ATOMISTIC INVESTIGATION OF IRRADIATION RESISTANCE OF HETEROPHASE METALLIC BOUNDARIES

A Dissertation
Presented to
The Academic Faculty

By

Elton Y. Chen

In Partial Fulfillment
of the Requirements for the Degree
Doctor of Philosophy in the
School of George W. Woodruff School of Mechanical Engineering

Georgia Institute of Technology

December 2019

ATOMISTIC INVESTIGATION OF IRRADIATION RESISTANCE OF HETEROPHASE METALLIC BOUNDARIES

Approved by:

Dr. Chaitanya S. Deo, Advisor
Department of Nuclear & Radiological Engineering, G.W. Woodruff School of Mechanical Engineering
Georgia Institute of Technology

Dr. Rémi Dingreville
Center for Integrated Nanotechnologies
Sandia National Laboratories

Dr. David McDowell
School of Materials Science and Engineering
Georgia Institute of Technology

Dr. Olivier Pierron
G.W. Woodruff School of Mechanical Engineering
Georgia Institute of Technology

Dr. Hamid Garmestani
School of Materials Science and Engineering
Georgia Institute of Technology

Date Approved: August 19, 2019

ACKNOWLEDGEMENTS

I would like to give thanks to my advisor Chaitanya S. Deo for his guidance and support throughout graduate and undergraduate studies; Rémi Dingreville for his mentoring during my time at Sandia National Laboratories; Center of Integrated Nanotechnologies (CINT) for hosting me and providing computation resources; my coworkers James Stewart, Pierre-Alexandre Juan, and Christopher OBrien for engaging in important scientific discussions; and the many labmates from Georgia Tech Alexander Moore, Ben Beeler, Jacob Startt and Daniel Vizoso.

TABLE OF CONTENTS

LIST OF TABLES

LIST OF FIGURES

SUMMARY

The overall purpose of this dissertation is to explore the complex mechanisms underneath the irradiation resistance of metallic phase boundaries. Materials in nuclear applications are constantly exposed to harsh radiation environments throughout their service lives. Interactions between high energy radiation sources and the atoms of the material will inevitably produce nanoscale defects in the crystal lattice. In large quantities, these radiation defects are known to cause swelling, embrittlement, and nano-scale crack growth, all of which negatively impact the mechanical performance of the material and can possibly lead to component failure. One of the most promising solutions to defect accumulation is to leverage the defect sink properties of the grain boundaries. By creating new nanocomposites/laminates/multilayers with high concentrations of boundaries, modern materials engineers are able to significantly improve the irradiation resistance of conventional metals. In order to further refine the design of these next-gen materials, it is crucial to first understand the complex relationships between radiation defects and boundaries over a large range of radiation doses. To this end, we have employed multiple advanced atomistic modeling methods in this dissertation to examine the various aspects of radiation defect production, accumulation, and evolution, as well as the interaction of radiation damage with phase boundaries and its effects on mechanical performance.

In the first examination of radiation defect production, we employed the standard collision cascade model to calculate threshold displacement energies for metallic uranium. The threshold displacement energy, commonly defined as the minimal amount of deposited energy required to displace an atom off its equilibrium lattice site to form a stable interstital-vacancy (Frenkel) defect pair, is one of the principle properties for estimating radiation defect production. By comparing the threshold displacement energies with respect to atomic recoil direction and ensemble temperature, we are able to examine the effects of lattice structure and thermal vibrations on radiation defect production/recovery.

In order to circumvent the poor scalability of the standard collision cascade models, we have also developed a new method of simulating large dose defect accumulation called Reduced-Order Atomistic Cascade (ROAC). Utilizing an accelerated Monte Carlo framework, ROAC generates radiation damage as reduced-order core-shells, with the core representing high energy thermal mixing, and the shell representing ballistic point defect production. Radiation damage produced using ROAC have been verified against damage produced using standard collision cascades over a wide range of recoil energies. An example application of ROAC to large dose accumulation models was able to demonstrate a significant computational acceleration over consecutive cascades.

To study large dose defect accumulation and evolution in metals, we employed an accelerated atomistic method named Frenkel Pair Accumulation (FPA). FPA rapidly produces point defects through atomic displacement, effectively modeling a high dose electron irradiation condition. Through the application of FPA to Zr and Nb, three early stages of defect evolution were identified for bulk metals, namely: dislocation accumulation, saturation and coalescence. Using these as the foundation, point defects are similarly inserted at Zr–Nb multilayers to compare boundary interactions. At smaller doses the phase boundaries demonstrated standard sink behavior by reducing local defect accumulation. However, at larger does, the accumulation of radiation-induced intermixing eventually caused a shift in the boundary morphology. The newly transformed Zr–Nb compound phase emitted a large quantity of dislocations, resulting in a net increase in radiation defect content.

Lastly, for the examination of the mechanical effects of radiation defects, we utilized a steady-state boundary fracture method. Employing the ROAC method previously verified for Cu and Nb, large dose heavy ion irradiation was modeled in Cu–Nb multilayers. At various radiation doses, hydrostatic tensile loading was applied to the system and boundary decohesion was then induced by creating sharp cracks along the interfacial plane. Comparisons of crack growth between irradiated and pristine boundaries demonstrated a noticeable reduction of plasticity with increasing dose. This embrittlement effect is attributed to the

suppression of long range dislocations ahead of the crack tip due to interactions with pre-existing radiation defects.

In this dissertation the multifaceted topic of the irradiation resistance of metallic phase boundaries is divided into and explored by its most basic components. By establishing the relationships between radiation defect accumulation, boundary microstructure evolution, and mechanical behavior, we were able to construct a holistic view of radiation material aging. With respect to either accuracy or expediency, the ROAC method developed in the current work has already proven to be a significant improvement over other existing state-of-the-art atomistic methods of modeling large dose accumulation. The application and scalability of the method can enable us to study many more large scale radiation effects previously thought inaccessible to atomistic simulations.

CHAPTER 1
INTRODUCTION AND BACKGROUND

1.1 Motivation

As the world continues to shift toward more carbon neutral means of energy production in efforts to combat climate change, nuclear power remains one of the most reliable, high-capacity and efficient methods of electricity generation. Unfortunately, due to the accident at Fukushima Daiichi nuclear station in 2011 and the subsequent negative shift in public opinions, the expansion of nuclear power capabilities around the world have mostly reached a standstill [1, 2], as illustrated by the stagnant growth in Fig. 1.1(a). In 2019, the majority of the world's operating, commercial nuclear stations consist of Generation II fission reactors constructed between the 1960s and 1990s (Fig. 1.1(b)), most of which are nearing the end of their initial licensing term [3]. Most of the ongoing/planned Generation III Light-Water Reactors (LWRs) constructions exist in eastern industrializing counties, i.e., China, Russia, India and South Korea [4, 5]. As we continue to extend the operation lifespans of the existing nuclear fleets in the west, the issue of material aging becomes increasingly important to operational reactor safety. Over the decade(s) long operational lives, reactor structural materials will inevitably accumulate radiation damage due to interactions with high energy radiation sources (α, β, or neutron). These radiation damage are commonly measured by the cumulative atomic displacements a material experienced, i.e. displacements-per-atom (dpa). At high dpa(s), radiation damage are known to cause unfavorable material changes such as swelling [6, 7], embrittlement [8, 9], and nano-scale crack growth [10], as shown in Fig. 1.2 These deteriorations in mechanical properties are major concerns for operational reactor safety, particularly during high-stress transient states such as startup and/or accident scenarios.

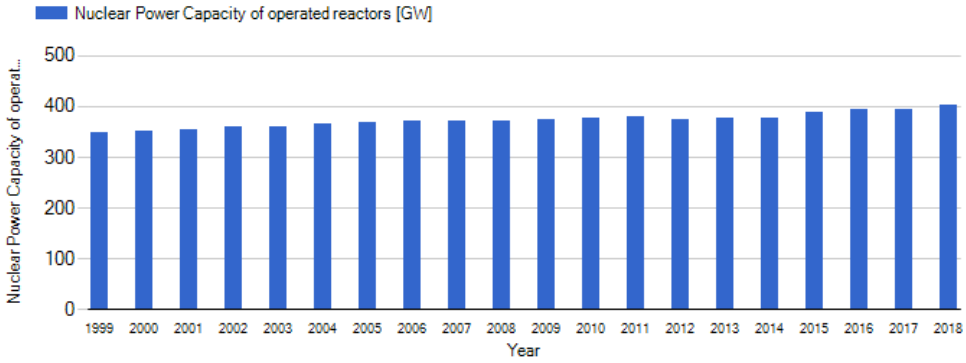

(a)

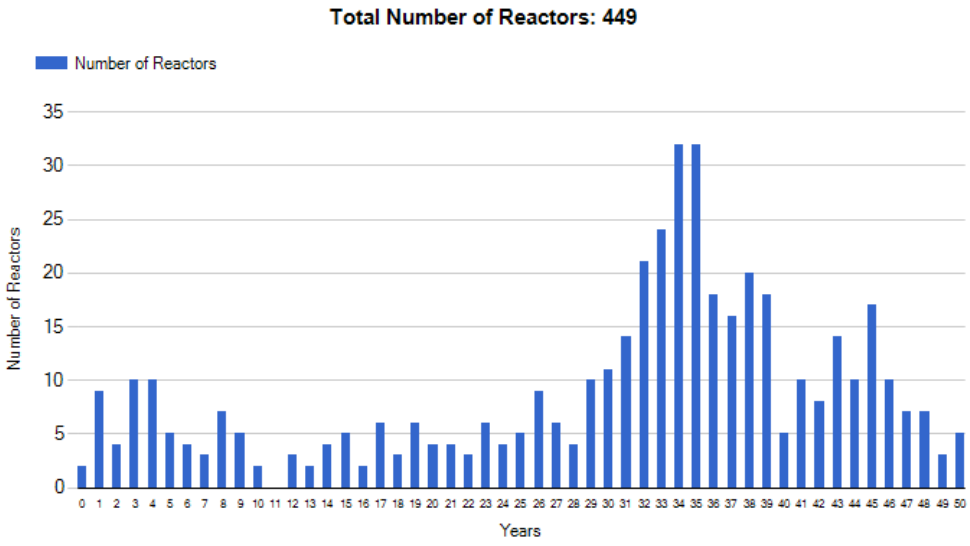

(b)

Figure 1.1: World nuclear power status in 2019, as taken from the Power Reactor Information System (PRIS) report [11] from International Atomic Energy Agency (IAEA). (a) Nuclear power capacity trend. (b) Operational Reactors by Age. Age of reactor is determined by its first grid connection. Reactors connected in 2018 are assigned with the age 0 years.

For the design of higher power Generation IV reactors and beyond, the emphasis on radiation material aging is increased. In both the proposed Molten-Salt Reactors (MSRs) and Liquid-Metal Fast Reactors (LMFRs), the radiation exposure rates and source energy spectrums are significantly harsher than those of the traditional LWRs. Depending on the reactor type and component proximity to the core, structural materials are estimated to

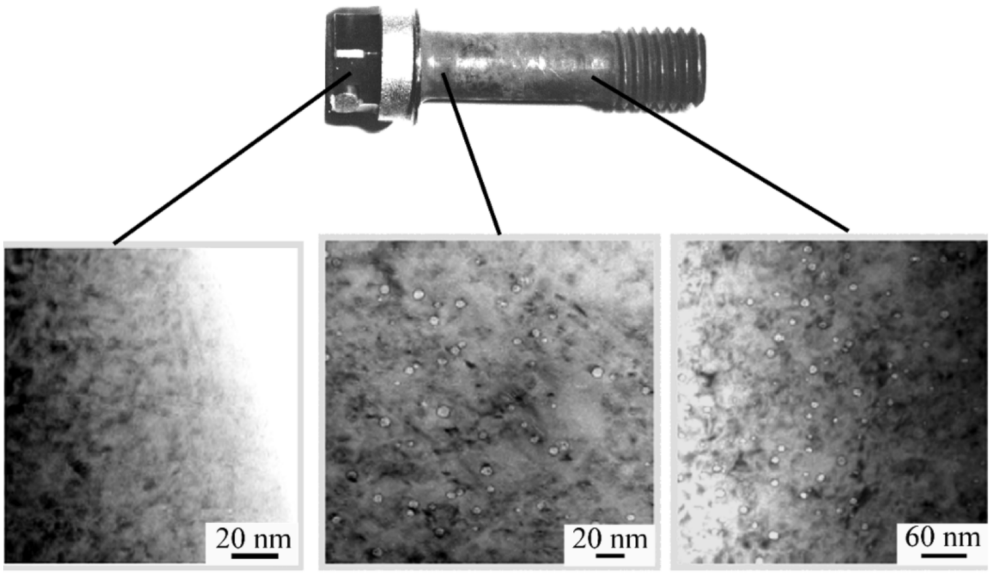

(a)

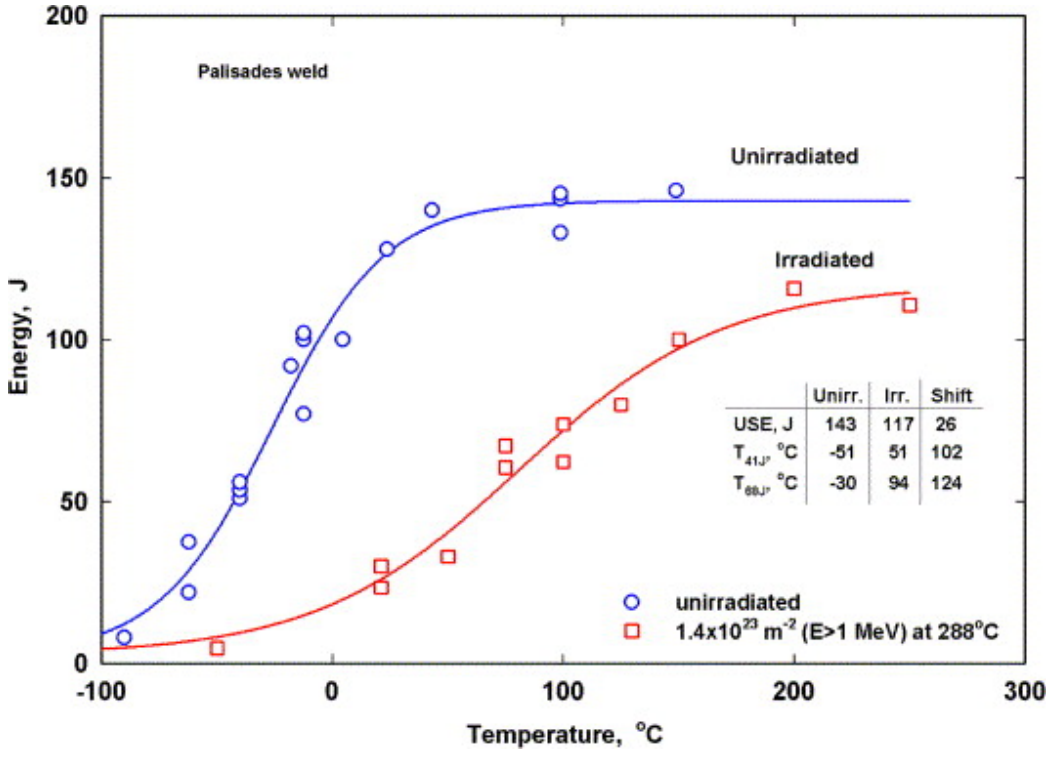

(b)

Figure 1.2: Material degradations caused by prolong exposure to irradiation conditions. (a) Radiation-induced swelling in a 316 SS baffle bolt in a PWR at different doses and positions [12]. (b) Radiation embrittlement of Palisades weld samples [13].

experience dose rates between $10^{-12} \sim 10^{-6}$ dpa/s, in existing commercial fission reactors [14]. By contrast, experimental fast reactors like the High Flux Isotope Reactor (HFIR) at Oak Ridge and the BOR-60 at Dimitrovgrad generate higher average dose rates of $\sim 10^{-7}$ dpa/s [15]. Similarly elevated dose rates are also expected in fusion application, based on the early projections of the DEMOnstration (DEMO) power station [16] and the International Fusion Material Irradiation Facility (IFMIF) program [17]. In order to ensure operational reactor safety, next generation structural materials need to be able to withstand these harsh radiation environments over long operational periods, without failure or significant loss of mechanical performance. For the engineering of these new radiation resistant materials, it's crucial to first study and understand the accumulation and evolution of radiation damage over large doses.

1.2 Radiation Interactions with Materials

Interactions between radiation sources and structural materials naturally occur at the atomic length scale. Any source of high energy radiation, predominately neutron for nuclear reactors, can interact with atoms in the structural material through the processes of atomic collision. Direct interactions between γ-photon and the atomic nucleus, i.e. photonuclear events, are much more rare, as most energies of γ-photon tend to scatter with the electron clouds. When an atom gains sufficient energy through the collision and become dislodged from its stable lattice site, it becomes a Primary Knock-on Atom (PKA). As the PKA traverses through the structural material lattice, it produces secondary collisions along its path, displacing neighboring atoms, and creating a collision/displacement cascade [18, 19]. This process is illustrated in Fig. 1.3(a). The shape of each cascade is determined by the energy of the initiating PKA, the structure of the bulk crystal lattice, as well as the thermodynamic properties of the structural material. In most dense metals, where cascade tends to compact, a cascade can also destabilize the local lattice, forming a high energy amorphous/liquid-like region commonly known as a Thermal Spike (TS). These thermal spikes are critical to the

accurate modeling of radiation damage accumulation and evolution, as we discuss later in Chapters 2 and 4. Eventually, the growth of a cascade reaches a limit when the initial PKA recoil energy has become so dispersed that secondary collisions can no longer dislodge any atoms from their original lattice sites. Following the principle of minimum energy, most of the displaced atoms are then inclined to diffuse back onto a free lattice site and to reform the energetically favorable bulk lattice configuration. While this annealing process does eliminate the majority of the unstable defects produced by the cascade, a small fraction of displaced atoms can become trapped and form more permanent defects. If a displaced atom occupies an interstitial site it becomes a Self-Interstitial-Atom (SIA), while also leaving a vacancy site within the lattice. These interstitial and vacancy point defect pairs, commonly known as Frenkel Pair (FP) defects, are illustrated in Fig. 1.3(b). While, individually, these point defects are inconsequential to the macroscopic material behavior, as they continue to accumulate, coalesce and evolve, the culminated large defect structures can cause severe degradation in mechanical performances [7, 20, 21].

With respect to crystalline metallic materials, there are several common forms of larger defect microstructures that can be expected post irradiation:

Small vacancy clusters can be found in common planar configuration, or tetrahedral configuration in FCC lattices [22]. They are highly mobile and diffuse via direct exchanges with on-lattice atoms [23].

Small interstitial clusters are commonly found in either planar or crowdion configuration [24]. They are mobile, and diffuses through the lattice by interstitial barrier hops or interstitialcy neighbor displacements [12]. Annihilations can occur when vacancy and interstitial clusters come into contact [25].

Voids are large spherical vacancy clusters that can grow up to be nanometers in length [6]. Due to their relative sizes, they act as immobile point defect sinks for both interstitials and vacancies [26].

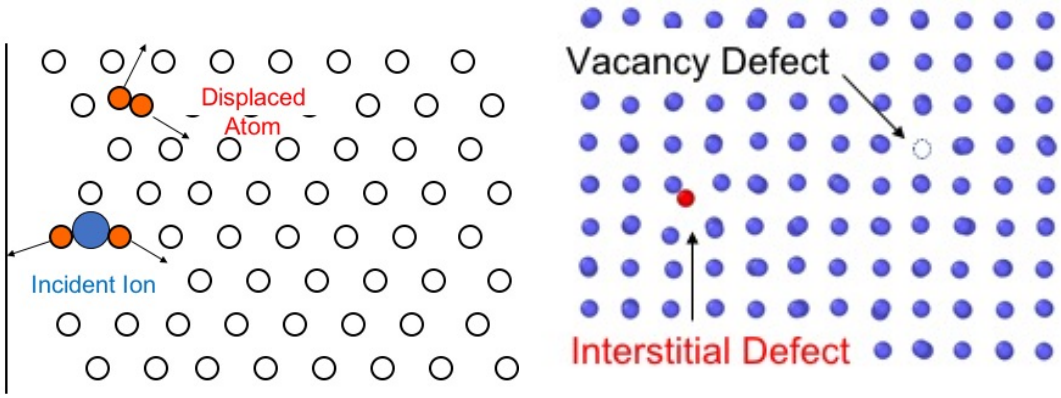

(a) (b)

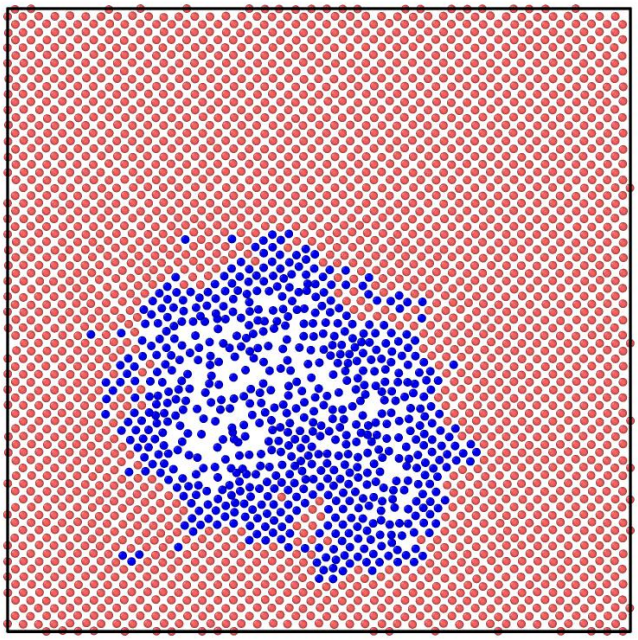

(c)

Figure 1.3: Radiation interactions with the material lattice. (a) Formation of the Primary Knock-on Atom (PKA) and the cascade. (b) Single Frenkel Pair (FP) defect formed by a cascade. (c) Slice view of a Thermal Spike (TS) in dense material lattice.

Dislocations are lines that form the boundary between regions of the crystal lattice that have and have-not slipped [12]. The Burgers vector of a dislocation describes the magnitude and direction of the local lattice distortion. The nature of the dislocation is determined by the relative orientation of the Burgers vector, with edge being $\perp$ to the line direction and screw being $\parallel$ to the line direction. At higher defect concentra-

tions, dislocations can provide a more holistic view of the three dimensional lattice disorder [27].

Stacking Fault Tetrahedra (SFTs) are a type of dislocation structure commonly produced in FCC metals [28, 29]. Surrounding low density vacancy clusters in tetrahedral arrangements, SFTs characteristically consist of stair-rod dislocation lines [30].

Many other sub-classifications of defect such as bubbles, gas atom interstitials, substitutional defects, and precipitates do exist when external ions infiltrate the material system during irradiation. However, within the constraints of the current work, these cases are neither considered nor appear in any of the simulation models.

1.3 Grain Boundary Effects

While radiation defect production in bulk single crystals is largely governed by material properties and lattice structures, these idealized characteristics are rarely applicable in the presence of microstructural features such as free surfaces, grain boundaries and nanocavities. In particular, grain boundaries, an ubiquitous feature of polycrystalline metals, are known to act as defect sinks due to their high excess volumes and low defect formation energies [31]. Over short periods of time, simulations of radiation cascades near the grain boundaries have been able to demonstrate a large reduction in initial point defect production [32, 33]. Over longer periods of time, stress fields emitted from the boundaries can influence long range thermal diffusion and attract mobile point defects towards the sink sites [34, 35, 31]. Utilizing these beneficial characteristics, modern grain boundary engineering has been able to effectively control both the defect contents and the mechanical properties of the crystalline bulks [36, 37, 38]. However, the accumulation and concentration of defects and stresses at the sink sites also make grain boundaries more susceptible to mechanical failure. The formation of micro-cracks due to void accumulation and the crack extension due to embrittlement ultimately lead to the phenomenon known as grain bound-

ary decohesion [21, 39, 40]. Thus, in order to study of the effects of radiation material aging holistically, it is important to examine not only the accumulation of damage in the bulk crystal, but also the evolution of defects near the grain boundaries.

Of the various types of grain boundaries that exist in crystalline metals, the present work specifically focuses on heterophase boundaries. Unlike common grain boundaries, which typically consist of two grains with distinct lattice orientations, heterophase boundaries also introduce the complexity of dissimilar bulk properties, which can include: elasticity, atomic composition, phase morphology, and even radiation defect production. This type of boundary is usually found in engineered materials and components, i.e. in nanolayered composites (nanolaminates) [41], coatings [42], or thin films [43]. Recent studies on these nanolaminates have demonstrated both superior radiation tolerances [44, 45] and mechanical properties [46, 47] as compared to traditional polycrystalline metals, making them promising candidates for nuclear applications.

1.4 Goal & Scientific Questions

The central goal of this dissertation is to:

- **Examine the mechanisms of radiation aging at heterophase boundaries and the effects of aging on mechanical properties.**

To this end, we have chosen to employ atomistic models, as they are uniquely suited to simulate the process of radiation defect production that naturally occurs at the atomic length. Starting with a more ab-initio approach also allows us to explore the complex interactions between radiation defects and phase boundaries, all of which are inaccessible to higher length/time-scale rate-theory, Cluster Dynamic (CD), and kinetic Monte Carlo (kMC) models. However, in order to examine the mechanisms of radiation material aging, there are limitations inherent to atomistic models that need to be surpassed. As discussed in detail in Chapters 2 and 4, while standard atomistic models excel in the simulation of single cascades, they are ill-suited for the simulation of radiation defect accumulation over hundreds

of thousands of cascades. In Chapter 2, the review of state-of-the-art modeling techniques also reveals distinct deficiencies in each of the existing methods for simulating radiation defect accumulation. Therefore, in support of the central goal, it is also necessary to:

- **Develop a new atomistic method of simulating defect accumulation and material aging over large doses.**

Through the application of this new atomistic modeling method, we seek to investigate a series of scientific questions concerning the relationships between radiation defect accumulation, boundary microstructure evolution and mechanical performance. Beginning with the exploration into radiation defect accumulation, the first question is:

Q1 How are radiation defects produced in bulk crystals, and what are the mechanisms of defect accumulation?

By first examining radiation defect production and accumulation in bulk materials, we can establish a basis for comparison against similar behaviors in phase boundary models. Building upon this foundation, the second questions becomes:

Q2 How do phase boundaries affect radiation defect accumulation, and how does the interfacial microstructure evolve?

By answering this question, we can establish the relationship between radiation defects and phase boundaries, in addition to identifying important boundary characteristics for controlling defect contents in the bulk grains. Lastly, exploring the mechanical effects of phase boundary irradiation, the third question is:

Q3 How do radiation defects affect phase boundary decohesion, and what are the roles of microstructures?

By reviewing the final relationship between microstructure and mechanical behavior, we can finally obtain a holistic perspective on the processes, mechanisms and effects of radiation material aging.

1.5 Dissertation Outline

In the following chapters we will be examining the various aspects of the radiation resistance of heterophase metallic boundaries. Similar to scientific questions posed in the previous section, the chapters are ordered to first establish the baseline characteristics of radiation defect production and phase boundary microstructures, before exploring the complex mechanisms behind defect accumulation at the boundaries.

Chapter 2 serves as an overview of modeling methods employed in the current work. Section 2.1 first discusses the basic principle of atomic models and requirements for modeling radiation cascades. Section 2.2 then presents two state-of-the-art techniques, Frenkel Pair Accumulation (FPA) and Consecutive Cascade (CC), for simulating radiation defect accumulation over large doses. The deficiencies of each technique are explored in detail in Section 2.3, which eventually leads to the proposal and outline of a new modeling method.

As an initial investigation on radiation defect production, Chapter 3 presents a study on the threshold displacement energies of multi-phased metallic U. The threshold displacement energy (E_{d}), commonly defined as the minimal amount of deposited energy required to displace an atom off its equilibrium lattice site to form a stable Frenkel Pair (FP) [12], is one of the principle properties for estimating radiation defect production. Different empirical derivations of threshold displacement energy can be found in Section 3.2.3. In order to examine the effects of lattice structure on defect production, a novel crystallographic symmetry-informed orientation sample scheme was developed in Section 3.2.2 for the anisotropic α-U phase. Finally, Section 3.3 presents all variations of the E_{d} results with respect to temperature, lattice structure and recoil orientation.

Expanding upon the initial proposal made in Chapter 2, Chapter 4 presents the development and verification of the new Reduced-Order Atomistic Cascade (ROAC) method for simulating dose accumulation in metals. Section 4.2 presents the updated theoretical athermal recovery corrected (arc) damage model [48], which incorporates the effects of thermal

spikes and serves as the foundation of the new method. The implement of the ROAC method is described in Section 4.3.1, and the model accuracy is verified in Section 4.3.2. For demonstration purposes, Section 4.4 also provides two novel applications of ROAC for high energy cascade fragmentation and large dose accumulation.

Shifting the focus towards phase boundary microstructures, Chapter 5 presents a study on the characteristics of pristine U–Zr stacking interfaces. Procedures for constructing and modeling atomistic phase boundaries are presented in Section 5.2 and the emergent interfacial microstructures are compared against lattice theory predictions in Section 5.3.1. In relation to the composition and chemical mismatch at the interface, the anisotropic interface energetics and stress fields are also explored in Section 5.3.2 and 5.3.3 respectively.

Combining the aspects of radiation damage and phase boundaries, Chapter 6 presents a study on radiation defect accumulation in Zr–Nb multilayers. By adapting the state-of-the-art FPA technique in Section 6.2.2, large dose electron irradiation is simulated for bulk Zr, bulk Nb and three different phase boundary combinations. Section 6.3.1 identifies the different stages of defect evolution in the bulk metals, which then serve as the basis of comparison against similar behaviors in Zr–Nb multilayers. Section 6.3.2 examines both the morphology of the interfacial microstructures and the boundary-defect interactions as functions of dose.

Integrating all of the previous works, Chapter 7 presents a preliminary investigation into the mechanical properties of Cu–Nb multiplayers post irradiation. Employing the ROAC method presented in Chapter 4, heavy ion irradiation is simulated up to a dose level of ~ 0.5 dpa in Section 7.1. At regular dose intervals, phase boundary decohesion is induced near the initial phase boundary using the method presented in Section 7.2. In Section 7.3, the final decohesion/crack extensions are compared against each other, in order to assess the overall mechanical embrittlement.

Lastly, the conclusion of the dissertation are presented in Chapter 8, along with recommendations for future works.

CHAPTER 2
TECHNICAL APPROACH

As stated in the previous chapter, atomistic models are unique suited to the study of radiation defect accumulation at the atomic length scale, at which defect production naturally occurs. In lieu of having a predefined probability or mobility for defect-defect interactions, as with cluster dynamic and kinetic Monte Carlo models, atomistic Molecular Dynamics (MD) models directly simulate the motion of atoms to allow thermodynamically accurate evolution of defects over time. This flexibility of the MD models is also what makes them the only viable tool for exploring the undefined processes and mechanisms of defect evolution. As such, this following chapter will serve as both an overview of the principles of MD as well as a review of the two state-of-the-art techniques of simulating radiation defect accumulation.

2.1 Basics of Molecular Dynamics (MD)

The fundamental principle of MD lies in the time integration of thermodynamic motions in accordance with Newton's equation of motion ($F = ma$). Atoms in a MD model are treated as individual point masses with dynamic positions and velocities. Over each time integration, the position of an atom is updated based on its velocity, and the velocity of an atom is updated based on the thermostat and net external force. Without adding artificial constraints, all forces acting on an atom are due to interaction(s) with neighboring atom(s). By simultaneously simulating a multitude of atoms, MD models are able to effectively replicate large ensemble structures such as crystal lattices, grain boundaries and multilayers.

2.1.1 Interatomic Potentials

Thermodynamic, elastic and chemical characteristics of an ensemble structure are fundamentally determined by the interactions between individual atoms. In MD models, these interactions are described by mathematical functions known as interatomic potentials. Depending on the application and the material, different potentials can have varying functional forms with a wide range of complexity. For the modeling of radiation damage accumulation, we have chosen to use Embedded-Atom Model (EAM) potentials, which contain a balance of accuracy and computation speed. The most basic form of a Nb-Nb pair potential [49] is shown in Fig. 2.1, where $V(r)$ is the pair potential, r is the pair separation distance, and r_0 is the optimal pair separation distance at the bottom of the potential well.

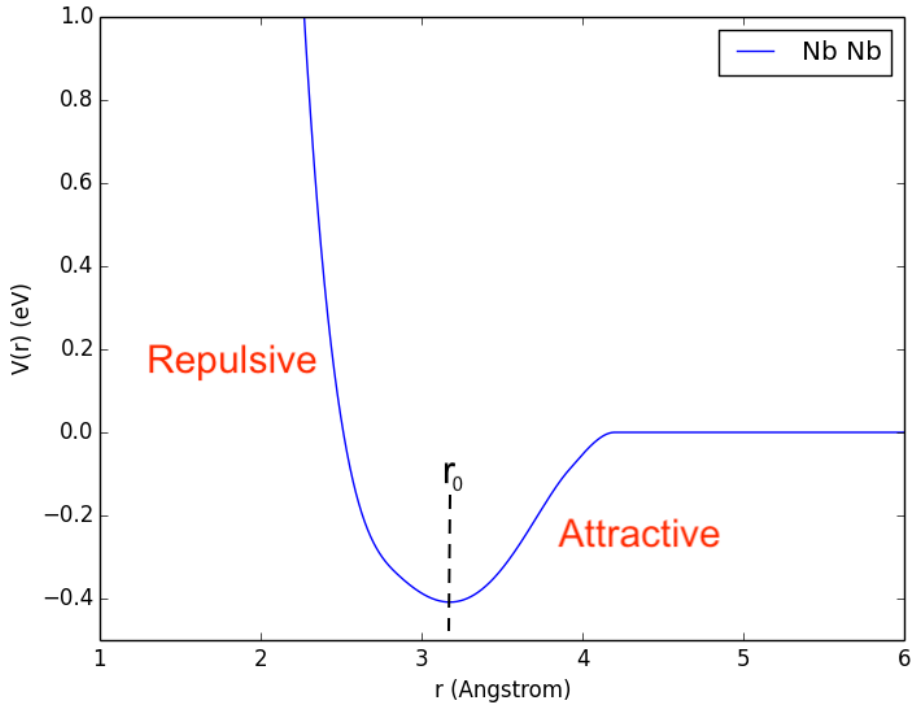

Figure 2.1: Nb-Nb pair interactions presented by Zhang et al. [49]. Atom interactions are repulsive at $r < r_0$ and attractive at $r > r_0$.

As r_0 roughly represents the nearest neighbor distance in a lattice, most of the elastic and thermodynamic properties of the bulk structure can be derived from the immediate

surrounding potential well. Understandably, when developers create a new interatomic potential, the majority of the effort is spent on optimizing the fitting of potential wells at 2 Å$\leq r \leq$ 5 Å. Short-range interactions ($r < 1\mathring{A}$) and long-range interactions are often neglected and occasionally truncated for metals, as they are effectively inconsequential for simulation of bulk material behaviors.

2.1.2 Modeling Collision Cascades

The modeling of collision cascades is nearly identical to the process described in Section 1.2. The main difference being, instead of having external radiation sources, a PKA can be directly created in the crystal by providing an atom with an elevated velocity/kinetic energy. After a PKA is designated in the simulation, the full collision cascade is allowed to develop over a period of 20 ps. While the majority of the displacement damage is generated within the first 0.5 ps, as shown in Fig. 2.2, only the defects that survive the annealing stage are considered stable. During the entire development period, the simulation is kept in an isochoric and constant energy (NVE) ensemble, such that no kinetic energy is artificially removed by the thermostat. Variations of this model are employed in both Chapter 3 and Chapter 4, where full collision cascades with a wide range of PKA energies are examined.

The modeling challenges of collision cascades are entirely caused by the high energy, high velocity atomic collisions at the initial stage of cascade growth. To start with, simulation of collision cascades requires adaptive time stepping. For the standard atomic motion integration in a MD simulation, the time step (Δt) is determined by the maximum displacement amongst all of its atoms. If a time step is too large, it can be detrimental to the stability of a simulation. To a smaller extent, if an atom misses a collision, it could create a false impression of channeling. To a greater extent, if atoms overlap, the exponential growth of the pair potential at close range can easily induce artificial thermal explosions. This only becomes more important for high energy PKAs, where Δt at the early stage of the

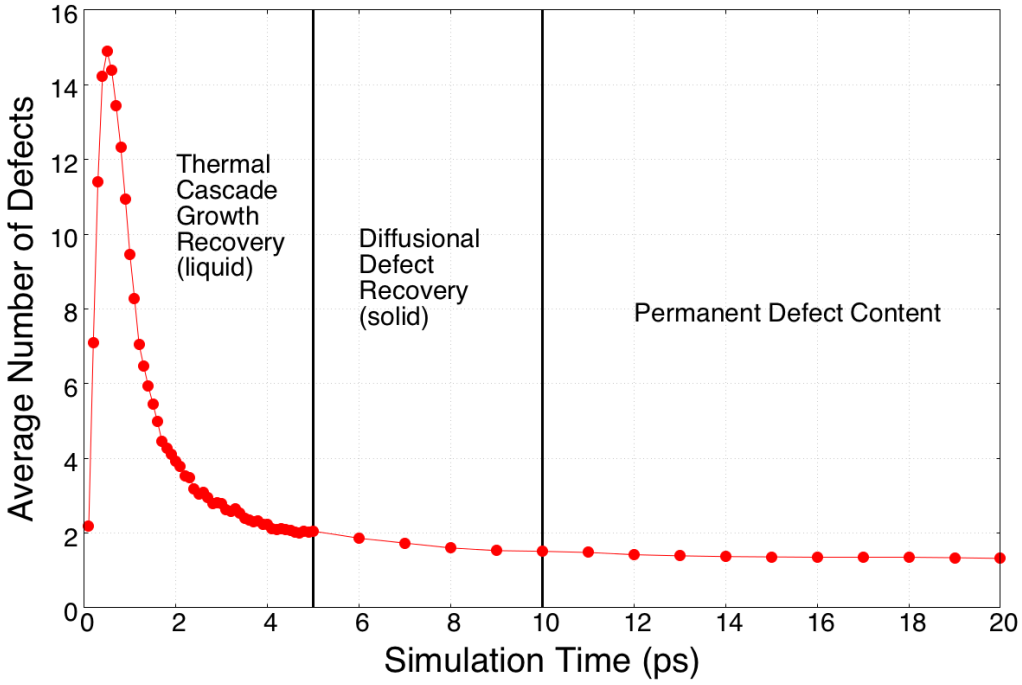

Figure 2.2: Average number of defects generated by cascades over 20 ps. Data are taken from 100 cases of 180 eV cascade in uranium.

cascade development needs to be several orders of magnitude smaller than that at thermal equilibrium (generally on the order of tens of attoseconds).

While adaptive time stepping can potentially inflate the computational costs of the model, it is always resolvable. The more difficult challenge of modeling collision cascades is the severe restriction on usable interatomic potentials. To accurately simulate the process of high energy/velocity collisions, an interatomic potential appropriate for cascade modeling must be fitted to the Ziegler-Biersak-Littmark (ZBL) nuclear repulsion interaction [50] at close range. However, as previously stated, this is not a common practice in interatomic potential development when radiation damage is not of interest. An inadequately fortified potential can similarly induce artificial thermal explosion, should high velocity atoms achieve near overlap. Although the ZBL modification can be easily added to existing Embedded-Atom Method (EAM) potentials at close range, the resulting changes in defect properties often necessitate the revalidation of the potential as a whole [51].

2.2 Advanced Methods for Simulating Radiation Damage Accumulation

The main challenge of simulating radiation damage accumulation is scaling computational costs. While individual events can be reasonably modeled by collision cascades, the cost of simulating higher doses can quickly become exorbitant. Presented below are two state-of-the-art methods that have been developed to tackle this very problem. One method pushes the concept of collision cascade to the extreme, while the other seeks to bypass the process entirely.

Consecutive Cascade (CC) method was originally used by Zhang and Demkowicz [52] to examine radiation induced mixing at the Cu-Nb phase boundary. Relatively crude and brute-force, the full high-energy cascades are inserted near the boundaries to induce localized melting. In order to prevent artificial cascade-cascade interactions, cascades are restricted to sequential insertion, with complete annealing between events. As radiation events accumulate near the phase boundary, the previous discrete bimetallic interface evolves into a more diffuse concentration gradient. Using the CC method, the authors were able to replicate the effects of ion-beam mixing for layered metallic systems [53], matching the results from several heavy ion irradiation experiments [54, 55, 56, 57]. This study has also demonstrated the fluid morphology of phase boundaries due to thermal spike melting, which will be explored in more depth in Chapter 6.

Frenkel Pair Accumulation (FPA) method was originally proposed by Chartier [58] to examine large dose accumulation in ceramic systems. A significantly accelerated process, this method directly introduces Frenkel Pair defects into the simulation by displacing atoms from their original lattice sites, bypassing the cascade process altogether. As the insertion of FPs is unrestricted by the overlap of cascades, the simulated dose rates can reach several order of magnitudes higher than full cascades. Through the repetition of FP insertion, the study was able to replicate five early stages

of damage accumulation: point defect production, defect clustering, Frank loop nucleation, transformation to Shockley loop, and formation of dislocation forest. The presented UO_2 example was also verified against experimental TEM data, matching dislocation patterns at varying doses. Unfortunately, there are some concerns with the applicability of the method to high energy radiation events, particularly due to the absence of thermal spikes.

2.3 Challenges of Modeling Physical Mechanisms

As is the case with most advanced modeling methods, neither accuracy nor expediency can be obtained without sacrificing the other. The CC and FPA methods each represent the relative extreme of one characteristic, which ultimately limits their applicability to dose accumulation models.

In particular, the CC method, while accurate, is incredibly computationally inefficient for scaling to larger doses and higher length scales. At the atomic scale, the dose/damage level, dpa, is measured as $\frac{N_{\text{defect}}}{N_{\text{cell}}}$, where N_{defect} is the cumulative number of defects and N_{cell} is the size of the simulation cell. The number of point defects generated per event n_{NRT} can be roughly estimated by the Norgett-Robinson-Torrens (NRT) damage model [59]:

$$n_{\text{NRT}} = \begin{cases} 0 & \text{for} \quad E_{\text{PKA}} < E_{\text{d}} \\ 1 & \text{for} \quad E_{\text{d}} < E_{\text{PKA}} < \frac{2E_{\text{d}}}{0.8} \\ \frac{0.8E_{\text{PKA}}}{2E_{\text{d}}} & \text{for} \quad \frac{2E_{\text{d}}}{0.8} < E_{\text{PKA}} < \infty \end{cases} \tag{2.1}$$

where E_{PKA} is the PKA recoil energy, and E_d is the threshold displacement energy. Using standard 10 keV cascades as the basis, the original Cu-Nb examples [52] simulated $\sim$10,000 consecutive cascades to generate 3 dpa in a 250,000 atom simulation. If we want to examine the mechanical degradation in a more holistic 5,000,000 atom simulation, $\sim$200,000 consecutive cascades would be needed to reach the same dose level. Compound

that with the 20 fold increase in atom population per motion integration step, the computational costs would multiple by a minimum factor of $\times 400$. Even with access to high performance computing clusters, such expense remain unreasonable and inaccessible in most cases.

In stark contrast, the FPA method heavily favors computational efficiency over accuracy. However, it would be false to simply call the method inaccurate, as sparse point defect production is characteristic to ceramics and semiconductors, which are the intended material systems. Issues only appear when applying the FPA method to metals and other dense material systems. In low energy irradiation conditions (electron), the production of sparsely distributed FPs remains dominant, as PKAs rarely receive sufficient energy to initiate a cascade. In high energy irradiation conditions, such as ion or neutron, the appearance of cascade thermal spikes become prominent, which fundamentally alters the mechanisms of defect production. MD studies of cascades have repeatedly shown that the presence of thermal spikes is responsible for not only the amorphization and phase transformation of polymorphic metals and ceramics [60], but also the creation of large interstitial clusters ahead of the thermal shock fronts [61]. Without addressing these high energy processes, the FPA method is restricted to a very narrow range of applications and is ill-suited for modeling the nuclear reactor conditions this work seeks to examine.

With the goal of studying defect evolution under realistic irradiation conditions, an alternative method of modeling damage accumulation must be considered. As is, both methods discussed have limited applicabilities due to their respective computational and mechanistic constraints, but the advantages of the two methods appear to be complimentary. Therefore, using these methods as a framework, we have constructed a third, hybrid method of modeling radiation dose accumulation in Chapter 4. Extracting the accuracy of the CC method, the new method reintegrates the energy dependent cascade thermal spikes through reduced-order approximations. Extracting the computational efficiency of the FPA method, the new method also adopts a Monte Carlo approach of defect production and accelerates

the overall process of dose accumulation.

CHAPTER 3

ATOMISTIC SIMULATIONS OF TEMPERATURE AND DIRECTION DEPENDENT THRESHOLD DISPLACEMENT ENERGIES IN α- AND γ-URANIUM [62]

In an effort to answer **Q1: How are radiation defects produced in bulk crystals, and what are the mechanisms of defect accumulation?**, this chapter examines the low energy radiation defect production in crystalline metals. Specifically, we have calculated the various definitions of threshold displacement energy for the low-temperature and high-temperature phases of metallic uranium. The threshold displacement energy (E_{d}), commonly defined as the minimal amount of deposited energy required to displace an atom off its equilibrium lattice site to form a stable Frenkel Pair (FP) [12], is one of the principle properties for estimating radiation defect production. It is commonly used in the empirical NRT-dpa [63, 48] and arc-dpa [64, 48] damage models, which serves as the foundation for the new ROAC method for simulating dose accumulation presented in Chapter 4. By quantitatively comparing E_{d} for a wide range of temperatures and recoil directions, we are able to investigate the effects of kinetics and crystal structure on radiation defect production.

3.1 Introduction

Metallic uranium alloys (uranium–zirconium, uranium–molybdenum) have been employed as fuel elements in a number of experimental fast reactors, including the Experimental Breeder Reactor (EBR) series, Dounreay Fast Reactor (DFR), and Fermi reactors [65]. Metallic alloy fuels possess superior neutronic properties, thermal conductivities [66, 67, 68], higher burnup, and ease of fabrication [69] compared to classical ceramic fuels. These alloys predominately consist of uranium [69], whose behaviors under irradiation are far less characterized than the more commonly studied uranium dioxide UO_2.

Due to the instability caused by its f electron shell [70], metallic uranium is very sensitive to changes in temperature and pressure conditions. As a result, uranium can exist in multiple phases with differing macroscopic properties. The three most commonly observed solid phases are the orthorhombic α-uranium, the tetragonal β-uranium, and the cubic γ-uranium. The ground state α-uranium exists in a rare Strukturbericht A20 structure [71]. At a temperature of approximately 935 K, α-uranium transforms into body-centered tetragonal (BCT) β-uranium; while at a temperature of 1045 K, β-uranium transforms into body-centered cubic (BCC) γ-uranium, which persists until melting at 1406 K [72]. Due to the narrow temperature range of the β-uranium, this study focuses on radiation events in the low temperature α-uranium phase and in the high temperature γ-uranium phase.

One of the most basic properties associated with the efficiency of resistance to radiation damage is the threshold displacement energy, E_{d}. The threshold displacement energy is commonly defined as the minimal amount of deposited energy required to displace an atom off its equilibrium lattice site to form a stable Frenkel Pair (FP) [12]. The material science and nuclear energy communities have studied the threshold displacement energy both experimentally and numerically by first principle and atomistic simulations for a wide range of materials [73, 74, 75, 76, 77, 78, 79, 64, 48, 80, 81]. Subsequently, values extracted from the experimental and simulation studies for the threshold displacement energies are used in theoretical models such as the Kinchin-Pease (KP) model [82], the Norgett-Robinson-Torrens (NRT) model [59], or the Athermal Recombination Correct-dpa (ARC-dpa) model [64, 48] to estimate defect production for any known spectrum of primary knocked-on atoms (PKAs) [83].

Threshold displacement energies can have vast variations, as determined by factors like crystallographic direction, temperature, and applied strain [84, 85, 86]. With respect to crystallographic directions, the threshold displacement energies along channeling directions tend to be lower than the average, due to the absence of direct collision events. The temperature and applied strain control the various degrees of thermal motions and lattice

distortions, which can either assist in diffusional point defect annihilation, or loosen the lattice and facilitate point defect production. At high temperatures, thermal atomic vibrations and potential spontaneous metastable phase formation make difficult the determination of E_{d}. Consequently, threshold displacement energy calculations done at 0 K or near static conditions [87, 88, 74] present noticeable differences from those done at temperature [73, 79].

Due to the difficulty of conducting experiments with actinides and modeling anisotropic A20 lattices, there is only one other study on threshold displacement energies in metallic uranium which was conducted by Beeler [89]. Beeler's study primarily focused on the high temperature γ phase in uranium, with a fairly rudimentary and brief examination of the α phase to establish direction-specific E_{d} trends. For the description of atomic interactions, their study surveyed three interatomic potentials for uranium, including two U [90] and U–Zr [91] Modified Embedded-Atom Method (MEAM) potentials, and one U–Mo [92] Angular Dependent Potential (ADP). Beeler's study however adopted the more traditional incremental angle sweep sampling method [75, 80, 89] for selecting recoil directions, limiting the range and validity of the calculated threshold displacement energies within the fundamental zone. Indeed, this traditional method introduces a systematic sampling bias which can lead to the miscalculation of threshold displacement energies.

In this study, we have systematically characterized the threshold displacement energy in metallic uranium as a function of both the temperature and the recoil direction using Molecular Dynamics (MD) with an Embedded-Atom Method (EAM) interatomic potential capable of representing both the α and γ phases in uranium. Following Nordlund et al. [77], we have calculated threshold displacement energies using several definitions: a direction-specific threshold displacement energy ($E_{\mathrm{d}}\left(\theta,\phi\right)$), an angle-averaged threshold energy ($E_{\mathrm{d}}^{\mathrm{ave}}$), a production probability threshold displacement energy ($E_{\mathrm{d}}^{\mathrm{pp}}$), and a defect count threshold displacement energy ($E_{\mathrm{d}}^{\mathrm{dc}}$).

For the orientation sampling of the anisotropic A20 α-uranium lattice, we present a

novel crystallographic symmetry-informed orientation sampling method. The orientation sampling process is nontrivial, since the selected directions should be both evenly distributed and capable of representing the full unique orientation space, i.e., the fundamental zone. Sampling techniques such as the incremental angle sweep [75, 80, 89] and the random point distribution [77, 81] has been commonly used in the archetypal threshold displacement calculations, but neither can simultaneously provide both uniform and complete coverages of the fundamental zones. Aimed at improving upon these techniques, the new orientation sampling method is adapted for both the A20 and BCC crystalline structures of uranium. Collision cascade simulations are first conducted at each sampled crystallographic direction, for the calculation of direction-specific threshold displacement energies. The combined simulations results are then used to determined the average threshold displacement energies. The comparison between the present study and that of Beeler serves not only as a verification of the threshold displacement energies calculated here, but also as a demonstration of the benefits and added rigor of using the crystallographic symmetry-informed orientation sampling method presented in this manuscript.

In what follows, Section 3.2.1 describes the setup for the atomistic simulations of individual threshold displacement event with a Primary Knock-on Atom (PKA) used to calculate the various definitions of E_{d}. Section 3.2.2 presents the generalized crystallographic symmetry-informed orientation sampling method developed to fully cover the crystallographic orientation space within the fundamental zone. Section 3.3 presents the calculated threshold displacement energies over the range of temperatures surveyed and as a function of the orientation. This section also presents the analysis of the associated stable defect structures observed for each phase (α- and γ-uranium). Comparisons with the results from Beeler [89] are shown in each section respectively, when applicable.

3.2 Methodology to predict threshold displacement energy

3.2.1 Atomistic simulation

We have performed Molecular Dynamics simulations for collision cascades using the Large-scale Atomic/Molecular Massively Parallel Simulator (LAMMPS)[93] software package. Since the present study is concerned with the threshold displacement energies in both α- and γ-uranium, the multi-phased uranium EAM potential by Smirnova [94, 95] is used to describe interatomic interactions. Smirnova et al. have conducted Density Functional Theory (DFT) calculations to fit their interatomic potential for the two uranium phases across a wide range of temperatures. Based on these DFT calculations and available experimental data, the fitted potential correctly replicates many lattice properties including the bulk moduli, bond angle distribution functions, and point defect formation energies.

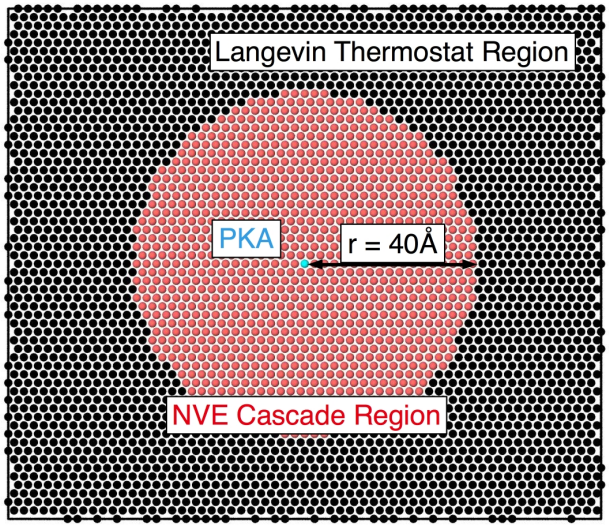

Figure 3.1: Cross section schematic of a cascade simulation cell. The γ-uranium simulation cell is an approximate 105 Å$\times$ 105 Å$\times$ 105 Åcube; while the α-uranium simulation cell is an approximate 85 Å$\times$ 170 Å$\times$ 150 Årectangular prism. The atom at the center of the simulation cell is given an energy and velocity corresponding to being struck by an energetic particle.

Figure 3.1 illustrates a schematic of the simulation setup used to introduce single collision cascade within the simulation domain. A simulation cell is initially constructed as

a perfect $30 \times 30 \times 30$ super-lattice, with periodic boundary conditions in all directions. An isothermal (T_{ambient}) and isobaric ($P = 0$) ensemble (NPT) is first applied to the simulation cell to allow relaxation of the energy and the structure. To cover the wide range of phase stability, $T_{\text{ambient}} = 10$ K, 300 K, and 600 K are simulated for the α phase. For the γ phase, T_{ambient} is tested at the lowest temperature of 900 K at which this phase is stable. Higher temperatures, i.e., $T_{\text{ambient}} > 900$ K, are not considered in the present study, as spontaneous point defect pair formations were observed near the melting point. Upon reaching thermal equilibrium after 20 picoseconds, the isobaric NPT ensemble is then switched to an isochoric and constant energy ensemble (NVE) to allow temperature-independent cascade development. Within this configuration, an atom at the center of the simulation cell is designated as the PKA, as shown in blue in Fig. 3.1. A Langevin thermostat [96] is then applied to atoms 40 Åaway from the PKA, as shown in black in Fig. 3.1. Such thermostat creates an over-damping region in the simulation cell, aimed at absorbing long range cascade shock fronts and eliminating cascade self-interactions across the periodic boundaries. Trapping of the recoil atoms in the over-damping region is not of any concern in the present study, since for all intents and purposes, (i) any 40 Ålarge recoil event is guaranteed to be well above the displacement threshold energy, and (ii) our simulation are conducted at energies near the threshold displacement energy.

To initiate a collision cascade, the PKA is given a high initial velocity, corresponding to a fixed recoil energy and direction. The recoil energies considered here range from 20 eV to 180 eV with an increment of 10 eV. Moreover, in the case of α-uranium, we have performed additional simulations for recoil energies at 220 eV, 260 eV, 300 eV and 400 eV in order to better approximate defect production probability of one, i.e., to better approximate the PKA energy at which a Frenkel pair is guaranteed to form. In the case of α-uranium, we have tested 417 unique recoil directions, while in the case of γ-uranium, we have tested 153 unique recoil directions. The details of the orientation sampling scheme are discussed in Section 3.2.2.

For the first 5 picoseconds of cascade development, a finer time integration step of 0.1 femtosecond is used to accommodate the elevated atomic velocities. After 20 picoseconds of cascade development and annealing, the simulation is then quenched by removing the kinetic energy and minimizing the potential energy. This process freezes any existing defect structures and prepares the superlattice for the post-processing analyses.

In order to generate a defect probability at every recoil energy and direction, we have conducted 20 random temperature seeded simulations for each combination. In total, we have conducted $175,140$ simulations for each T_{ambient} for α-uranium and $52,020$ simulations for γ-uranium.

For low-energy incident particles passing through a solid, nuclear stopping is the dominant mechanism, leading to collisions with atoms cores in turn causing displacement damage. As such, electronic stopping is fairly negligible at energies near or at E_{d} and can be neglected. To better account for the close-range interactions of the nuclear stopping, the standard LAMMPS implementation of the Ziegler-Biersack-Littmark (ZBL) [50] potential is introduced as an additive overlay to increase the close-range nuclei repulsion forces. The switch function to zero-out ZBL interactions at long range is set at the inner radius of 0.5 Å, approximately the Bohr radius for the inner electron shell, and the outer radius of 0.95 Å. It is important to note here, that the splining of ZBL hardening over the intermediate range of the potential has been shown to influence the predicted threshold displacement energies [51]. However, since no refitting is conducted for the EAM potential, such effect is expected to be minimal.

3.2.2 Cubic subdivision sampling in uranium lattices

Given the stochastic nature of recoil (PKA) events, an accurate assessment of the threshold displacement energies would typically require the sampling of all possible recoil directions. However, not all recoil directions are unique with respect to the crystal lattice. Instead, the full spherical orientation space can be reduced down to a small subset of unique orientations

through the application of crystallographical symmetry. This smallest unique subset of orientation space is commonly known as the *fundamental zone* [97].

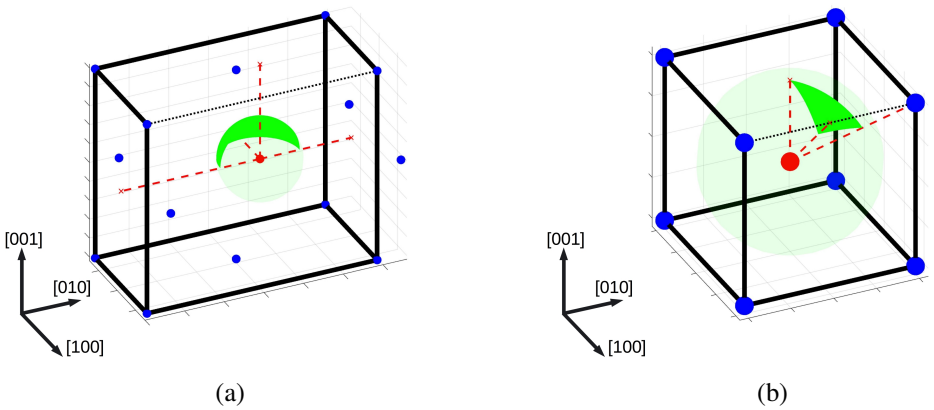

Figure 3.2: Reduced orientation sampling space. (a) Fundamental zone for A20 lattice structure of α-U. Simulations were conducted at 10 K, 300 K and 600 K. (b) Fundamental for BCC structure of γ-U. Simulations were conducted at 900 K.

Figures 3.2(a) and 3.2(b) illustrate the fundamental zones for α- and γ-uranium respectively. As mentioned in the introduction, α-uranium exists in an uncommon anisotropic orthorhombic A20 crystal structure. While mirror symmetries are easily identified about the $\{100\}$ and the $\{001\}$ planes, the offset between atomic layers on $\{010\}$ planes eliminates any additional symmetry operations. By designating the near-centered atom as a PKA, the fundamental zone can be shown in Fig. 3.2(a) as the quarter-sphere about the PKA.

The high-temperature γ-uranium exists in a more common BCC structure, which has higher symmetry than the ground state α-uranium. Appropriately, the fundamental zone for γ-uranium is well defined, here presented in Fig. 3.2(b) as the $\frac{1}{48}^{\text{th}}$ sphere about the centered PKA atom. The projection of this fundamental zone is a standard stereographic triangle.

With the knowledge of the different fundamental zones for α- and γ-uranium respectively, a sampling scheme is needed to select a set of discrete recoil directions. There is, however, no consensus on the best sampling scheme to be used for this application.

The traditional sampling method [75, 80] consists of an incremental angle sweep in the spherical coordinate about the azimuthal angle θ and polar angle ϕ. However, such sampling scheme tends to cluster sampled orientations towards the poles ($\phi = 0$ and $\phi = \pi$) with sparse sampling around the equator ($\phi = \pi/2$) [98]. In turn, as pointed by Nordlund[77], this method requires either the further selection of specific directions with even solid angle representations, or using solid angle weights ($\sin\theta d\theta d\phi$) to calculate a weighted average of the sampled results.

An alternative sampling method [77, 81] is to select evenly distributed directions that lies within the fundamental zone. The set of directions can be either generated randomly or selected from a geodesic grid. Direction-specific threshold displacement energies calculated with this method can be easily combined with simple arithmetic averaging, but the coverage of the entire fundamental zone is not assured [81].

Instead of adapting either of the two aforementioned sampling methods, we develop a symmetry-informed orientation sampling scheme for more general applications. This method is herein referred to as the cubic subdivision sampling.

The cubic subdivision sampling method is based on the construction of iteratively refined geodesic polyhedra and using the even spaced vertices of the resulting polyhedron to sample fundamental zones. Geodesic polyhedra are refined by subdividing surfaces of simpler polyhedra and projecting the new vertices onto a spherical surface, as illustrated in Figs. 3.3(a)–3.3(c). Increasing the number of subdivisions also increases the resolution of the polyhedron to more closely approximate a sphere. By projecting the fundamental zone onto the subdivided polyhedron, a uniform orientation sampling scheme is generated by taking the overlapping vertices, as shown in Figs. 3.3(d)–3.3(e).

As indicated by the name of the sampling method, the choice of the initial polyhedron in the present configuration is a unit cube. The main advantage of selecting a unit cube as the starting polyhedron configuration is all the available symmetry operations it contains. These symmetry operations are preserved and transferred to the new polyhedron gener-

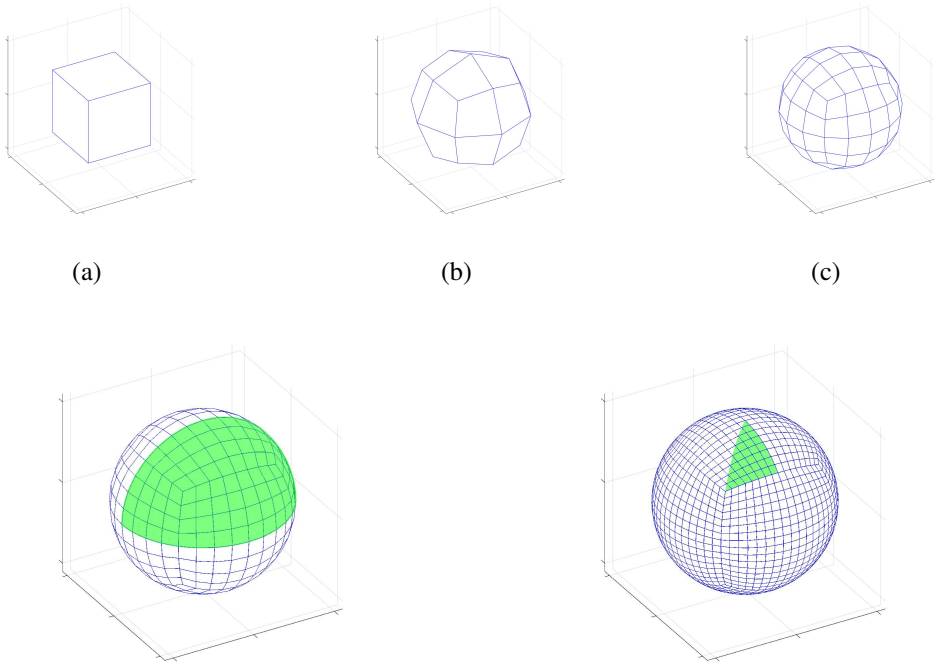

Figure 3.3: Cubic subdivision sampling. (a) Initial unit cube. (b) Spherical approximation after 1 subdivision. (c) Spherical approximation after 2 subdivisions. (d) Fundamental zone of α-U projected onto 4th divided polyhedron. (e) Fundamental zone of γ-U projected onto 5th divided polyhedron. Vertices of overlapping spherical approximations are taken as the PKA recoil directions.

ated by each subsequent subdivision. Since both A20 and BCC structures have subsets of cubic symmetries, their respective fundamental zones can easily be reconstructed within the various polyhedra originated from a unit cube. This is evident when overlaying the fundamental zones onto the surface of the polyhedra as shown in Figs. 3.3(d)–3.3(e), in which the polyhedron vertices perfectly align with the fundamental zone perimeters. The cubic subdivision sampling method is developed for general applications. Since all cubic, orthorhombic and tetragonal crystal lattices contain subsets of the full cubic symmetry, all possible fundamental zones of these lattices can also be constructed with the subdivided polyhedra. Adaptation of this orientation sampling scheme is beneficial to standardize various types of low-energy, lattice-dependent, threshold displacement studies.

To functionally illustrate the advantage of the cubic subdivision sampling method over

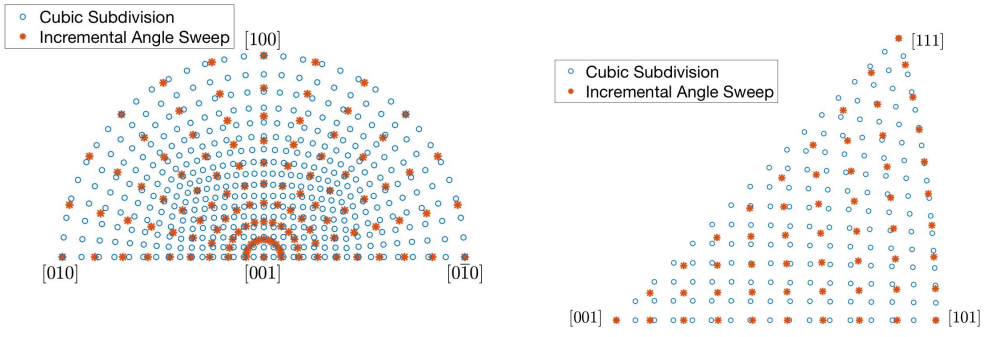

(a) A20 (b) BCC

Figure 3.4: Cubic subdivision and incremental angle sweep sampling methods comparison [75, 80, 89]. (a) A20 lattice sampling scheme comparison. (b) BCC lattice sampling scheme comparison. Points indicated available data at the recoil directions.

the traditional incremental angle sweep sampling method, the orientation distributions of data from the present work and that of Beeler [89] have been plotted as stereographic projections in Fig. 3.4. For both the α- and γ-uranium, the cubic subdivision sampling method is able produce a set of uniformly distributed directions across the entire fundamental zones. In contrast, Beeler's A20 sampled orientation data tend to cluster towards the $[001]$ direction, which is characteristic of the incremental angle sweep sampling method. In order to correct the sampling bias for the average threshold displacement energy calculations, solid-angle weights have to be introduced in the post-processing treatment of the results. However, as discussed later in Section 3.3, for the case of α-uranium, this can actually propagate the bias and affect the overall result. In the specific case of Beeler [89], the clustering towards to the pole is not as apparent in the data for BCC uranium, due to the combination of fine angle increments and a small fundamental zone. However, it is fairly apparent that the traditional incremental angle sweep method is incapable of producing several high symmetry orientations between the $[001]$ and $[111]$ directions. As a result, the associated threshold displacement energy distributions may not completely match the standard stereographic triangle, as later discussed in Section 3.3.

3.2.3 Definition of threshold displacement energy

As pointed out by Nordlund et al. [77], several definitions of threshold displacement energies can be considered.

The *direction-specific threshold displacement energy* ($E_{\mathrm{d}}(\theta,\phi)$) considers the value of the threshold displacement energy at each of the vertices of the geodesic mesh using the cubic subdivision sampling as described in Section 3.2.2. For the quarter sphere fundamental zone in α-uranium, a 4$^{\text{th}}$ subdivided polyhedron is used to sample 417 unique recoil directions for the direction-specific threshold displacement energies. For the $\frac{1}{48}$ sphere fundamental zone in γ-uranium, a 5$^{\text{th}}$ subdivided polyhedron is used to sample 153 unique recoil directions for the direction-specific threshold displacement energies. Directions yielding local minima in the threshold displacement energy are identified as defect channeling directions. Taking advantage of the relatively uniform sampling scheme of the present study, the *angle-averaged displacement threshold energy* ($E_{\mathrm{d}}^{\mathrm{ave}}$) can be directly calculated as the simple arithmetic average of all direction-specific threshold displacement energies $E_{\mathrm{d}}(\theta,\phi)$.

Alternatively, the *production probability threshold displacement energy* ($E_{\mathrm{d}}^{\mathrm{pp}}$) can be calculated by evaluating the recoil energy corresponding to the average defect production probability $P_{\mathrm{def,ave}}(E) = 50\%$, where $P_{\mathrm{def,ave}}(E) = \sum_i^{n_{\mathrm{dir}}} \frac{1}{n_{\mathrm{dir}}} P_{\mathrm{def}}(\theta_i,\phi_i,E)$, n_{dir} is the number of sampled directions, and $P_{\mathrm{def}}(\theta_i,\phi_i,E)$ is the direction-specific defect probability.

In a similar fashion, the *defect count threshold displacement energy* ($E_{\mathrm{d}}^{\mathrm{dc}}$) corresponds to the recoil energy at which the average stable defect count $N_{\mathrm{def,ave}}(E) = \sum_i^{n_{\mathrm{dir}}} \frac{1}{n_{\mathrm{dir}}} N_{\mathrm{def}}(\theta_i,\phi_i,E) = 0.5$, where n_{dir} is the number of sampled directions, and $N_{\mathrm{def}}(\theta_i,\phi_i,E)$ is the direction-specific defect count. As shown later in Section 3.3.2, both $P_{\mathrm{def,ave}}(E)$ and $N_{\mathrm{def,ave}}(E)$ behave identically for lower recoil energies, where the defect production and defect count are one-to-one. Differences between the two resultant E_d^{dc} and E_d^{pp} arise at higher recoil energies, where a single recoil event can create multiple FPs in its wake.

3.2.4 Defect analysis

Extraction of the point defects is performed using a Wigner-Seitz (W-S) defect analysis [99], as implemented in the OVITO software [100]. The W-S algorithm generates an initial set of Voronoi cells about all atoms in a reference, defect-free, configuration. During the cascade development, the now displaced atoms are binned into the reference Voronoi cells to generate new occupancy states. Point defects are then identified by each Voronoi cell's occupancy, with interstitial defects residing in cells with occupancy > 1 and vacancy defects residing in cells with occupancy < 1.

For each simulation, the final quenched configurations are used to identify the remaining stable defects. The quenching process serves as a mean to eliminate any thermal distortion that can interfere with defect binning. With respect to the 20 random temperature seeds at every recoil energy and direction, the defect probability (P_{def}) is defined as the fraction of simulations containing stable defects, and the defect count (N_{def}) is defined by the average number of stable FPs.

3.3 Threshold displacement energies in α- and γ-uranium

3.3.1 Directional dependence and channeling directions

Figure 3.5 shows two examples of defect probability distributions for α-uranium at 10 K and γ-uranium at 900 K respectively. Stereographic projection is used to condense the direction-specific defect probabilities into a pole figure representation. Discrete defect probabilities are converted into a continuous field though areal interpolation, resulting in the triangular tessellation features. It is important to note that, in the present work, all direction definitions are expressed relative to the unit sphere. Given the fact that α-uranium is non-cubic in nature, the directions would need additional conversion to be expressed in the lattice frame. The defect probability distributions for all other recoil energies, temperatures, and structural conditions are provided in the supplementary material information for

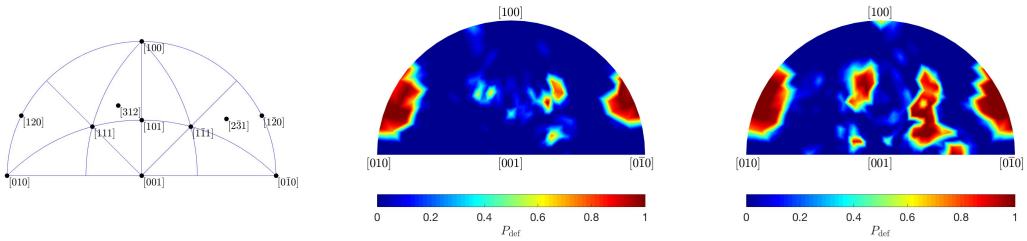

(a) A20 orientation key (b) A20 30 eV (c) A20 40 eV

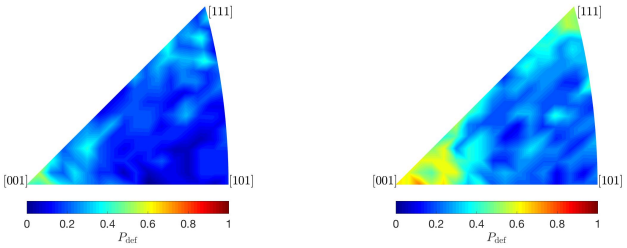

(d) BCC 20 eV (e) BCC 30 eV

Figure 3.5: Low energy cascade defect probability distributions. (a) A20 recoil direction key. (b) Defect probability distribution with 30 eV recoil PKA in α-U at 10 K. Emergence of defects is observed for the $[120]$ and $[1\bar{2}0]$ directions. (c) Defect probability distribution with 40 eV recoil PKA in α-U at 10 K. Emergence of defects is observed for the $[1\bar{1}1]$ and $[312]$ directions. (d) Defect probability distribution with 20 eV recoil PKA in γ-U at 900 K. Emergence of defects is observed for the $[001]$ directions. (e) Defect probability distribution with 30 eV recoil PKA in γ-U at 900 K. Emergence of defects is observed for the $[111]$ directions.

reference.

For all four temperatures presented in this study, our results for the threshold displacement energies distributions have demonstrated strong directional dependencies. Evidence of the direction anisotropy and defect channeling can be better seen in the low recoil energy defect probability distributions of Fig. 3.5. For the defect probability distribution of 30 eV recoils in α-uranium (Fig. 3.5(b)), high probability regions can be clearly identified in the two $[120]$/$[1\bar{2}0]$ directions. Similarly for 40 eV recoils in α-uranium (Fig. 3.5(c)), two additional high probability regions emerge in the $[1\bar{1}1]$ and the $[312]$ directions. These features are common to all α-uranium systems across the temperature range tested. With respect to the A20 lattice, shown in Fig. 3.2(a), these directions point at particular regional gaps in nearby stacking planes. Therefore, for α-uranium, the two near mirror $[120]$/$[1\bar{2}0]$ directions, the $[1\bar{1}1]$ direction and the $[312]$ direction are identified as the preferred defect channeling directions.

The defect probability distributions of 20 eV and 30 eV recoils in γ-uranium are also illustrated in Fig. 3.5(d) and 3.5(e) respectively. At 20 eV, the first high defect probability region appears in $[001]$ direction, a common defect channeling path in BCC metals. At 30 eV, there is a second observable high defect probability region in the $[111]$ direction. However, the $[111]$ direction is not a defect channeling direction, instead it points to the direction of the first nearest neighbor atom.

As indicated by Was [12], the simplest defect production probability as a function of recoil energy takes the form:

$$P_{\mathrm{def}}(E) = \begin{cases} 0 & \text{for} \quad E < E_{\mathrm{d}} \\ 1 & \text{for} \quad E > E_{\mathrm{d}} \end{cases} \tag{3.1}$$

However, with realistic account of lattice thermal vibrations, the discrete threshold becomes

blurred, and the defect production probability function becomes:

$$P_{\text{def}}(E) = \begin{cases} 0 & \text{for} \quad E < E_{\text{d}_{\text{min}}} \\ f(E) & \text{for} \quad E_{\text{d}_{\text{min}}} \leq E < E_{\text{d}_{\text{max}}} \\ 1 & \text{for} \quad E \geq E_{\text{d}_{\text{max}}} \end{cases} \tag{3.2}$$

Here, $E_{\text{d}_{\text{min}}}$ and $E_{\text{d}_{\text{max}}}$ represent the possible range of E_{d}, and $f(E)$ is a smooth varying function between 0 and 1. Since $f(E)$ is a cumulative distribution function(CDF) by nature, it can be directly fitted to various functional forms. In the present study, we choose a sigmoidal arctangent functional shape for $f(E)$ in Eq. (3.2) such that

$$P_{\text{def}}(E) = a \arctan(b \cdot E + c) + d, \tag{3.3}$$

where a, b, c, d are fitting parameters.

For each recoil direction, the fitted function $f(E)$ is evaluated at the 50 percentile to produce the direction-specific threshold displacement energies ($E_{\text{d}}(\theta, \phi)$). It is important to point out that, due to the division of sample size, the direction-specific threshold displacement energies do have significantly larger errors than the overall E_d. The direction-specific threshold displacement energies are plotted in a similar fashion as the defect probability distributions, using the stereographic projection. Figure 3.6 shows the comparison between our calculations of the direction-specific threshold displacement energies in γ-uranium with those of Beeler for the U MEAM interatomic potential [90], the U–Zr MEAM interatomic potential [91], and the U–Mo ADP interatomic potential [92] respectively. Further, Fig. 3.7 shows the comparison between our calculations of the direction-specific threshold displacement energies in A20 α-uranium with that of Beerler for the U–Mo ADP potential [92] at the temperature $T = 600$ K.

As previously stated when describing common orientation sampling techniques, due to the incomplete sampling of the BCC fundamental zone when using a traditional angle

sweep method employed by Beeler [89], the results for γ-uranium do not reflect the full set of crystallographic orientations as compared to those generated by the cubic subdivision sampling scheme employed here. That being said, with regards to the directional preference of threshold displacement energies, regardless of the fundamental zone sampling method used, a clear consensus can be identified amongst the four set of results generated with different interatomic potentials. Minima of threshold displacement energies all appear around $[001]$, the established defect channeling direction. The lower threshold displacement energy around the $[111]$ direction is also observed across the board, as illustrated in Fig. 3.6(e). Such behavior is expected, since defect channeling and recoil collision are purely determined by the lattice geometry.

The absolute values of direction-specific threshold displacement energies can vary depending on the interatomic potential used. In Fig. 3.6(e), the U MEAM threshold displacement energies appear as the clear outlier for γ-uranium. However, such result is not necessarily an indication of the inappropriateness of the interatomic potential used, since the U MEAM potential is the only one developed for the express purpose of modeling pure γ-uranium. In addition to describing uranium interactions, the U–Zr and U–Mo alloy potentials are fitted to include the behaviors of their alloy components. As such, the threshold displacement energies calculated with these two binary alloy interatomic potentials may be more applicable to describe threshold displacement energy in alloyed systems. Lastly, due to the fact that the U–Mo ADP potential was developed based on an older U EAM potential, results produced by the two are expected to be fairly close.

Matching behaviors previously shown in the Fig. 3.5, the α-uranium data sets in Fig. 3.7 all show defect channeling in the $[120]$/$[1\bar{2}0]$, $[1\bar{1}1]$, and $[312]$ directions. In addition, several high threshold displacement energies spots around the $[100]$, $[111]$ and $[2\bar{3}1]$ directions can be identified at the lower temperatures. Each of these directions approximately points toward a nearest neighbor lattice site, and is expected to produce a head-on collision, instead of channeling across the atomic plane.

Interestingly, there is one aspect of the direction-specific threshold displacement energies that does not agree between our study and one by Beeler [89]. What we are referring to is the relative sizes of the channel directions, shown as the low threshold displacement energy regions. Since channeling directions are almost exclusively determined by the lattice geometry, the only logical explanation of the difference is the orientation sampling bias. As previously stated, the incremental angle sweep sampling method has the tendency of over sampling around the pole and under sampling around the equator. Consequently, the solid angle weights must be introduced during the summation/integration process. This, however, actually exacerbated the poor orientation sampling in α-uranium, as more weights are placed upon channeling directions around the equator. This is also fairly evident in Fig. 3.7(d), since areal interpolation in the pole figure is conceptually similar to solid angle weighted integration.

3.3.2 Threshold displacement energies as a function of temperature

Figure 3.8 summarizes the overall defect generation statistics as a function of the recoil energies for different temperatures and phases. At each temperature and recoil energy, the average defect probability and average defect count were calculated by averaging over all direction-specific defect probabilities and direction-specific defect counts respectively. Defect count analyses were performed using the Wigner-Seitz technique described in Section 3.2.4. At lower recoil energies, the defect probability and defect count functions are nearly indistinguishable. At high energy recoils, the two functions diverge since a single recoil event is capable of generating multiple defect pairs. It is clear the defect probability and defect count functions at 600 K in α-uranium and at 900 K in γ-uranium have significantly faster initial rises than their counterparts at lower temperatures. This is attributed to the increased contribution of thermal vibrations at the higher temperatures weakening the lattice binding. For guaranteed defect production at all directions, the defect probabilities reach 99% at 161 eV for 900 K, 391 eV for 600 K, 483 eV for 300 K, and 494 eV for 10

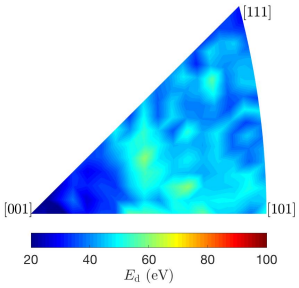

(a) U EAM 900 K

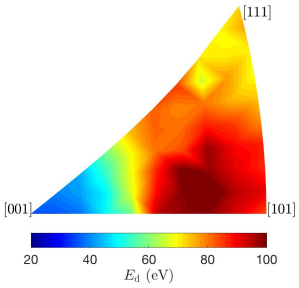

(b) U MEAM 800K*

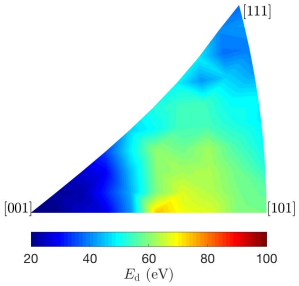

(c) U–Zr MEAM 800 K*

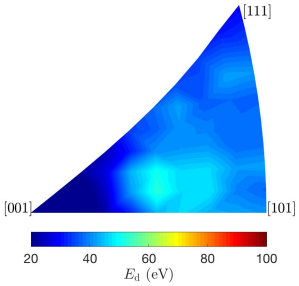

(d) U–Mo ADP 800 K*

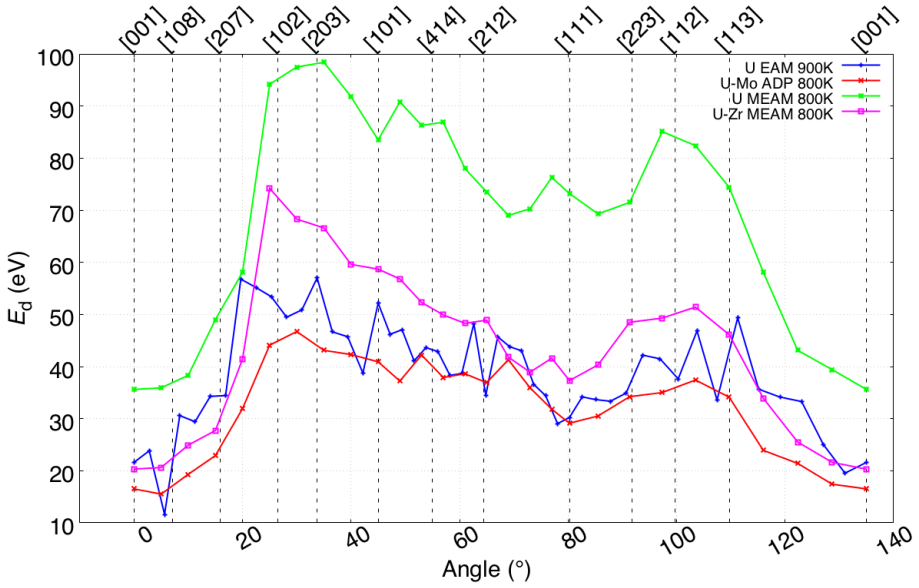

(e)

Figure 3.6: Direction-specific threshold displacement energies directional distributions for BCC γ-U. (a) Direction-specific E_d for γ-U at 900 K. (b) Direction-specific E_d for γ-U at 800 K with U MEAM potential. (c) Direction-specific E_d for γ-U at 800 K with U–Zr MEAM potential. (d) Direction-specific E_d for γ-U at 800 K with U–Mo ADP potential. (e) Direction-specific E_d for high symmetry directions. *Data obtained from Beeler [89].

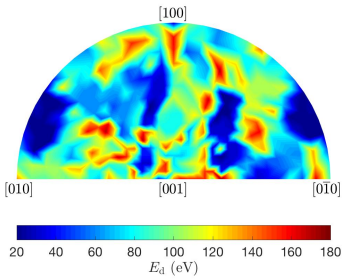

(a) U EAM 10 K

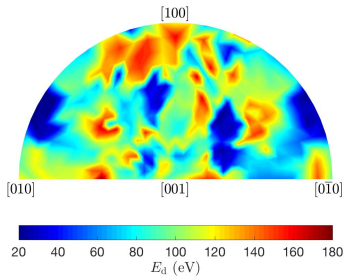

(b) U EAM 300 K

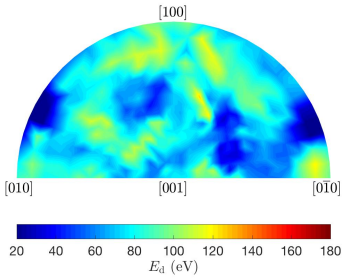

(c) U EAM 600 K

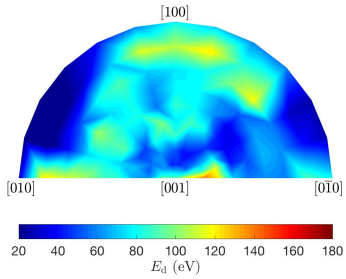

(d) U–Mo ADP 600 K*

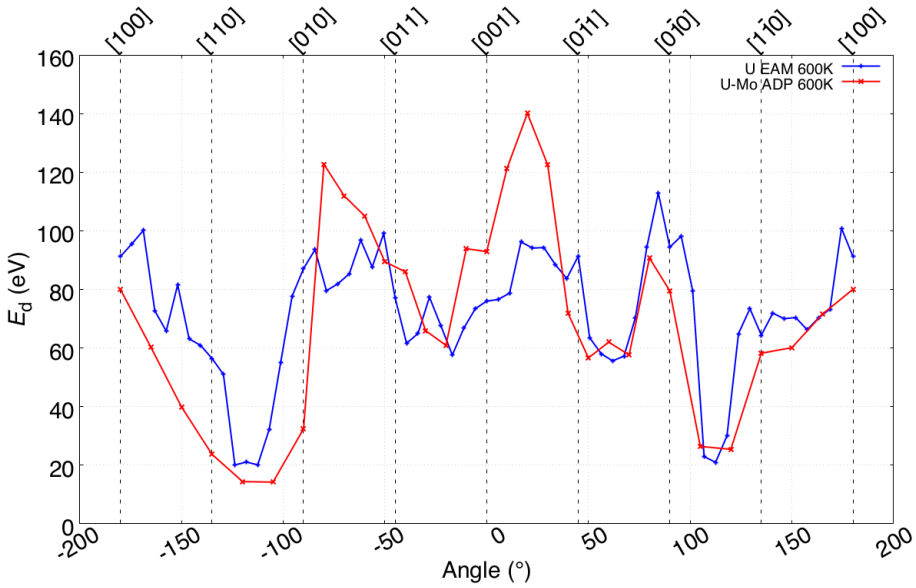

(e)

Figure 3.7: Direction-specific threshold displacement energies for A20 α-U. (a) Direction-specific E_d for α-U at 10 K. (b) Direction-specific E_d for α-U at 300 K. (c) Direction-specific E_d for α-U at 600 K. (d) Direction-specific E_d for α-U at 600 K with U–Mo ADP potential. (e) Direction-specific E_d for high symmetry directions. *Data obtained from Beeler [89].

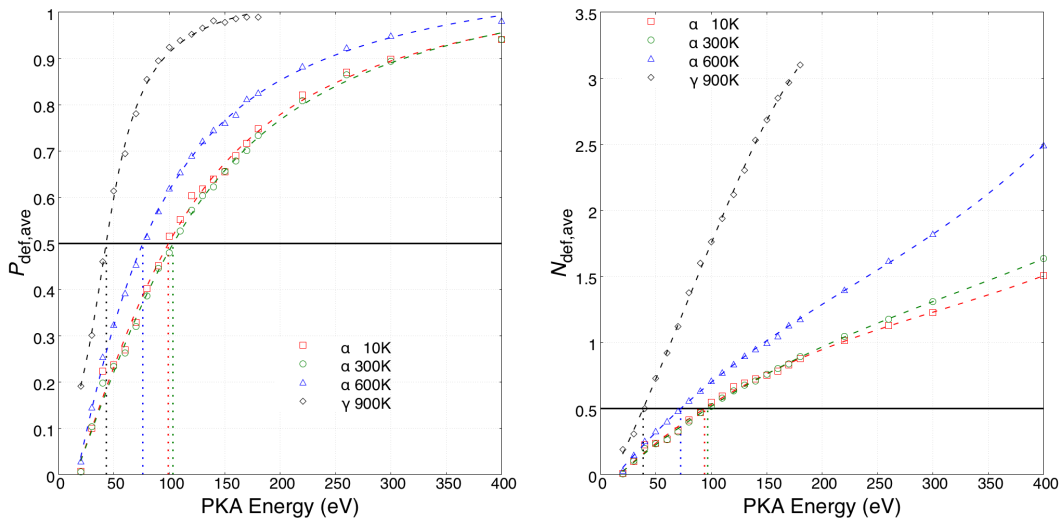

(a) (b)

Figure 3.8: Defect generation statistics at different phases and temperatures. (a) Average defect probabilities vs. initial PKA recoil energy. (b) Average defect counts vs. initial PKA recoil energy. Dashed lines correspond to the identification of the threshold displacement energies for the various configurations.

K.

In order to evaluate the various definitions of threshold displacement energy, the average defect probabilities and average defect counts are fitted to functions of PKA recoil energies. The average defect probabilities ($P_{\text{def,ave}}$) are fitted to arctangent functions with sigmoidal shape, as described in Eq. (3.3). The average defect counts ($N_{\text{def,ave}}$) are fitted to 4^{th} order polynomial functions. For each temperature, the fitted average probability function is evaluated at 50% to calculate the production probability threshold displacement energy E_{d}^{pp}, the fitted average defect count function is evaluated at 0.5 to calculate the defect count threshold displacement energy E_{d}^{dc}. E_{d}^{pp} extrapolated from the fits have been further confirmed by additional simulations with finer energy intervals to be within $\pm$ 2 eV of the true probability 50. Lastly, the angle-averaged threshold energy $E_{\text{d}}^{\text{ave}}$ is obtained through averaging all the direction-specific threshold displacement energies $E_{\text{d}}\left(\theta,\phi\right)$. Table 3.1 summarizes all sets of threshold displacement energies calculated in our study, along with results presented by Beeler [89] for comparison.

Comparatively speaking, the various definitions of E_{d} presented in the current study and the three $E_{\mathrm{d,med}}^{\mathrm{pp}}$ computed by Beeler always reside within the same energy range for a given temperature. However, considering the similarity between the U EAM and U–Mo ADP potentials, the differences should have been null. The consistent underestimation of E_{d} in the U–Mo ADP set is hypothesized to stem from two main factors: (i) the sampling bias previously discussed in Section 3.2.2, which overly weighted defect channeling directions in α-uranium therefore lowering the average threshold displacement energies, and (ii) the ZBL hardening of the interatomic potential at close range, which can strengthen collisions resistance and increase the threshold displacement energies [51].

Table 3.1: Threshold displacement energies (in eV) for different phases and temperatures. $E_{\mathrm{d}}^{\mathrm{ave}}$ is the angle-averaged threshold displacement energy . $E_{\mathrm{d}}^{\mathrm{pp}}$ is the defect production probability threshold displacement energy. $E_{\mathrm{d}}^{\mathrm{dc}}$ is the defect count threshold displacement energy. *Data presented by Beeler [89]. $*E_{\mathrm{d,med}}^{\mathrm{pp},(1)}$ is generated with the U MEAM potential [90]. $*E_{\mathrm{d,med}}^{\mathrm{pp},(2)}$ is generated with the U–Zr MEAM potential [91]. $*E_{\mathrm{d,med}}^{\mathrm{pp},(3)}$ is generated with the U–Mo ADP potential [92].

	$E_{\mathrm{d}}^{\mathrm{ave}}$	$E_{\mathrm{d}}^{\mathrm{pp}}$	$E_{\mathrm{d}}^{\mathrm{dc}}$	$*E_{\mathrm{d,med}}^{\mathrm{pp},(1)}$	$*E_{\mathrm{d,med}}^{\mathrm{pp},(2)}$	$*E_{\mathrm{d,med}}^{\mathrm{pp},(3)}$
α-U 10 K	84.2349	99.2659	93.9178	—	—	—
α-U 300 K	92.8530	103.4980	96.6990	—	—	—
α-U 600 K	74.3213	76.0915	72.4146	—	—	66.3
α-U 800 K	—	—	—	—	—	63.4
γ-U 800 K	—	—	—	73.2	47.1	35.6
γ-U 900 K	42.0137	42.9929	38.5157	—	—	—
γ-U 1000 K	—	—	—	68.9	41.3	32.8

A general decreasing trend can be observed in the threshold displacement energies calculated from 300 K to 900 K. This agrees with the hypothesis that the increase in lattice vibration weakens the lattice binding, leading to an increase in defect production. However, there is an exception to the trend when the temperature increases from 10 K to 300 K, where a small increase in threshold displacement energy is observed. To explain this initial hike in threshold displacement energy, the defect probability distributions at both temperatures are compared in Fig. 3.9. Specifically, the two plot distributions correspond to defect probabilities of $\sim 50\%$, which coincidently both match recoil energy of 100 eV.

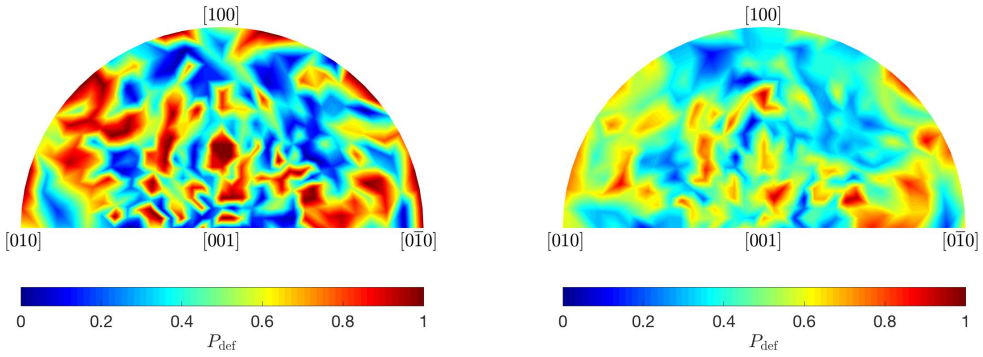

(a) α-U 10 K (b) α-U 300 K

Figure 3.9: Defect probability distributions near average defect probability of 50%. (a) Defect probability distribution of 100 eV recoil PKA at 10 K. (b) Defect probability distribution of 100 eV recoil PKA at 300 K.

As such, any existing difference can only be attributed to the difference in temperature.

Visual examination of Fig. 3.9(a) and Fig. 3.9(b) reveals the leveling of the probability distribution going from 10 K to 300 K. It is important to note that the leveling of distribution not only refers to the increases in defect probability in certain recoil directions (blue spots), but also the decreases in defect probability in other directions (red spots). The defect probability decreases are nowhere more apparent than in the $[120]$ and $[1\bar{2}0]$ and $[1\bar{1}1]$ defect channeling directions. These decreases in defect probability also signal the existence of a thermally dependent defect recovery mechanism. Indeed, this is referring to point defect diffusion, which causes more frequent interstitial-vacancy annihilations at 300 K than at 10 K. Going from a near static temperature 10 K to 300 K, the differences in point defect diffusion frequency can easily account for the initial hike in threshold displacement energy. However, comparatively speaking, the point defect diffusion mechanism is much weaker than the lattice vibration mechanism, since threshold displacement energies significantly decrease for $T_{\mathrm{ambient}} > 300$ K.

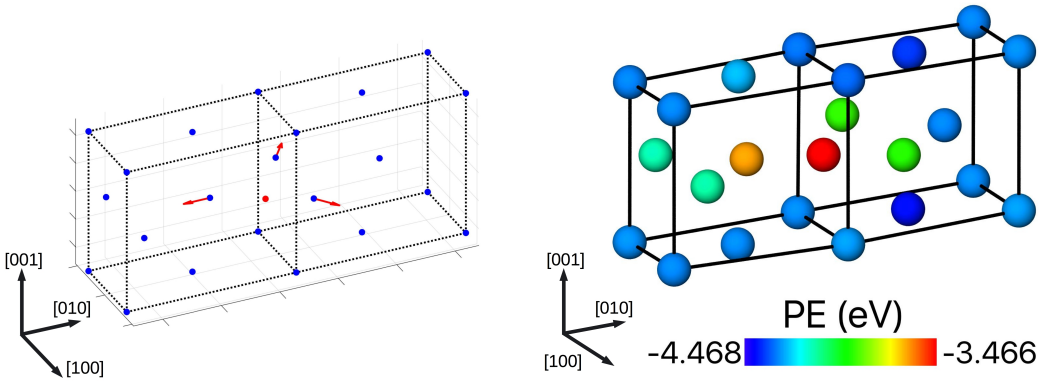

(a) (b)

Figure 3.10: A20 preferred interstitial site. (a) Nearest neighbor lattice distortion. (b) Nearest neighbor atom energetics. Interstitial atom is red in both cases.

3.3.3 Interstitial defect structures

With the knowledge of the defect channeling directions, we have further examined the various preferred interstitial defect configurations for both α- and γ-uranium. Presented alongside, each identified configuration is the self-interstitial formation energy $E_{\mathrm{I}}^{\mathrm{f}}$ calculated using:

$$E_{\mathrm{I}}^{\mathrm{f}} = E_{(n+1)} - \frac{n+1}{n} E_n, \tag{3.4}$$

where E_n represents the total energy of the perfect lattice system, $E_{(n+1)}$ represents the total energy of the same system with an additional interstitial atom.

For α-uranium, the most commonly observed interstitial defect configuration after annealing is shown in Fig. 3.10. Figure 3.10(a) illustrates the lattice distortions; Figure 3.10(b) illustrates neighboring energetics. The $\langle 010 \rangle$ dumbbell-like defect structure closely matches the stable *I5* interstitial configuration defined by Li [101] in orthorhombic uranium who used ab-initio simulation. The position of interstitial atom on the $\{001\}$ lattice planes also concurs with the appearance of the two $[120]/[1\bar{2}0]$ defect channeling directions. Simulation of the α-uranium defect structure at 10 K yielded $E_{\mathrm{I},\alpha-\mathrm{U}}^{\mathrm{f}} \approx 2.204$ eV. This is comparatively lower than several first principle calculations that predicted $E_{\mathrm{I},\alpha-\mathrm{U}}^{\mathrm{f}}$ to be in the range of 3.53 eV [102], 4.28 eV [101], and 4.42 eV [103].

For γ-uranium, no single preferred interstitial defect structure can be identified. Figures 3.11(a)–3.11(e) present the various ideal interstitial defect configurations in the BCC lattice. However, due to a combination of defect accommodation and thermal motion, attempts to the categorize the simulated interstitial defect structures have proven to be rather futile. Figure 3.11(f) illustrates the simulated dumbbell defect structure. The classification of of this defect structure falls in between a $\langle 110 \rangle$ dumbell (Fig. 3.11(d)) and a $\langle 111 \rangle$ dumbbell (Fig. 3.11(e)). Similarly, defect configuration shown in Fig. 3.11(g) can be identified as either a tetrahedral interstitial (Fig. 3.11(a)) or a $\langle 110 \rangle$ dumbbell (Fig. 3.11(d)). Finally, Figure 3.11(h) presents an octahedral interstitial defect structure (Fig. 3.11(b)) that's not dissimilar to a $\langle 100 \rangle$ dumbbell (Fig. 3.11(c)).

This interchangeability of various defect configurations in γ-uranium can be explained when examining the defect energetics at 900 K. Equation 3.4 is once again used to calculate the interstitial formation energy $E^{\mathrm{f}}_{\mathrm{I},\gamma-\mathrm{U}}$. First, E_n is first determined for a pristine $8 \times 8 \times 8$ BCC superlattice with 1024 atoms, then, $E_{(n+1)}$ is calculated after introducing an additional interstitial atom. The resultant $E^{\mathrm{f}}_{\mathrm{I},\gamma-\mathrm{U}} \approx 0.325$ eV, which is a magnitude lower than that of the α-uranium. This, however, does agree with the first principle calculation done by Beeler [104]. The small $E^{\mathrm{f}}_{\mathrm{I}}$ value not only explains the concurrence of the multiple defect configurations, but also reflects the decreased threshold displacement energies in γ-uranium.

3.4 Conclusion

In this study, we have evaluated the threshold displacement energy of metallic uranium as functions of both recoil direction and temperature. Due to the uniqueness of the crystallographic structure, we have placed a special focus on the lower temperature α phase.

We developed a novel crystal symmetry-informed, cubic subdivision sampling method to select directions to study the directional dependency. This method takes full advantage of symmetry preservation during cubic subdivisions to create orientation sampling

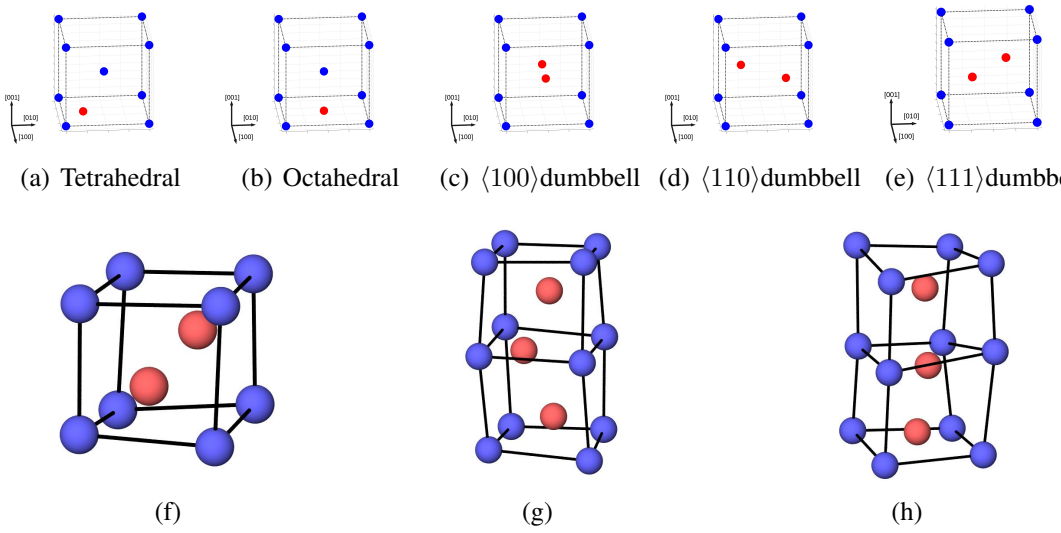

(a) Tetrahedral (b) Octahedral (c) $\langle 100 \rangle$dumbbell (d) $\langle 110 \rangle$dumbbell (e) $\langle 111 \rangle$dumbbell

(f) (g) (h)

Figure 3.11: BCC interstitial configurations. (a) Tetrahedral interstitial site. (b) Octahedral interstitial site. (c) $\langle 100 \rangle$ dumbbell interstitial. (d) $\langle 110 \rangle$ dumbbell interstitial. (e) $\langle 111 \rangle$ dumbbell interstitial. (f) Simulated $\langle 110 \rangle$/$\langle 111 \rangle$ dumbbell interstitial. (g) Simulated tetrahedral/$\langle 110 \rangle$ dumbbell interstitial. (h) Simulated octahedral/$\langle 100 \rangle$ dumbbell interstitial.

schemes for two distinct cubic structure of A20 and BCC. This method is general and adaptable to any crystallographic system with cubic, tetragonal or orthorhombic symmetry. The relative uniformity of sampling schemes provided by this methodology reduces the calculation complexity of the threshold displacement energies, by allowing unweighted averaging across all samples. In comparison to a similar threshold displacement study in uranium [89], this method proves to be a clear improvement over the traditional sampling technique such as angle sweep or random orientation selection, retaining none of the inherent sampling biases.

We have calculated threshold displacement energy in metallic uranium using several definitions. The most commonly used production probability threshold displacement energy $E_{\mathrm{d}}^{\mathrm{pp}}$ is calculated as approximately 99.2659 eV at 10 K (α-U), 103.4980 eV at 300 K (α-U), 76.0915 eV at 600 K (α-U), and 42.9929 eV at 900 K (γ-U). With exception of those calculated at 10 K, threshold displacement energies greatly decrease with increasing temperature. Such observation highlights the negative effects of thermal vibration on

radiation resistance, with respect to the initial defect production timeframe. Additionally, our analyses of the direction-specific defect probability and direction-specific threshold displacement energy have confirmed the presence of defect channels at $[120]$, $[1\bar{2}0]$, $[1\bar{1}1]$ directions for α-uranium and $[001]$ direction for γ-uranium. The directional variation in threshold displacement energies remains consistent across the temperature range, however, as temperature increases, the availability of defect channeling directions decreases.

Finally, using the Wigner-Seitz defect analysis, we have examined the common interstitial defect structures for threshold displacements in α- and γ-uranium. For α-uranium, the single observed defect structure has the interstitial atom laying near the $\{001\}$ lattice plane, closely matching the interstitial site predicted by previous DFT calculations [102, 101, 103]. For γ-uranium, all observed defect structures are meta-stable due to the increased thermal motions and lattice accommodations. The high temperature state and low interstitial formation energies also indicate a relative ease in transition between different defect configurations.

CHAPTER 4
REDUCED-ORDER ATOMISTIC METHOD FOR SIMULATING HIGH DOSE IRRADIATION IN METAL

As initially stated in Chapter 1, in order to accurately study radiation material aging, it is necessary to **develop a new atomistic method of simulating defect accumulation and material aging over large doses.** Here we have expanded the proposal made in Chapter 2, and implemented the new Reduced-Order Atomistic Cascade (ROAC) method for simulating dose accumulation in metals. Using the arc damage model [48] as the foundation, ROAC generates radiation damage as reduced-order core-shells, with the core presenting the thermal spike, and the shell representing the ballistic point defects. We illustrate the predictability and accuracy of ROAC for the cases of copper and niobium by comparing its results with those from full collision cascades. Scalability of the method is demonstrated for examples of high energy cascade fragmentation and heavy-ion bombardment. In an effort to examine the radiation aging at phase boundaries, the heavy-ion bombardment model was also adapted for Cu–Nb multilayers in Chapter 7, .

4.1 Introduction

The effects of irradiation on materials are rooted in the initial event in which an incident energetic particle transfers its energy to a materials by colliding with the target lattice atoms. This event subsequently develops in several processes (primary knock-on atom (PKA), additional knock-ons, displaced atoms, production of displacement cascades) leading to the creation and evolution of materials damage in the form of point defects, dislocation loops, defect clusters and voids [12]. The presence of these defects can cause chemical and physical changes in materials properties such as swelling, phase change, or embrittlement for example [9]. Accurate and predictive models that can quantify the extent of radiation

damage and provide a physical description of these interaction processes are crucial for understanding the effects of irradiation.

Molecular dynamics (MD) and binary collision approximation (BCA) simulations are routinely employed to model radiation effects in the early stages following a single radiation event [99, 105, 106, 107]. While the process of modeling individual displacement cascade using these techniques seems straightforward, several restricting factors still prevent us from directly upscaling results from atomistic models to length and dose scales comparable to experiments [108].

The first challenge associated with modeling radiation damage lies in the necessity to scale the size of the simulation domain with the PKA energy. In order to prevent self-interaction across periodic boundaries and artificial shock waves due to the deposition of energy, a typical simulation cell is constructed with dimensions several times larger than the maximum size of the cascade. While low energy cascades can be contained to relatively small simulation cells, high energy cascades may require up to tens or hundreds of millions of atoms [109]. This limitation of size scaling also persists in damage accumulation model with multiple PKA events [52]. In order to prevent the unrealistic thermal interactions between two or more simultaneous cascades, sufficiently large time lapses must be accounted for between events, restricting the equivalent simulated damage rate.

Compounding the issue of scaling the computational domain, is the need to use a computationally demanding adaptive time stepping for those simulations. The high velocity involved in the atomic collisions significantly increases the computational cost in the first stage of cascade development (ballistic phase). For the standard atomic motion integration in a MD simulation, the time step (Δt) is determined by the maximum displacement amongst all of its atoms. A time step too large can be detrimental to the stability of a simulation by missing collisions or causing near atom overlaps that result in artificial thermal explosions. This is especially true when modeling high energy PKAs, where Δt at the early stage of the cascade development needs to be several orders of magnitude smaller than that

at thermal equilibrium (generally on the order of tens of attoseconds). The multiplicative combination of the large simulation domain and small Δt can be extremely computational expensive until the initial PKA energy is dispersed and distributed by secondary collisions. As such, algorithms such as the Cell Molecular Dynamics for Cascade (CMDC) [110] have been recently pursued in order to reduce the computational cost through the isolation of regions with active motions.

Lastly, the atomistic modeling of displacement cascades also presents a severe restriction on the choice of interatomic potentials. To accurately simulate the process of high energy/velocity collisions, an interatomic potential appropriate for cascade modeling must be fitted to the Ziegler-Biersak-Littmark (ZBL) nuclear repulsion interaction [50] at close range. However, this is not a common practice in interatomic potential development when radiation damage is not of interest. While the ZBL modification can be easily added to existing Embedded-Atom Method (EAM) potential by tapering the electron density and fortifying the pair interactions at close range for example, the resultant changes in defect properties often necessitate the revalidation of the potential as a whole [51]. In addition to the standardized EAM format, more advanced/complex potentials (MEAM [111], COMB [112], ReaxxFF [113]) are available for modeling defect formation in metals, but their significantly increased computational costs realistically restrict their applications to low energy, single recoil models.

Alternative methods of modeling radiation damage have been proposed to circumvent the above mentioned challenges. Among those, the Frenkel Pair Accumulation (FPA) method [58] is one such accelerated method of modeling radiation damage accumulation that bypasses the displacement cascade process altogether. In lieu of modeling the computationally expensive atom collisions, stable Frenkel pairs are directly generated by displacing atoms from their original lattice sites, matching the final recovered state of the system. Applications of the FPA method to Urania and other ceramic systems [58, 114] have shown to be able to correctly replicate early stages of radiation defect evolutions observed in ex-

periments. While the method is fairly accurate for materials systems with sparse defect generation, it is incapable of reproducing some characteristic defects in dense metallic systems. For example, we have shown in a previous study [115] that the introduction and accumulation of spatially distributed point defects in hexagonal zirconium could only replicate majority c-component type dislocations, representative of low energy electron irradiation conditions. Larger defect clusters, typically expected after a few ion strikes [61], only appeared at higher dose levels, after significant accumulation and migration of point defects have occurred.

Fundamentally, the inability of the FPA method to predict correct defect clusters formation can be attributed to the absence of the effects of the thermal spike [48] that occurs in the early stages following a PKA event. The thermal spike is defined as the contiguous liquid-like amorphous pockets formed in dense materials as the result of the destabilization of local lattices. The supersonic thermal shocks emitted from a thermal spike are responsible for the formation of defect clusters from high energy recoil events [61]. Furthermore, due to the atomic mixing displacement that occur within each thermal spike, significant point defect annihilation is expected, should any existing Frenkel pairs overlap with a cascade [116]. In other words, the incorporation of the effects of a thermal spike is crucial not only to accurately account for the initial formation of defect clusters at low doses, but also to capture the long term saturation of damage contents at high doses.

Building up from the idea behind the FPA method, we describe here a reduced-order atomistic cascade model that integrates the effects of the thermal spike process in order to predict and replicate radiation events in metals across a wide range of recoil energy. To that end, we approximate cascade and displacement damage production by modeling the cascade as a core-shell structure describing two damage production estimators, namely an athermal recombination corrected displacements per atom (arc-dpa) estimator in the shell and an atomic mixing estimator in the core. Our model is calibrated using explicit MD PKA simulations for a broad range of recoil energy. Similarly to the FPA method, the ap-

proximated cascade structure can be directly incorporated into an atomic system, bypassing the computationally expensive early stage of the cascade formation. By reproducing more holistically the formation of displacement cascades, the present method is able to achieve more realistic defect production without loss of accuracy of the results, while retaining the necessary speed to simulate large doses.

First, we describe how the two damage production estimators are calibrated to explicit MD PKA simulations in Section 4.2. The two estimators are based on a recent standard for quantifying atomic displacement levels in irradiated materials that extends the Norgett-Robinson-Torrens displacements per atom (NRT-dpa) model [63, 48]. In 4.3, we then present our implementation of the reduced-order atomistic cascade model. In particular, we discuss the specifics of inserting cascades within a computational domain (Sec. 4.3.1) and we provide a verification and validation comparison (Sec. 4.3.2) with results from full MD PKA simulations over a broad range of recoil energies (500 eV–50 keV). We then demonstrate the applicability of our methodology in Section 4.4 by providing examples where we simulated high energy cascade fragmentation (Sec. 4.4.1) and large dose ion-bombardment (Sec. 4.4.2) using this technique. In the last section (Sec. 4.5), we provide a discussion on the various practical considerations and challenges associated with this methodology especially when simulating subcascade formation and dose effects.

4.2 Explicit primary knock-on atom cascade simulations and damage production estimators

The main difference between a standard MD PKA simulation and our methodology is the way the displacement cascades formation is described. In our methodology, we approximate a displacement cascade as a core-shell structure bypassing the early ballistic stage from standard MD simulations. This core-shell structure is calibrated in order to reproduce the same amount of defects as the one obtained from explicit MD PKA simulations. The calibration makes use of two damage production estimators derived from a recently

proposed modified NRT-dpa defect production model [48]. Based on observations on radiation defect generation mechanisms obtained from MD simulations [99, 117, 118, 119], this modified NRT-dpa defect production model provides more physically realistic descriptions of primary defect creation in metals by describing both the in-cascade recombination effects on defect production (termed as the athermal recombination corrected dpa, or arc-dpa) and the atomic mixing due to the heat spikes during cascade development (termed as the replacements-per-atom, or rpa). In this model, the predicted number of atomic displacements (N) as a function of the recoil energy T of the cascade takes the form,

$$N_{\mathrm{dpa/rpa}}(T) = \begin{cases} 0 & \text{for} \quad T < E_{\mathrm{d}} \\ 1 & \text{for} \quad E_{\mathrm{d}} < T < \frac{2E_{\mathrm{d}}}{0.8} \\ \frac{0.8T}{2E_{\mathrm{d}}}\xi_{\mathrm{dpa/rpa}} & \text{for} \quad \frac{2E_{\mathrm{d}}}{0.8} < T < \infty \end{cases} \tag{4.1}$$

and,

$$\xi_{\mathrm{dpa}}(T) = \frac{1 - c_{\mathrm{dpa}}}{(2E_{\mathrm{d}}/0.8)^{b_{\mathrm{dpa}}}} T^{b_{\mathrm{dpa}}} + c_{\mathrm{dpa}}, \tag{4.2}$$

$$\xi_{\mathrm{rpa}}(T) = \left[\frac{b_{\mathrm{dpa}}^{c_{\mathrm{rpa}}}}{(2E_{\mathrm{d}}/0.8)^{c_{\mathrm{rpa}}}} + 1 \right] \frac{T^{c_{\mathrm{rpa}}}}{b_{\mathrm{rpa}}^{c_{\mathrm{rpa}}} + T^{c_{\mathrm{rpa}}}}, \tag{4.3}$$

where E_{d} is the threshold displacement energy, and b_{dpa}, c_{dpa}, b_{rpa} and c_{rpa} are material specific constants determined from MD simulations or experiments. The coefficient b_{rpa} is related to the average subcascade formation energy (energy units), while b_{dpa} and c_{rpa} (unitless) are related the non-linear dependence with respect to the threshold displacement energy. The coefficient c_{dpa} (unitless) is related to the saturation of damage recombination. Fitted coefficients in the case of copper (Cu) and niobium (Nb) are provided in 4.1. The function ξ_{dpa} represents the fraction of surviving defects due to the athermal recombination, while the rpa correction factor ξ_{rpa} accounts for the so-called radiation mixing and expands upon the classical NRT prediction to estimate the total number of atoms that experience replacement shuffling, i.e., the number of atoms displaced by the thermal spike and

recovered to new non-defect lattice sites. Detailed derivations of these expressions can be found in the original paper [48].

Table 4.1: Material constants for modified modified NRT-dpa defect production model in Eqs. 4.1–4.3.

	E_{d} (eV)	b_{dpa}	c_{dpa}	b_{rpa} (eV)	c_{rpa}
Cu	50.0	-1.070 $\pm$ 0.0753	0.200 $\pm$ 0.0081	3359.3 $\pm$ 229.8	1.27 $\pm$ 0.0241
Nb	56.0	-0.485 $\pm$ 0.0270	0.172 $\pm$ 0.0155	2627.5 $\pm$ 311.1	1.11 $\pm$ 0.0403

To fit this modified NRT-dpa model, we used the MD code Large-scale Atomic/Molecular Massively Parallel Simulator (LAMMPS) [93] to perform simulations of single PKA displacement cascades for initial recoil energies E_{PKA} ranging from 0.5 keV to 50 keV in the case of Cu and Nb. We have selected a binary Cu–Nb EAM potential [49] which emphasizes high temperature liquid-phase thermodynamics in order to model appropriately the mixing process that occurs within a thermal spike. This potential also accounts for nuclear stopping by being fitted with the close-range ZBL nuclear repulsion. Electronic stopping power effects are also incorporated via a frictional drag force as a function of the atomic velocity applied to atoms with kinetic energy ≥ 10 eV as described elsewhere [108].

Table 4.2: List of MD PKA simulations from initial recoil energy (E_{PKA}) ranging from 500 eV to 50 keV. $N_{\mathrm{simulation}}$ – Number of simulations performed, L^i – Simulation cell size in lattice units for material "i", N^i_{atom} – Total number of atoms within the computation domain for material "i".

E_{PKA}(keV)	$N_{\mathrm{simulation}}$	L^{Cu}	$N^{\mathrm{Cu}}_{\mathrm{atom}}$	L^{Nb}	$N^{\mathrm{Nb}}_{\mathrm{atom}}$
0.5	100	20^3	32,000	30^3	54,000
1	100	20^3	32,000	30^3	54,000
2	100	30^3	108,000	40^3	128,000
5	100	30^3	108,000	40^3	128,000
10	100	50^3	500,000	60^3	432,000
20	50	60^3	864,000	80^3	1,024,000
50	50	80^3	2,048,000	100^3	2,000,000

For all the explicit MD PKA simulations conducted, we used periodic boundary conditions to simulate a cascade isolated in the bulk. The dimensions of the simulation cell were scaled with E_{PKA} as to avoid cascade self-interaction (see sizes of simulation cell in 4.2).

Prior to the PKA initiation, the crystalline lattice was first equilibrated and thermalized using an isothermal-isobaric (NPT) ensemble at $T = 300$ K and zero pressure $P = 0$ Pa for 200 ps. After this step, we initiated the displacement cascade by randomly choosing a PKA near the center of the simulation box and assigning it a velocity in a random direction corresponding to the initial recoil energy E_{PKA}. The time evolution of the displacement cascade was performed in an isochoric and constant energy ensemble (NVE) with an adaptive time step (10^{-10} ps $\leq \Delta$t $\leq 10^{-4}$ ps) with a maximum atomic displacement set to 0.05 Å for the first 0.5 ps. This early adaptive time stepping was meant to capture the high velocity collisions. The time step was then switched to a constant time step of $\Delta t = 10^{-3}$ ps for the remainder 19.5 ps of the simulation to allow for the cascade to further develop. The excess energy due to the cascade insertion was removed from the atomic system by using an over-dampened Langevin thermostat for all atoms within 10 Å of the periodic boundaries. Finally, each simulation was followed by a fast quenching down to 0 K in order to remove any residual thermal distortion for defect analysis. Multiple simulations with random PKA directions and thermal seeds were conducted for a given E_{PKA} to generate a sufficient defect statistics. A complete list of the MD displacement cascade simulations is provided in 4.2 for both Cu and Nb. It is important to distinguish here that the initial recoil energy of the PKA is designated as E_{PKA} in 4.2, rather than as T shown in Eq. 4.1. This is intentional, since the modified NRT-dpa model only considers the lattice energy deposition for the formation and growth of thermal spikes. For example, by subtracting out the total energy lost due to the electronic stopping, the actual recoil energy T for a cascade simulation for 50 keV recoils in Cu can be up to $\sim 5\%$ to 7% lower than E_{PKA}, and $\sim 10\%$ to 12% lower in the case of Nb.

In 4.1, we show the number of defect/displaced atoms as a function of the damage energy for both Cu and Nb as identified from our MD simulations and the corresponding calibrated fits from Eq. 4.1. Defects for the arc-dpa model were identified using a classical Wigner Seitz analysis from the quenched configuration. Mixing displaced atoms from the

rpa model were identified as atoms that were displaced from their original lattice sites, but that did not form any interstitial defect. The threshold displacement energies E_d for both Cu and Nb were calculated using a uniform orientation sampling method described elsewhere [62]. The median values of E_d at 0K for Cu and Nb were estimated to be 50 eV and 56 eV respectively. While E_{d} values can differ with potentials and calculation methods, the material constants are largely insensitive to the difference due to damage productions being heavily weighted towards higher recoil energies. The functional forms presented in Eqs. 4.1-4.3 have been fitted to the number of defect/displaced atoms obtained from these MD simulations results. The materials coefficients are provided in 4.1. Our results are comparable to those reported elsewhere [48] and differences can be attributed to the interatomic potential used as well as the large statistical spread in the defect production stemming from the simulations.

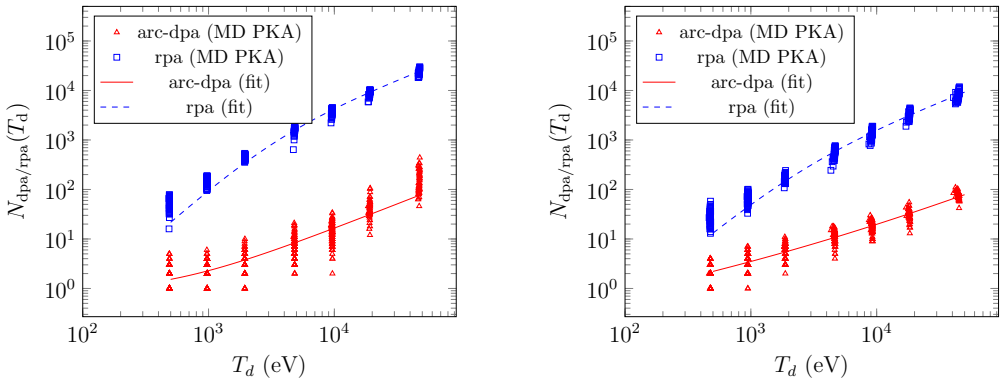

(a) FCC Cu (b) BCC Nb

Figure 4.1: Defect production (arc-dpa & rpa, see Eqs. 4.1-4.3) for energies ranging from 500 eV to 50 keV in (a) Cu and (b) Nb. Dash lines are fitted rpa functionals to the atomic mixing damage production estimator. Solid lines are fitted arc-dpa functionals to the defect damage production estimator. Variations in T_{d} are due to the removal of electronic stopping energy loss.

4.3 Reduced-order method for simulating cascades

4.3.1 Equivalent cascade atomic structure

The central idea to our reduced-order atomistic cascade method (ROAC) for simulating radiation effects in metals is based on observations from MD simulations of the time-dependent evolution of a displacement cascade in many metallic systems: following the ballistic and thermal phases occurring in the early stage of an isolated PKA displacement cascade, as the cascade cools down, almost all atoms regain positions in the perfect lattice sites. The actual amount of final defects left behind can be categorized into a long-range ballistic defect damage (arc-dpa type of damage) on the periphery of the hot cascade core and a short-range thermal spike mixing damage (rpa type of damage). These two damage estimators can be approximated as a core-shell structure where the amount of damage in the shell corresponds to arc-dpa damage production and the amount of damage in the core corresponds to the rpa damage production. By directly replicating these two final damage states, the high-velocity early cascade development is effectively bypassed, reducing the overall computational costs.

This configurational construct works as followed. After equilibrating and thermalizing a large simulation cell with periodic boundary conditions, we begin by calculating $N_{\mathrm{dpa}}(T)$ and $N_{\mathrm{rpa}}(T)$ for a given recoil event with energy T using Eq. 4.1. We then use the summation of these two damage production estimators to determine the approximated size of the core-shell cascade structure ($N_{\mathrm{cascade}} = N_{\mathrm{dpa}} + N_{\mathrm{rpa}}$). The center of this cascade is randomly located within the simulation domain with the N_{cascade} nearest neighbors designated as the spherical core. In order to replicate the production of supersonic ballistic point defects [120], we then randomly displace N_{dpa} atoms from the core into an outer shell 5 Å to 10 Å outside the core, such that thermal shocks emitted by the thermal spike can still interact with the interstitial defects and enhance migration/clustering.

Within the core, we distribute the PKA energy T in order to replicate the atomic mix-

ing due to the thermal spike and the associated dispersion of energy. To that end, we scale the core temperature (T_{core}) of the remaining N_{rpa} core atoms to $T_{\text{core}} = \frac{2}{3k}(\frac{3}{2}kT_{\text{ambient}} + \frac{T}{N_{\text{cascade}}})$, where k is the Boltzmann constant and T_{ambient} is the ambient simulation temperature. This step instantaneously redistributes the large recoil energy T of a single PKA to the entire population of the core of the cascade, thus eliminating the need to simulate any expensive, high velocity collision. We subsequently relax these energized N_{rpa} atoms using a NVE ensemble, allowing unrestricted mixing, recovery, and expansion within the spherical core region of the approximated cascade. We note here that, while it is possible to achieve even greater computational speed by simulating core mixing with on-lattice atom shuffles, the elimination of the time-integrated thermal relaxation is ill-advised. Indeed, MD studies of displacement cascades have repeatedly shown that the presence of a thermal spike is responsible for not only the amorphization and phase transformation of polymorphic metals and ceramics [60], but also the creation of large interstitial cluster ahead of the thermal shock fronts [61]. Many of these processes remain dynamic and unpredictable due to the stochastic nature of thermodynamic interactions between atoms.

Regarding the shell and the remainder of the simulation cell, given that the core already represents the maximum mixing damage expected from a recoil event, the relaxation outside the core needs to contain the further expansion of the core and reduce unintended excess atomic shuffling. To that end, we apply an over-dampened Langevin thermostat to all the atoms outside the core, as opposed to just the boundaries of the simulation cell as it would be the case in an explicit PKA MD simulation. As a result of the increased thermal dampening throughout the simulation cell, the thermal shocks emitted by the core terminate quickly near its vicinity, making individual recoil event significantly more compact. This is an advantage to this method when modeling dose accumulation, as multiple recoil events can be inserted simultaneously, on the condition that core regions do not overlap. Lastly, after a 20 ps relaxation, the simulation is quenched down to 0K and minimized for defect extraction and analysis.

4.3.2 Damage production from approximated cascades

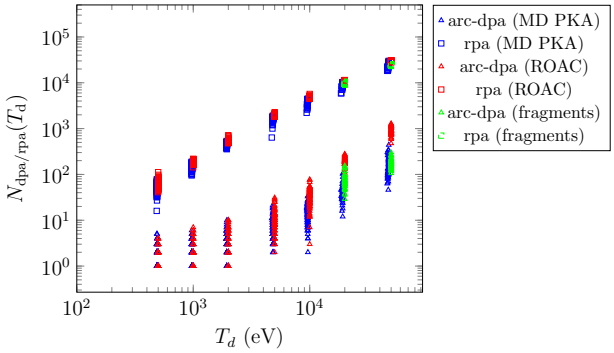

(a) FCC Cu

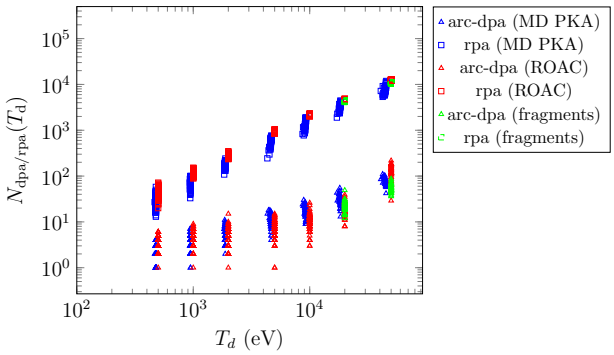

(b) BCC Nb

Figure 4.2: Comparison of damage production between explicit MD PKA simulations and the reduced-order atomistic cascade (ROAC) method for simulating cascades for energies ranging from 500 eV to 50 keV in (a) FCC Cu and (b) BCC Nb. Symbols in green correspond to the insertion of multiple subcascades at high recoil energies as described in 4.4.1.

We verified and validated the predictability and accuracy of the reduced-order atomistic cascade model described above by carrying out a series of simulations comparing the results of our methodology with those from explicit MD PKA simulations. We show in Fig. 4.2 a direct comparison between the two methods for the arc-dpa and rpa damage production estimators over a broad range of recoil energies. In terms of the number of replaced atoms in the core (rpa metric), we note a good agreement between the results in both cases for Cu and Nb across the energy spectrum tested. In most cases, our reduced-order atomistic cascade model produces a slightly higher average number of replaced atoms N_{rpa}

compared to explicit cascade simulations which is expected due to the imperfect containment of the thermal spike induced shock. By contrast, the number of the surviving defect in the shell of the cascade (arc-dpa metric) generated by the two methods are similar for low recoil energies, but tend to diverge for $T \geq 10$ keV. These differences at higher energies can be attributed to the inaccurate single thermal spike assumption employed in our methodology. If instead, for those high recoil energies, the approximated cascade is broken up into multiple 10 keV cascades, then the combined number of surviving defects N_{dpa} produced from these subcascades matches well those produced from the explicit MD cascade simulations. Further discussion on cascade fragmentation and subcascade representation is provide in 4.4.1.

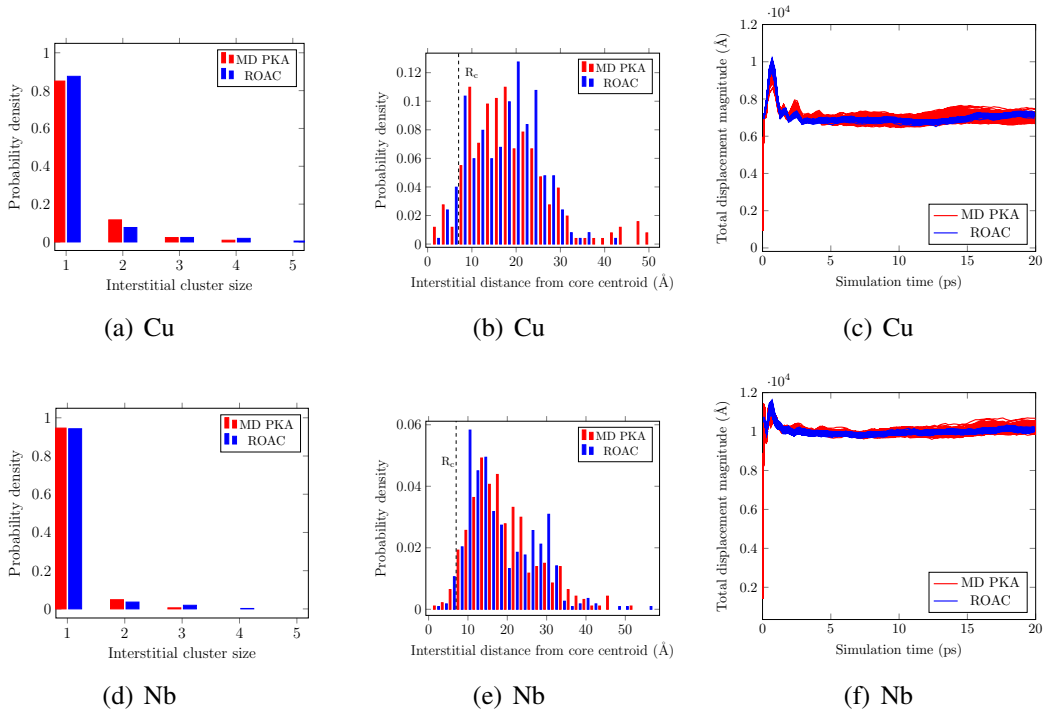

(a) Cu (b) Cu (c) Cu

(d) Nb (e) Nb (f) Nb

Figure 4.3: Comparison of damage characteristics for 1keV recoil in Cu and Nb. (a) and (d): Interstitial cluster size distribution. (b) and (e) Interstitial spatial distribution. Dash-line represents the approximate radii R_c of the spherical thermal generated by the the reduced-order atomistic method. (c) and (f) Total atomic displacement. Overall quantitative mixings are closely matched.

We also examined the defect characteristics of low (1 keV) and high (10 keV) energy

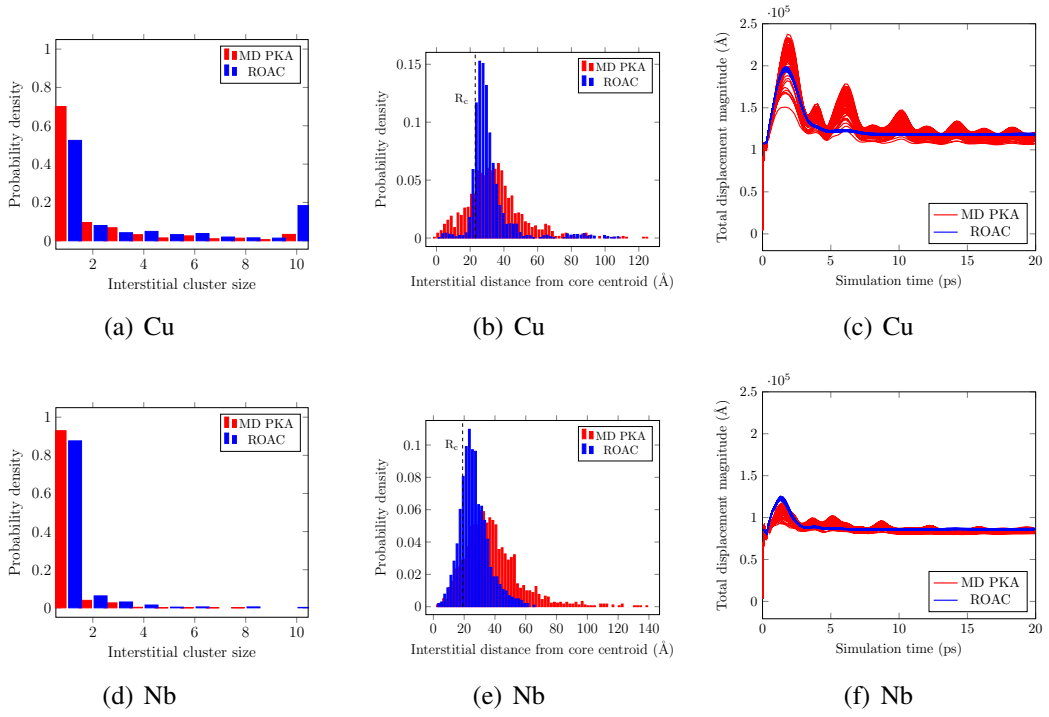

(a) Cu (b) Cu (c) Cu

(d) Nb (e) Nb (f) Nb

Figure 4.4: Comparison of damage characteristics for 10 keV recoil in Cu and Nb. (a), (d) Interstitial cluster size distribution. (b), (e) Interstitial spatial distribution. Dash-line represents the approximate radii R_c of the spherical thermal generated by the the reduced-order atomistic method. (c), (f) Total atomic displacement. Overall quantitative mixings are closely matched.

recoil events produced by the two methods. In Figures 4.3 and 4.4, we present a statistical comparison between the two methods in terms of interstitial cluster size distribution (Figs. 4.3(a),(d) and 4.4(a)(d)), spatial distribution of interstitial defects (Figs. 4.3(b),(e) and 4.4(b)(e)) and time evolution of the atomic displacement histories at the onset of the thermal spike (Figs. 4.3(c),(f) and 4.4(c)(f)) for both Cu and Nb. Results have been averaged over one hundred random cascade simulations for each energy and for each method.

Examining the results comparison for the low recoil energy recoil events (Fig. 4.3) for both Cu and Nb, we note a good agreement between the defect characteristics produced by our methodology and those produced by explicit MD cascade simulations. As expected, both methods produce a majority of isolated point defect (interstitial clusters of size 1), with a few rare small defect cluster appearing throughout. The spatial distribution of interstitial

defects within the cascade are also in good agreement, with the majority of the ballistic defects lying beyond the radius $\mathrm{R_c}$ of the thermal spike. As for the comparison of the atomic mixing, the resultant total atomic displacement histories from the reduced-order atomistic cascade model tend to have less overall variations than those from explicit MD cascade simulation since this methodology approximate cascades with a spherical thermal spike core of similar size for each realization. However, over the 20 ps relaxation period, all displacement histories plateau to similar equilibrium levels, regardless of the modeling method.

For the high energy recoil events (10 keV) in Fig. 4.4, there are noticeable differences in the defect statistics produced by explicit MD cascade simulations and the reduced-order atomistic cascade model. The distribution of sizes of interstitial defects produced by our methodology show a greater population of large interstitial defects with nearly 20% of defect clusters of size ten and up. Whilst these results may not appear to be ideal at first glance, this production of large interstitial clusters is not entirely undesirable. Previous simulations of displacement cascade Fe [61] have demonstrated the creation of large interstitial clusters of as the result of thermal shock transporting atoms out of the thermal spike region. This can be verified by directly examining the larger Cu interstitial cluster as shown in Fig. 4.5(a). For this configuration, the large interstitial cluster lies actually on the periphery of the designated thermal spike core. Balancing the shift in local atomic densities, the formation of large interstitial cluster(s) is accompanied by a clustering of vacancy defects near the initial thermal spike center. We show in Fig. 4.5(b), the resultant Stacking-Fault Tetrahedron (SFT) surrounding the low density vacancy cluster. SFTs are characteristic defects frequently seen in irradiated FCC metals, especially for the case of Cu [29, 121]. The increased SFT production is also clearly reflected in the normalized vacancy cluster size distribution shown in Fig. 4.5(c), where a large population of large vacancy clusters can be seen.

Fundamentally, what differentiates the defect cluster productions between the two meth-

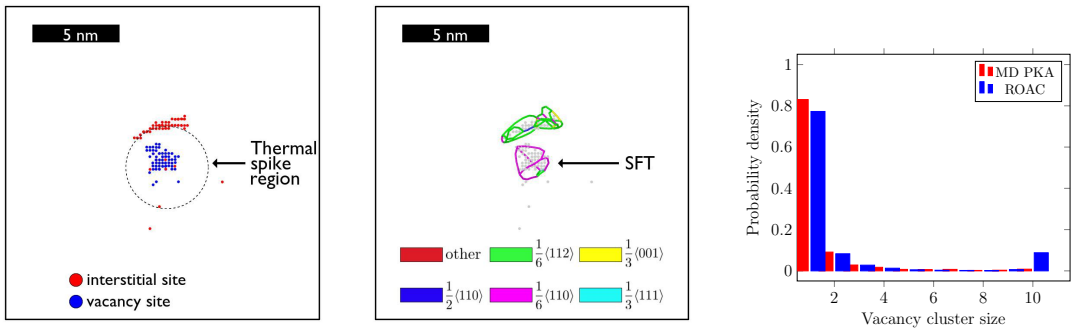

(a) Wigner-Seitz analysis (b) Dislocation analysis (c) 10 keV recoil in Cu

Figure 4.5: Large interstitial clusters generated by the reduced-order atomistic model for a 10 keV recoil. (a) Wigner-Seitz point defect analysis. Large interstitial cluster appears on the periphery of the thermal spike region; vacancy defects cluster towards the center of the sphere. (b) Dislocation eXtraction Analysis (DXA). Stacking-Fault Tetrahedron (SFT) surrounds the low density vacancy defect cluster. (c) Vacancy cluster distribution for 10 keV recoils in Cu. Large vacancy clusters correspond to the formation of SFTs.

ods is the structure of the thermal spike core. Under the idealized assumption of the reduced-order atomistic cascade method, a thermal spike is always reproduced in its most condensed spherical form. By contrast, a displacement cascade is much more stochastic in nature, which tends to form oblong or elliptical thermal spike regions along its primary trajectory. While the volume of both thermal spike core structures can be directly match by N_{rpa}, the non-spherical thermal spike structure will always have a large surface area to dissipate the same initial recoil energy T_{d}. Indeed, the amplification of the thermal shocks over the minimal spherical surface area is the driving force of the large interstitial cluster productions by the reduced-order atomistic cascade method. This difference in thermal spike core structure can be seen in the distributions for the interstitial distance from the core in Fig. 4.4(b) and 4.4(e). The interstitial distributions produced by the reduced-order atomistic cascade model simulations are clearly concentrated near the periphery of the spherical thermal spike region, with an approximate radius of $\sim$ 23 Å for Cu and $\sim$ 19 Å for Nb. Conversely, the interstitial distributions produced by explicit MD cascade simulations span more evenly and wider spatial range, representing a more dispersed defect production pro-

cess. For recoil energies larger than 10 keV, this difference in defect cluster production is further accentuated, leading to the large deviations of N_{dpa} shown in Fig. 4.2. However, at such high energies, it becomes increasingly unrealistic to assume a single contiguous thermal spike core. Instead, better damage reproductions can be made by simply dividing up the high energy recoils akin to the process of cascade fragmentation (see Sec. 4.4.1).

4.4 Applications

4.4.1 Cascade fragmentation

As discussed in the previous section, cascade fragmentation is not only important for the redistribution of recoil energies, it also affects the very nature of defect production generated from our methodology. Here, we showcase a simple and straightforward fragmentation implementation by directly replicating a high energy displacement cascade with our reduced-order atomistic cascade model.

The basis for replicating a fragmented cascade with our methodology is to approximate a fragmented cascade with multiple smaller recoil events with the total energy roughly equivalent to the initial PKA recoil energy T. For example, we show in Fig. 4.6 the manual breakdown of a 100 keV displacement cascade, and subsequent reconstruction with spherical core-shell cascades. In order to minimize the amount of the energy lost to thermal dampening, we consider the displaced cascade configuration from the explicit MD cascade simulation (Fig. 4.6(a)) relatively early at 0.16 ps after PKA initiation. Atoms with total energy gain $\Delta E_{\mathrm{total}} = \Delta E_{\mathrm{cohesive}} + \Delta E_{\mathrm{kinetic}} < 0.5$ eV are assumed to be undisturbed by collisions and ignored, and the remaining atoms are spatially divided into smaller fragments with energy of $E_{\mathrm{frag}} = \sum_i^n \Delta E_{i,\mathrm{total}}$. Note that the initiating PKA atom is ignored due to the its net energy loss from the collisions. Due to a combination of the energy loss to electronic stopping and the 0.5 eV energy screening, the sum of E_{frag} in this example only yields $\sim$90.1 keV of the 100 keV initial T. To match the exact fragmentation pattern of the displacement cascade shown in Fig. 4.6(a), we calculated the center-of-mass was for each

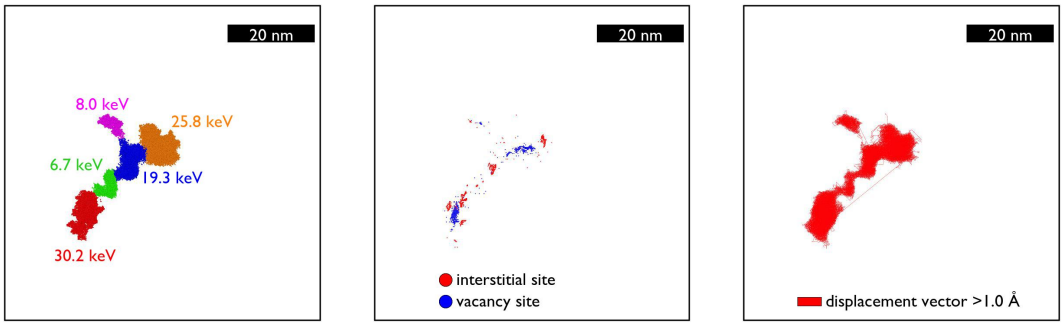

(a) MD PKA - Fragments (b) MD PKA - Defects (c) MD PKA - Displacements

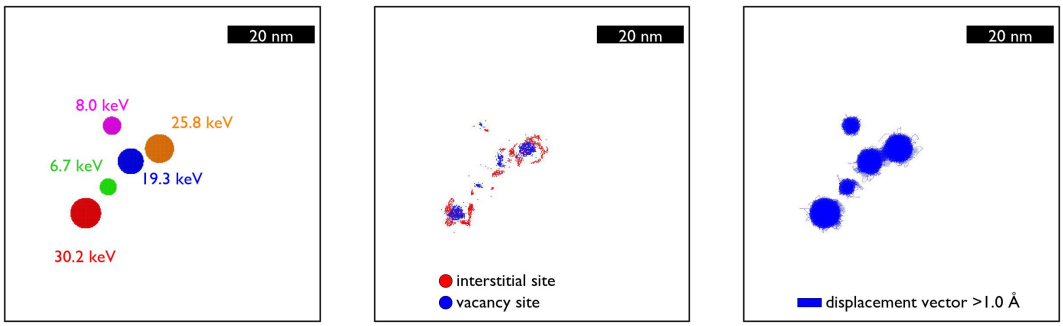

(d) ROAC - Fragments (e) ROAC - Defects (f) RAOC - Displacements

Figure 4.6: Fragmentation and replication of a 100 keV recoil event in Cu produced by explicit MD PKA cascade simulations and produced by the reduced-order atomistic cascade model. (a), (d) Energetic division of recoil event into fragments. Displacement cascade is rendered at 0.16 ps after PKA initiation; arc-DI is rendered at initialization. Total fragment energy is ∼90 keV. (b), (e) Final defect damages as represented by dislocations. (f), (g) Final mixing damages as represented by displacement vectors. Atoms with displacement magnitudes less than 1 Å are ignored.

of the cascade fragments. In 4.6(d), all five cascade fragments are reconstructed with our methodology, using the extracted position and energy data. Both simulation sets (explicit MD cascade simulation and reduced-order atomistic cascade method) were relaxed over 20 ps, quenched and then minimized before the final damage comparison.

As shown in the comparison of the final stable defect contents between Fig. 4.6(b) and Fig. 4.6(e), while the spatial distributions of the dislocations remain in agreement, the dislocation content produced by our reduced-order cascade model is noticeably higher as compared to those produced by explicit MD cascade simulations, especially for the larger

subscade fragments with energies of 25,778 eV and 30,265 eV. This is to be expected since the modified NRT-dpa model, and therefore our model, favors the production of large defect clusters at high T, due to the assumption of a spherical thermal spike. If the discretization and breakdown of the full cascade were to be performed with smaller fragments, we would expect that the final defect content could be brought more faithful to that of the actual displacement cascade. In Figures 4.6(c) and 4.6(f), we illustrate the overall mixing histories and final atomic displacements greater than 1 Å. While total atomic displacements appear approximately equal, the compact spherical thermal spike cores produced by our methodology were not able to fully merge into the contiguous structure as predicted by the actual displacement cascade predicted by explicit MD cascade simulations. Overall, both the defect and mixing damages of the 100 keV cascade can be replicated with the multi-fragment reduced-order cascade model. The accuracy and spatial distribution of defect production are, however, somewhat dependent on the fragment/energy discretization and does require a more established numerical model. While there have been many studies attempting to capture the governing principles of fragmentation [105, 122, 123, 124, 125], there is yet to be a generally accepted predictive numerical model. Critical values such as fragmentation energy can widely vary depending on the fragmentation breakup criteria [122]. The damage-oriented defect cluster scaling laws [107, 126] require significant data generation and fitting for different materials, which lie far beyond the scope of the current study.

4.4.2 High dose ion-bombardment

One of the main benefit of the present reduced-order atomistic cascade model is the ability to efficiently simulate dose effects. Since thermal shocks terminate quickly near the thermal spike core, multiple isolated recoil events can be simulated simultaneously, provided that the thermal spike regions do not overlap. This is functionally similar to the one illustrated in the previous section for the multi-fragment/subcascade model, but expanded to a higher rate of damage insertion, over multiple relaxation intervals. Depending on the

size of the simulation cell and the energy of the recoil events, modeling large dose accumulation with the reduced-order atomistic cascade method can be three to four orders of magnitude faster than performing sequential explicit MD cascade simulations but necessitates more approximations. Here, we further illustrate the capabilities of this methodology by simulating realistic ion-bombardment for 1 MeV protons and 1 MeV Cu ions into Cu.

From the simulation perspective, the main differentiating factor between the two irradiation sources is the density of recoils as a function of recoil energy (also known as the primary recoil spectrum). Here, we use the simple integral primary recoil spectrum [127] produced by the first initial collision and is given as,

$$P(E,T) = \frac{\int_{E_\mathrm{d}}^{T} \sigma(E,T')dT'}{\int_{E_\mathrm{d}}^{\hat{T}} \sigma(E,T')dT'}, \tag{4.4}$$

where E is the incident ion energy, $\hat{T}$ is the maximum recoil energy, and $\sigma(E,T')$ is the differential energy transfer cross section with a recoil energy of T'. For example, we show in Fig. 4.7(a) the fraction of recoils for 1MeV proton and 1MeV Cu ion projectiles into Cu. We calculated $\sigma(E,T')$ for the proton source using a Coulomb potential corresponding to Rutherford scattering [12]; and $\sigma(E,T')$ for the copper ion source was calculated using the fitted inverse square potential corresponding to slow heavy ions [12]. Note that, while there are $\sim$ 2.5% of the recoil spectrum from Cu ion irradiation exists for $T > 50$ keV, these rare cases were ignored during energy sampling due to fragmentation concerns raised in the previous section.

For each source, we inserted 500 recoil events sampled from Eq. 4.4 every 20 ps. The computational domain is comprised of 4,000,000 atoms. In Figures 4.7(b) and 4.7(c), we illustrate the first 500 approximated cascades inserted. As expected, the higher energy recoil spectrum of the Cu ion source produces more damages on a per event/interval basis.

In order to compare the effects of the different irradiation sources, it is important to

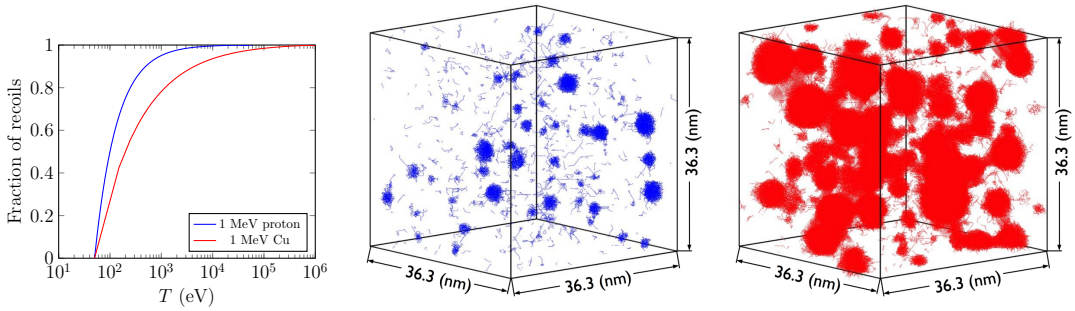

(a) Integral Primary Recoil Spectrum

(b) 1 MeV proton source

(c) 1 MeV Cu ion source

Figure 4.7: Integral primary recoil spectra and applications in ion-bombardment . (a) Integral primary recoil spectrum of 1 MeV ion sources irradiating Cu. (b) Atomic displacement damage after 500 proton recoil events. (c) Atomic displacement damage after 500 Cu ion recoil events. Displacement vectors of magnitude less than 1 Åare not rendered. Periodic boundary condition is applied in all three dimensions.

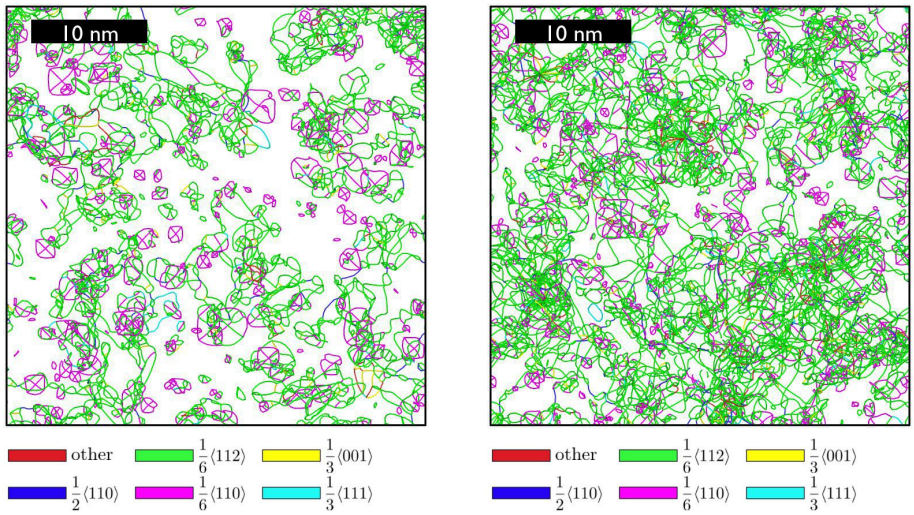

(a) 1 MeV proton source

(b) 1 MeV Cu ion source

Figure 4.8: Radiation defect accumulated at ∼0.0279 dpa. (a) Dislocation defects produced by 1 MeV proton source. Total dislocation density is $1.054 \times 10^{17}\mathrm{m}^{-2}$. (b) Dislocation defects produced by 1 MeV Cu ion source. Total dislocation density is $1.923 \times 10^{17}\mathrm{m}^{-2}$. Dislocation are color-coded by type.

classify the defect states not by the number of recoil events, but by the actual damage produced, i.e., displacement-per-atom. For consistency with experiments and other models,

here we calculate the accumulated damage using the standard NRT-dpa model instead of the modified arc-dpa formalism. With our simulation setup, after ∼6144 core-hour (256 cores × 24 hours), simulations for proton and Cu ion irradiations reached ∼0.0286 dpa (39,000 events) and ∼0.120 dpa (37,500 events) respectively. While the comparative dose rate of the proton source is much smaller due to the lower energies, it could be increased by adjusting the number of events inserted at each interval. In 4.8, we show the resulting defect structures at ∼0.0279 dpa for both irradiation sources. Even at this very early stage of damage accumulation [115], the effects of irradiation source and recoil energy on microstructure evolution are apparent. It is interesting to note that the type (SFTs and $1/6\langle 112\rangle$) and density of defects at this damage level is comparable to those observed experimentally [128, 129].

4.5 Discussion & Conclusions

As illustrated in the previous two sections, the present reduced-order atomistic cascade model for simulating radiation effects in bulk metals proves to circumvent the simulation size scaling and adaptive time stepping challenges raised in the introduction. In that respect, it is conceptually similar to the FPA method where Frenkel pairs are periodically added to the simulation or classical BCA methods where defect production is added after each collision and removed when the energy of moving atoms becomes too small. The present methodology, however, approximates cascades by not only replicating displacement damage (arc-dpa) but also the atomic mixing (rpa) from the thermal spike incurred during the ballistic phase.

However, as illustrated in the previous section, prediction of subcascade formation remains elusive. Additionally, based on the imposed atomistic timescale associated with the cascade insertion when simulating defect accumulation and dose effects, the simulated dose rates are accelerated far beyond what can be replicated experimentally. Consequently, the present methodology will not be able to capture some of the mechanisms (e.g., diffusion

of point defects and small clusters) occurring at larger time scales. The inability for the atomistic timescale to accurately reach characteristic times associated with diffusion processes does restrict the interaction and clustering of point defects and small clusters at low dose/damage levels. Fortunately, these small defects quickly grow in size, and become immobile upon further irradiation, reducing the concern of diffusion over time. As a result, the dose and interfacial effects on defect evolution should remain largely unaffected by the dose rate, except the very early stages of point defect accumulation. Finally, this methodology is for now limited to simulating displacement cascades embedded in the bulk of a crystalline material. Calibration and modification of the damage estimators would need to be revisited in order to simulate the interaction of cascade with free surface to account for sputtering or surface effects for example.

We have presented an atomistic method to model displacement cascades or implantation in crystalline materials across a wide range of recoil energy. This reduced-order atomistic cascade method is based on modeling the cascade as a core-shell atomic structure composed of two damage production estimators. These estimators account for athermal recombination corrected displacements per atom and atomic mixing. They are calibrated from explicit PKA simulations and a standard displacement damage model. The comparison of the defect production and defect characteristics produced by this model and by explicit MD cascade simulations are close across the large range of recoil energy tested. For high energy recoil events, we have demonstrated how this methodology can be used to approximate cascade fragmentation by superimposing subcascades with smaller energy approximated cascades that match the final spatial distribution of defects. Due to its computational efficiency, we also demonstrated how this reduced-order method can be used to model dose effects beyond what can be practically achieved with standard MD cascade simulations by illustrating damage accumulation due to ion bombardment in the case of 1 MeV proton and Cu irradiation into Cu.

Whilst larger defect clusters may appear relative static in the atomistic timescale, stress/temperature

driven cluster diffusions/migrations are expected over a period of seconds or hours. In order to obtain more holistic view of radiation defect accumulation and evolution over engineering/experimental timescale, its important to incorporate these mechanisms typically inaccessible to MD models. By replacing the source term with an atomistically accurate defect production, results obtained from this methodology can easily be upscaled to rate theory models [130] for example to develop versatile multiscale radiation effects models.

CHAPTER 5

MISFIT DISLOCATION NETWORKS IN SEMI-COHERENT MISCIBLE PHASE BOUNDARIES: AN EXAMPLE FOR U–ZR INTERFACES [131]

Before we can answer **Q2: How do phase boundaries affect radiation defect accumulation, and how does the interfacial microstructure evolve?**, we must have a firm grasp of the phase boundary characteristics before irradiation. To this end, this chapter examines one of the most basic forms of semi-coherent cube-on-cube miscible phase boundaries between U and Zr. The misfit accommodation at these phase boundaries is commonly characterized by a two-dimensional dislocation network on the interfacial plane. While classical lattice theory can provide predictions for the interfacial microstructure, significant departures can be seen in simulation results. This is ultimately attributed to the competition between the structural accommodation (lattice mismatch) and the chemical accommodation (composition mismatch), which is uniquely applicable to phase boundaries. Unfortunately, as we will later see in Chapters 6 and 7, most interfacial microstructures have minimal effect on the process or radiation defect accumulation and none are likely to survive over large doses.

5.1 Introduction

The structure and properties of heterophase boundaries (also referred to as phase boundaries) are important microstructural factors controlling the formation, morphology and stability of multiphase metallic alloys [132, 133]. The nature of such interfaces in terms of coherency (coherent, semi-coherent or incoherent) is classically characterized by the lattice mismatch between both phases $\epsilon^{m,S} = 2\frac{\ell_\alpha - \ell_\beta}{\ell_\alpha + \ell_\beta}$ (ℓ_α and ℓ_β representing the lattice constants of each phase α and β), resulting in the formation of interfacial defects such as dislocation networks [134]. The state of interfacial coherency depends not only on the physical and the

chemical nature between both phases, but also on external factors such as the temperature or the stress field. For a coherent phase boundary, the mismatch is completely accommodated by straining both phases. In the case of a semi-coherent phase boundary, localized misfit dislocation networks are responsible for compensating uniform far-field elastic fields, while an incoherent phase boundary is the result of two rigid semi-infinite media in rigid contact [134, 135]. In the general case where one phase precipitates from the other and the two host metallic elements are (at least partially) mutually miscible, it is unlikely that the phase boundaries will be incoherent. If the interface is coherent, thermodynamic properties of the individual phases generally draws more interest than the interface and are well studied by researchers [136, 137]. Additionally, incoherent and semi-coherent boundaries between immiscible metals have attracted significant attention owing to the development of engineered multilayered materials [138, 139, 140, 141] for improved strength, toughness and radiation resistance.

From a theoretical standpoint, the characterization of the structure of interfaces in terms of dislocation network and the nature of those dislocations is commonly performed through the analysis of the geometrical compatibility and/or the elastic distortion near the interface. Thus, the Frank-Bilby formalism [142, 143, 144] is a widely used approach to determine the intrinsic dislocation content of a general boundary. Extensions of this classical formalism have been proposed to account for anisotropic elasticity or the elastic relaxations from the in-plane dislocation configurations [145, 146]. Alternatively, interphase boundaries have also been extensively examined through the use of atomistic simulations. The objectives of such computational studies differ from theoretical ones, as they center not only one the interfacial defect structures [139, 147], but also on additional thermodynamic and kinetic properties of the interface [148, 141, 138]. Analysis techniques such as disregistry [144, 147] or the Dislocation Extraction Algorithm (DXA) [100, 149, 150, 151] are now frequently used to analyze and quantify interfacial dislocation networks. The materials systems studied are commonly interfaces between immiscible metal solids such as

Cu–Nb [141, 139] or Ag–Ni [152, 132] for example.

In comparison, incoherent and semi-coherent phase boundaries between miscible materials are more commonly encountered in structural materials but less studied. Buried in the bulk, such interfaces are not easily amenable to surface characterization probes. Thermodynamic, kinetic and physical properties of the individual phases themselves warrant and attract significant attention. However, these types of phase boundaries between two miscible phases play an important role in determining key properties such as interphase decohesion, crack propagation, or interfacial solute segregation. An illustration of such interfaces can be found in U–Zr binary alloys which exhibit a tendency to phase separate into U-rich and Zr-rich precipitates. Depending on alloy compositions as well as heat treating/cooling conditions, complex interfacial features such as lamellar, acicular and Widmanstätten microstructures can be observed [38, 153, 154]. Both U and Zr have non cubic native structures at room temperature (orthorhombic and hexagonal) and transform to the cubic bcc structure at higher temperatures. Within this temperature regime, the two metals form a bcc solid solution which upon cooling leads to a high temperature miscibility gap in which both bcc phases (γ-U and β-Zr co-exist). With lattice constants $\ell_{\mathrm{U}} = 3,442$ Å and $\ell_{\mathrm{Zr}} = 3.553$ Å, the natural lattice mismatch $\epsilon_{U/Zr} = 0.0317$. It is expected that the U–Zr interface will be semi-coherent with the lattice mismatch being accommodated by misfit dislocations. Investigation into this alloy system has focused primarily on the structure and properties of the bulk phases as a function of the alloy composition and, more recently, on thermodynamic driving forces affecting phase formation [91, 155]. Interphase boundaries in U–Zr alloys however have received little to no attention so far. Neither U nor Zr lend themselves easily to atomistic study or experimental observation and the alloy system described above presents a rich variety of interfacial configurations. Before venturing into studying boundaries between the complex crystal structures, we can investigate an extreme bound of these phase boundaries, namely cube-on-cube U–Zr interface boundaries. Such a set of boundaries may exist in the miscibility gap (albeit with some mutual solubility) and

is also precursors of the phase separation into the intermetallic δ and the orthorhombic α phases.

In what follows, the non-uniform dislocation structure of miscible semi-coherent bcc/bcc U–Zr interfaces is systematically characterized using atomistic simulations. Misfit dislocation networks and their characters are investigated as a function of various interfacial misfit strains and surface orientations. Section 5.2 describes details of the atomistic simulation and methods used to characterize the interface dislocation structure. Section 5.3 provides a description of the misfit dislocation patterning characteristics for the various stacking orientations and misfit strains explored. Section 5.4, concludes this study with a discussion of the miscible interface properties, with a particular emphasis on the respective contributions from the dislocation-dislocation elastic interactions on one hand and chemical interactions due to the miscibility between U and Zr on the other hand.

5.2 Methodology

5.2.1 Atomistic modeling of semi-coherent U–Zr interfaces

The atomistic simulation code LAMMPS (Large-scale Atomic/Molecular Massively Parallel Simulator [93]) is used to generate and configure the relaxed atomistic configurations of semi-coherent U–Zr phase boundaries. In this work, the Modified Embedded Atom Method (MEAM) interatomic potential developed by Moore et al. [91] for U–Zr alloys is employed to describe interatomic interactions in the vicinity of U–Zr interfaces. This interatomic potential has been developed for simulating γ-U–Zr alloy phase, and considers the anisotropic bonding at the rigid bi-crystalline interfaces. As the basis for this study, the optimized, relaxed structures of pure bcc U and pure bcc Zr are first obtained using bulk molecular static simulations. The resulting lattice constants and per-atom bulk energy are calculated to be $\ell_{\mathrm{U}} = 3.442$ Å, $E_U^{\mathrm{bulk}} = -5.287$ eV and $\ell_{\mathrm{Zr}} = 3.535$ Å, $E_{Zr}^{\mathrm{bulk}} = -6.2$ eV respectively. These properties are fairly consistent with other first principle simulation results, and closely matches experiment data with $\ell_{\mathrm{U}}^{\mathrm{exp}} = 3.198$ Å [156] and $\ell_{\mathrm{Zr}}^{\mathrm{exp}} = 3.574$

Å [157]. As evident by the proximity of the lattice constants ℓ_{U} and ℓ_{Zr}, the two pure bcc phases share highly similar structures. Such similarity in lattice constants eliminates most incoherent interfaces, which are highly disordered interfaces and thermodynamically unfavorable. The two remaining types are the coherent interface and the semi-coherent interface. The former results from distributed intra-phase strains, creating perfect lattice match; the latter accommodates the lattice mismatches in forms of periodic localized dislocations. Comparably, the dislocation features affect the interfacial characteristics far more prominently, hence the main focus of the study is on the semi-coherent interfaces.

Various stacking orientations are considered within the atomistic simulations based on the most energetically favorable cube-on-cube interfaces between U and Zr, namely only the $\{001\}$, $\{110\}$, $\{111\}$ and $\{112\}$ boundary planes. For each of these orientations, various interfacial structural mismatches are considered by varying the overlap between the surface lattice vectors of each phase during the matching process between both materials. Within the atomistic model, the structural mismatch $\epsilon^{m,S}$ is classically defined as $\epsilon^{m,S} = 2\frac{m\ell_U - n\ell_{Zr}}{m\ell_U + n\ell_{Zr}}$ [135, 158], where (m, n) are scaling factors (integers) corresponding to lattice multiplicities of their respective ensemble. Considering the lattice size difference between U and Zr, the scaling factors are chosen such that $m > n$, with the extra lattices residing exclusively in the smaller U lattice. A 5% mismatch upper limit was also imposed on the scaling factor selection to improve the natural viability of the interfaces. The mismatched ensemble lattice selected for simulations range from 2.4% (m=20, n=19) to 5.3% (m=13, n=12) depending on the combination of the scaling factors (m, n).

Simulation setups are typical of semi-rigid bi-crystalline contact interfaces. To accommodate the lattice misfit and achieve commensurability in the contact planes, one lattice is isotropically stretched/deformed by $\epsilon^{m,S}$ to match dimensions of the adjoining other lattice. Deformations in this study were imposed on the Zr supercells due their lower scaling factor n, where edge dislocations would be absent. Periodic boundary conditions are applied to the simulation cell in all directions, matching the periodic nature of the semi-coherent

interface structures. The periodic boundary condition also generates a secondary stacking interface in the transverse direction. To minimize any interface-interface interactions, each initial ensemble is constructed with a minimum height of ≈ 100 Å.

To generate variations in the initial interfacial structures, the Γ-surface technique [159, 141] is adopted. Stacking variations are created by incremental displacements of one superlattice relative to the other in the interfacial plane. The process is typically arduous due to the small displacement increments (1Å) need to cover the superlattice surface. Fortunately for systems of misfit interface, due to the repeating nature of both superlattices, the number of unique stacking variations is greatly reduced. Accordingly, the displacement shifts were conducted over a 5×5 grid across a single lattice surface with increments between 0.7 Å and 1.2 Å, generating 25 structural variants per orientation.

Following the construction of each interface, molecular statics simulations are performed to generate the energy-optimized interfacial structures. An isobaric-isothermal (NPT) ensemble with a zero pressure constraint is applied to system to allow strain redistribution and dislocation formation. Energy minimization was conducted over maximum $200,000$ iterations using the Conjugate Gradient (CG) algorithm; energy and force convergence are set to 10^{-15}.

5.2.2 Characterization of interface dislocation structure

The characterization of networks of misfit dislocations is accomplished using an atomistic computational algorithm that identifies all interfacial dislocations and their associated Burgers vectors [100, 149]. This analysis is complemented by a disregistry analysis on the atomistic system and the Frank-Bilby (FB) formalism in order to verify and quantify the spacing and nature of the dislocation networks.

Dislocation extraction algorithm

With the similarity in nature between defects on misfit interfaces and those in bulk lat-

tices, the Dislocation Extraction Algorithm (DXA) [100, 149] is employed to extract the interfacial dislocation network structure. The underlying concept for this algorithm relies on the construction of the Burgers circuit [143]. The approach extracts the dislocation Burger's vector segments through the automated calculation of the incompatible elastic displacement field surrounding dislocations combined with the Common Neighbor Analysis (CNA) atomic structure identification algorithm.

Disregistry analysis

In order to verify the dislocation structures at the interface and to further quantify the spacing and characteristics of the dislocation networks, the displacement disregistry [144] is measured across the U–Zr interface plane after relaxation. The disregistry $\Delta\mathbf{r}$ is defined as the relative displacement of atoms between the un-relaxed natural dichromatic pattern (NDP) configuration [139] and the relaxed real interface configuration (Relx). The NDP configuration is constructed by compressing and stretching the initial simulation configuration (also called coherent dichromatic pattern (CDP) configuration [139]) to the dimensions of the relaxed real interface configuration. Note that the NDP configuration therefore corresponds to the relaxed dimensions in absence of misfit dislocations. Within this context, the disregistry between the Relx configuration and the NDP configuration is calculated as difference in relative positions between i^{th} and j^{th} atoms such that

$$\Delta\mathbf{r} = \mathbf{r}_{ij}^{\text{Relx}} - \mathbf{r}_{ij}^{\text{NDP}}. \tag{5.1}$$

In other words, $\Delta\mathbf{r}$ corresponds to the non-uniform relaxation displacement field due to the formation and presence of misfit dislocations. Furthermore, the disregistry $\Delta\mathbf{r}$ is decomposed into an edge and a screw component, $\mathbf{b}_e$ and $\mathbf{b}_s$ respectively. The edge component $\mathbf{b}_e$ is defined as the component normal to the dislocation line such that $\mathbf{b}_e = \Delta\mathbf{r} \cdot \hat{\mathbf{n}}$; while the screw component $\mathbf{b}_s$ is defined as the component along the dislocation line $\mathbf{b}_s = \Delta\mathbf{r} \cdot \hat{\boldsymbol{\xi}}$.

$\hat{\mathbf{n}}$ and $\hat{\boldsymbol{\xi}}$ are unit vectors normal and parallel to the dislocation line.

Quantized Frank-Bilby formalism

Finally, further verification and identification of the dislocation line and average spacing of interfacial misfit dislocations are conducted by solving the quantized Frank-Bilby (qFB) formulation [160, 139, 161]. These theoretical predictions are compared against the simulated dislocation networks at the interface. The qFB formalism relates the net Burgers vector content $\mathbf{B}(\mathbf{p})$ to N sets of discrete dislocations lying in the interfacial plane. Derived from Bollmann's O-lattice theory [162], $\mathbf{B}(\mathbf{p})$ can be expressed with respect to a reference lattice as the intersection of the coincident O-lattice with the interfacial plane such that,

$$\mathbf{B}(\mathbf{p}) = \sum_{i=1}^{N} (\frac{\mathbf{n} \times \boldsymbol{\xi}_i}{d_i} \cdot \mathbf{p}) \mathbf{b}_i, \tag{5.2}$$

where $\mathbf{n}$ is interface normal, $\boldsymbol{\xi}_i$ is dislocation direction, d_i is dislocation spacing, $\mathbf{p}$ is a probe vector in the interface plane, and $\mathbf{b}_i$ is the Burgers vector of the interface dislocation. Conveniently, for the bcc-bcc stacking orientations under consideration, the coincident O-lattice is also a bcc structure. This provides two sets readily available, conventional and primitive, translation vectors to be used as starting $\mathbf{b}_i$ for the qFB formulation. For the conventional translation vectors, $\mathbf{b}_i$ is chosen as the set of $[100]$, $[010]$ and $[001]$ vectors. For the primitive translation vectors, $\mathbf{b}_i$ is chosen as the set of $\frac{1}{2}[11\bar{1}]$, $\frac{1}{2}[\bar{1}11]$ and $\frac{1}{2}[1\bar{1}1]$ vectors. Two different sets of dislocation lines are calculated using the qFB formalism, and the resulting dislocation line direction $\boldsymbol{\xi}_i$ and average spacing d_i are then used to construct the predictive interfacial dislocation network structure.

5.3 Results

Due to their correlation to the mechanical performance, three particular interphase boundary characteristics are analyzed and compared in order to describe the misfit dislocation

structures of U–Zr interface for the four selected interface orientations:

1. **Interfacial misfit dislocation structure** corresponds to the intrinsic defects composition on a misfit interface. The presence and extension of different misfit dislocations can be beneficial or detrimental to material plasticity modes.

2. **Interfacial excess energy** serves as a general indicators of interphase boundary occurrence and stability. Low energy interfaces are more thermodynamically favorable; high energy interfaces are more prone to fracture.

3. **Residual elastic fields**, induced by the misfit dislocation network, can be used to identify stress concentration sites and preferred dislocation emission pathways.

The combination of these characteristics can provide further quantitative and qualitative contexts for the expected mechanical behavior for each respective phase boundary stacking orientation.

5.3.1 Interfacial misfit dislocation structure

The stacking misfit of U–Zr superlattices are accommodated in the plane of the interface by the formation of dislocations. The presence of multiple dislocation sets on the same interface generates a unique dislocation network structure for each stacking orientation. Utilizing the DXA method described in Section 5.2.2, dislocation structures are extracted for all interface configurations. Figure 5.1 illustrates the interfacial dislocation network structures for the $\{001\}$, $\{100\}$, $\{111\}$ and $\{112\}$ stacking orientations.

For interfacial dislocation verifications, disregistry analyses are also performed for each stacking orientation based on the initial DXA dislocation lines. For the purpose of identifying discrete dislocations in complex networks, we focused on primarily on disregistry $\Delta\mathbf{r}_{ij}^{Rlx-unRlx}$, representing the relative particle displacement due to the dislocation presence. The full uranium disregistry fields are shown in Figs. 5.2–5.4 for all stacking orientations, along with the DXA predicted dislocation sets. The zirconium disregistry fields

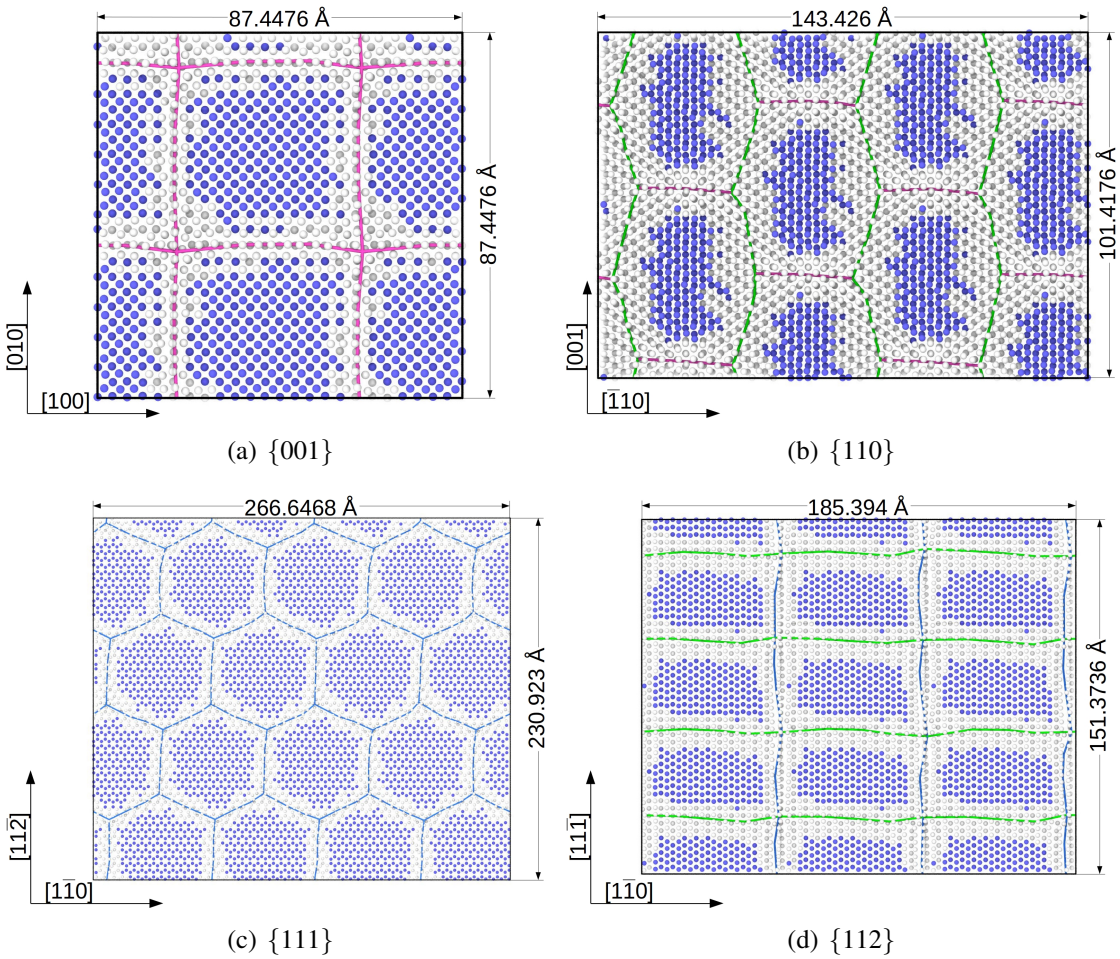

(a) $\{001\}$ (b) $\{110\}$

(c) $\{111\}$ (d) $\{112\}$

Figure 5.1: Interface structures for (a) $\{001\}$, (b) $\{100\}$, (c) $\{111\}$ and (d) $\{112\}$ U–Zr interfaces. Uranium atom layer adjacent to interface is shown with atoms colorized according to their respective lattice structures: blue–bcc, white–disordered. Lines indicate the positions of dislocations. Line colors indicate the types of dislocation: magenta–$\langle 100 \rangle$, blue–$\langle 110 \rangle$, green–$\frac{1}{2}\langle 111 \rangle$

are omitted due to the almost uniform lattice deformation and the lack of dislocation presence. Examining the edge components $\mathbf{b}_e$, dislocation cores and lines can be identified by determining sharp shifts (from positive to negative) in the relative displacement direction. Using the simulated dislocation orientations as initial estimates, disregistery analyses are conducted to pinpoint matching dislocation positions to within a few angstrom. For $\{001\}$ and $\{111\}$ stacking orientations, where multiple symmetrically identical dislocation sets exist, disregistry analyses are reduced down to the single set necessary to confirm the relative positions of dislocations in the disregistry field.

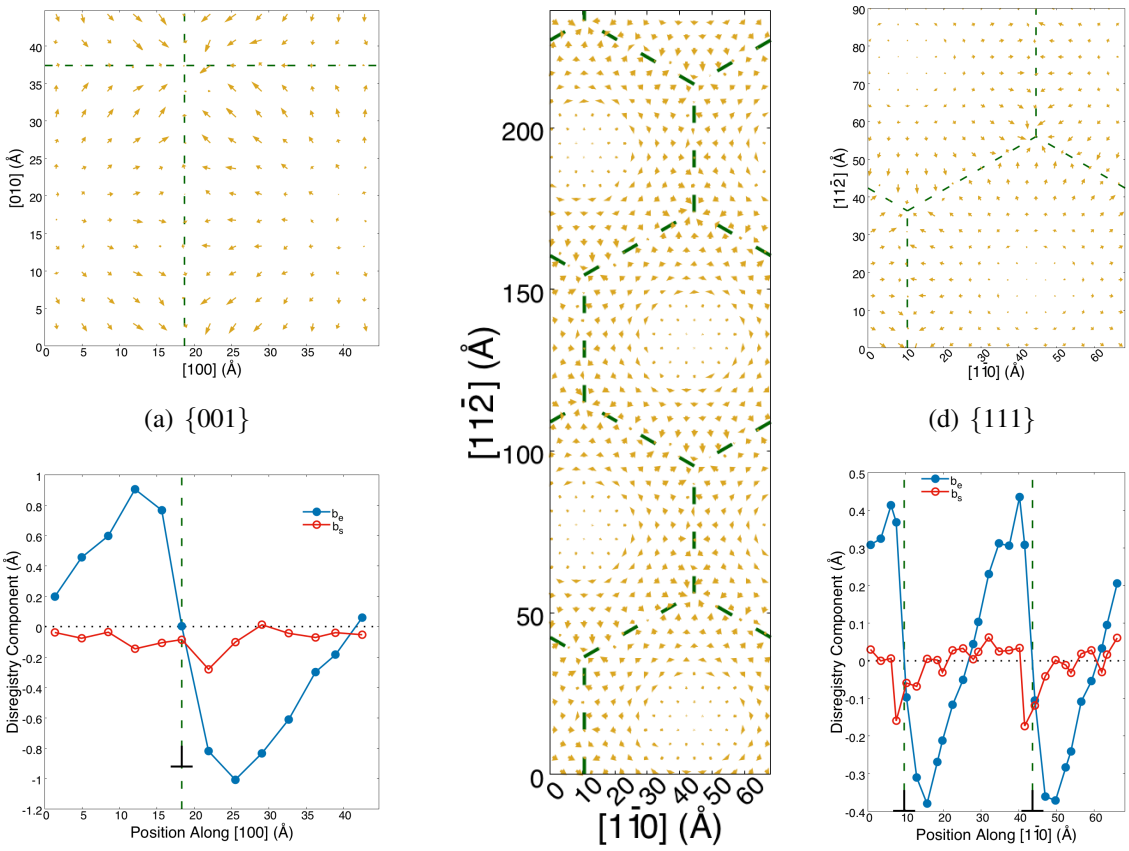

(a) $\{001\}$ (b) $\{001\}$ (c) $\{111\}$ (d) $\{111\}$ (e) $\{111\}$

Figure 5.2: Disregistry analysis for $\{001\}$ and $\{111\}$ U–Zr interfaces. $\{001\}$ U–Zr interface: (a) Full displacement disregistry field; (b) Disregistry components, assumed dislocation line in the $[010]$ direction and $\hat{n}$ in the $[100]$ direction. A single disregistry component set is shown, since dislocation line in $[100]$ is symmetrically identical to that in $[010]$. $\{111\}$ U–Zr interface: (c) Full displacement disregistry field; (d) Partial displacement disregistry field; (e) Disregistry components, assumed dislocation line in the $[11\bar{2}]$ direction and $\hat{n}$ in the $[1\bar{1}0]$ direction. A single disregistry component set is shown, since dislocation lines in $[1\bar{2}1]$ and $[\bar{2}11]$ are symmetrically identical to those in $[11\bar{2}]$.

Disregistry analyses were able to confirm the dislocation defect sites extracted by DXA to high degrees of accuracy. The single exception remains in the case of the $\{110\}$ stacking orientation, where the dislocation sets along the $[001]$ direction do not align with the disregistry convergence (dislocation) cores. Uniform planar displacements of the interfacial particle layers can also cause overall change in edge components. These, however, are easily identified during disregistry analyses and rectified by adjusting the edge component zero (from positive to negative) offsets.

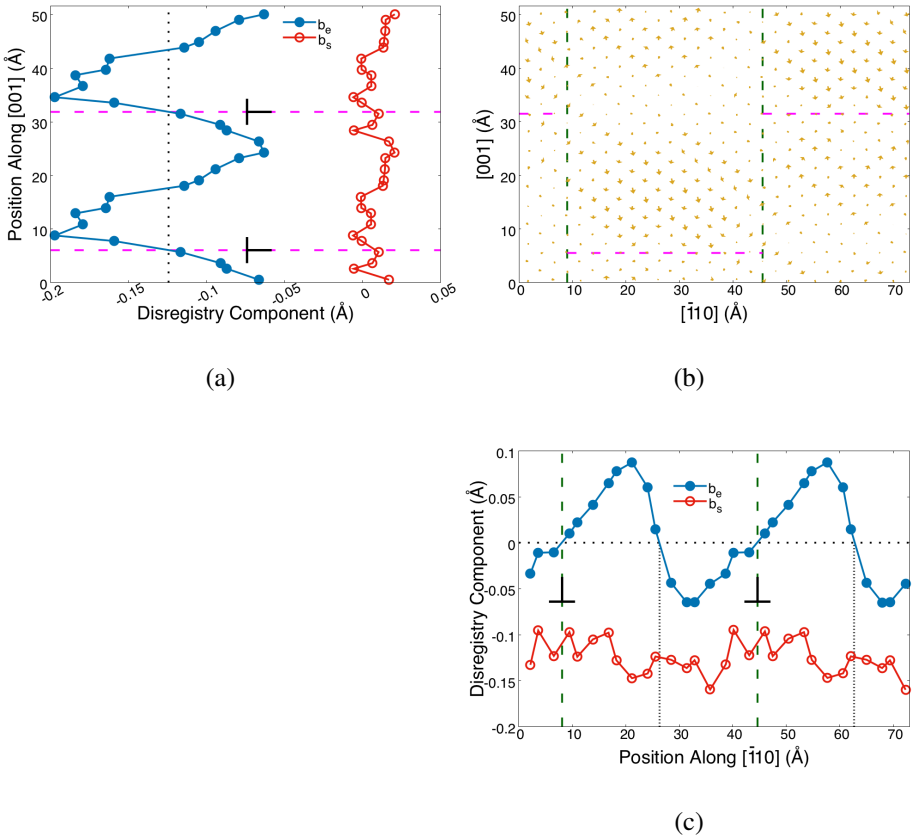

Figure 5.3: Disregistry analysis for $\{110\}$ U–Zr interfaces. (a) $[\bar{1}10]$ dislocation set disregistry components, $\hat{n}$ in the $[001]$ direction; (b) Full displacement disregistry field; (c) $[001]$ dislocation set disregistry components, $\hat{n}$ in the $[\bar{1}10]$ direction. Dislocation lines of the $[001]$ set do not align with dislocation cores, rather appearing at the periodic offsets.

Estimations of the dislocation core widths can also be obtained by examining the characteristic of the displacement disregistries for each dislocation set composing an interface. Specifically, the width of the dislocation core corresponds to the peak-to-peak distance between the maximum and minimum edge component of the displacement disregistries surrounding the dislocation core. Indeed, the peak-to-peak distance of the displacement disregistry corresponds the misalignment of the adjoining lattices induced by the presence of the dislocation.

Table 5.1 tabulates the measured dislocation core widths for the interfacial dislocation networks previously shown in Fig. 5.1. It should be noted that, for all the orientations simulated, the dislocation core width does not change with misfit strain as the physical

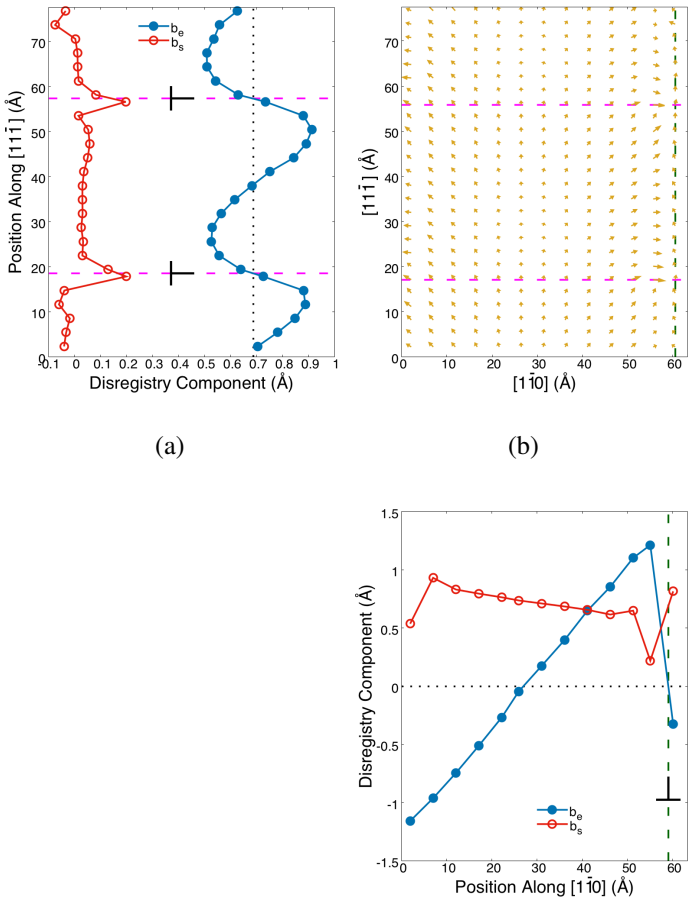

(a) (b)

(c)

Figure 5.4: Disregistry analysis for $\{112\}$ U–Zr interface. (a) $[1\bar{1}0]$ dislocation set disregistry components, $\hat{n}$ in the $[11\bar{1}]$ direction; (b) Full displacement disregistry field; (c) $[11\bar{1}]$ dislocation set disregistry components, $\hat{n}$ in the $[1\bar{1}0]$ direction.

Interface orientation	$\{001\}$	$\{110\}$		$\{111\}$	$\{112\}$	
Dislocation line direction	$[010]$	$[\bar{1}10]$	$[001]$*	$[11\bar{2}]$	$[1\bar{1}0]$	$[11\bar{1}]$
Dislocation core width (Å)	13.424	8.261	10.222	9.541	10.851	5.063

Table 5.1: Approximate dislocation core width for the $\{001\}$, $\{100\}$, $\{111\}$ and $\{112\}$ U–Zr interfaces. A single dislocation core width is presented for symmetrically identical dislocation sets. *The $[001]$ dislocation set is misaligned with the physical dislocation core.

spatial accommodation of the dislocation stays extremely localized. However, the misfit strain does impact the interfacial dislocation density in a linear fashion.

These atomistically-characterized dislocation network structures are compared to those calculated by the qFB formulation. Table 5.2 and Fig. 5.5 present both a quantitative and

	$\boldsymbol{\xi}_1$	$d_1(\mathring{A})$	$\boldsymbol{\xi}_2$	$d_2(\mathring{A})$	$\boldsymbol{\xi}_3$	$d_3(\mathring{A})$
$\{001\}$ DXA	$[010]$	43.7	$[100]$	43.7	-	-
$\{001\}$ qFB Conventional	$[010]$	45.5	$[\bar{1}00]$	45.5	-	-
$\{001\}$ qFB Primitive	$[00\bar{1}]$	45.5	$[01\bar{1}]$	32.17	$[010]$	45.5
$\{110\}$ DXA	$[\bar{1}1\bar{1}]$*	42.0	$[\bar{1}11]$*	42.0	$[\bar{1}10]$	50.6
$\{110\}$ qFB Conventional	$[001]$	74.2	$[00\bar{1}]$	74.2	$[\bar{1}10]$	52.5
$\{110\}$ qFB Primitive	$[\bar{1}1\bar{1}]$	42.9	$[\bar{1}11]$	42.9	-	-
$\{111\}$ DXA	$[11\bar{2}]$	66.7	$[\bar{1}2\bar{1}]$	66.7	$[\bar{2}11]$	66.7
$\{111\}$ qFB Conventional	$[0\bar{1}1]$	60.0	$[10\bar{1}]$	60.0	$[\bar{1}10]$	60.0
$\{111\}$ qFB Primitive	$[1\bar{1}0]$	60.0	$[01\bar{1}]$	60.0	$[\bar{1}01]$	60.0
$\{112\}$ DXA	$[1\bar{1}0]$	37.8	$[11\bar{1}]$	61.8	-	-
$\{112\}$ qFB Conventional	$[0\bar{2}1]$	49.8	$[20\bar{1}]$	49.8	$[\bar{1}10]$	78.8
$\{112\}$ qFB Primitive	$[1\bar{1}0]$	39.4	$[11\bar{1}]$	64.3	$[\bar{1}\bar{1}1]$	64.3

Table 5.2: Systems of dislocation network $\boldsymbol{\xi}_i$ directions and d_i spacings. *The $[\bar{1}1\bar{1}]$ and the $[\bar{1}11]$ dislocation sets calculated by DXA are much closer aligned to the $[001]$ direction than the $\langle 111 \rangle$ directions. For the purpose disregistry calculation they are treated as single merged $[001]$ dislocation set.

qualitative comparison respectively of the dislocation network directions $\boldsymbol{\xi}_i$ and spacing d_i as measured directly from the atomistic simulation or as predicted from the classical qFB formalism while considering either the primitive or conventional basis for the Bollman's O-lattice sites. It should be noted that, in the present comparison, considerations of the elastic relaxations [146] within the theoretical qFB formulation are not accounted for.

As seen in Fig. 5.1 and Fig. 5.5, while the $\{001\}$ and $\{112\}$ dislocation network structures as predicted by the classical qFB formulation match the DXA patterns from the atomic model, deviations between the theory and the atomistic system for the $\{110\}$ and $\{111\}$ stacking orientations. For the $\{110\}$ stacking orientation, the DXA algorithm identified three groups of dislocation lines, $[\bar{1}1\bar{1}]$, $[\bar{1}11]$ and $[\bar{1}10]$. However, comparison of Fig. 5.1(b) and Fig. 5.5(b) shows a clear realignment of the $[\bar{1}1\bar{1}]$ and $[\bar{1}11]$ dislocation lines, closely approaching the $[001]$ direction. These dislocation realignments are also accompanied by the appearance of a third dislocation line in the $[\bar{1}10]$ direction, which is not predicted by the classical qFB formalism using the primitive O-lattice basis. The shifts in dislocation network structure is hypothesized to be the result of dislocation-dislocation interactions

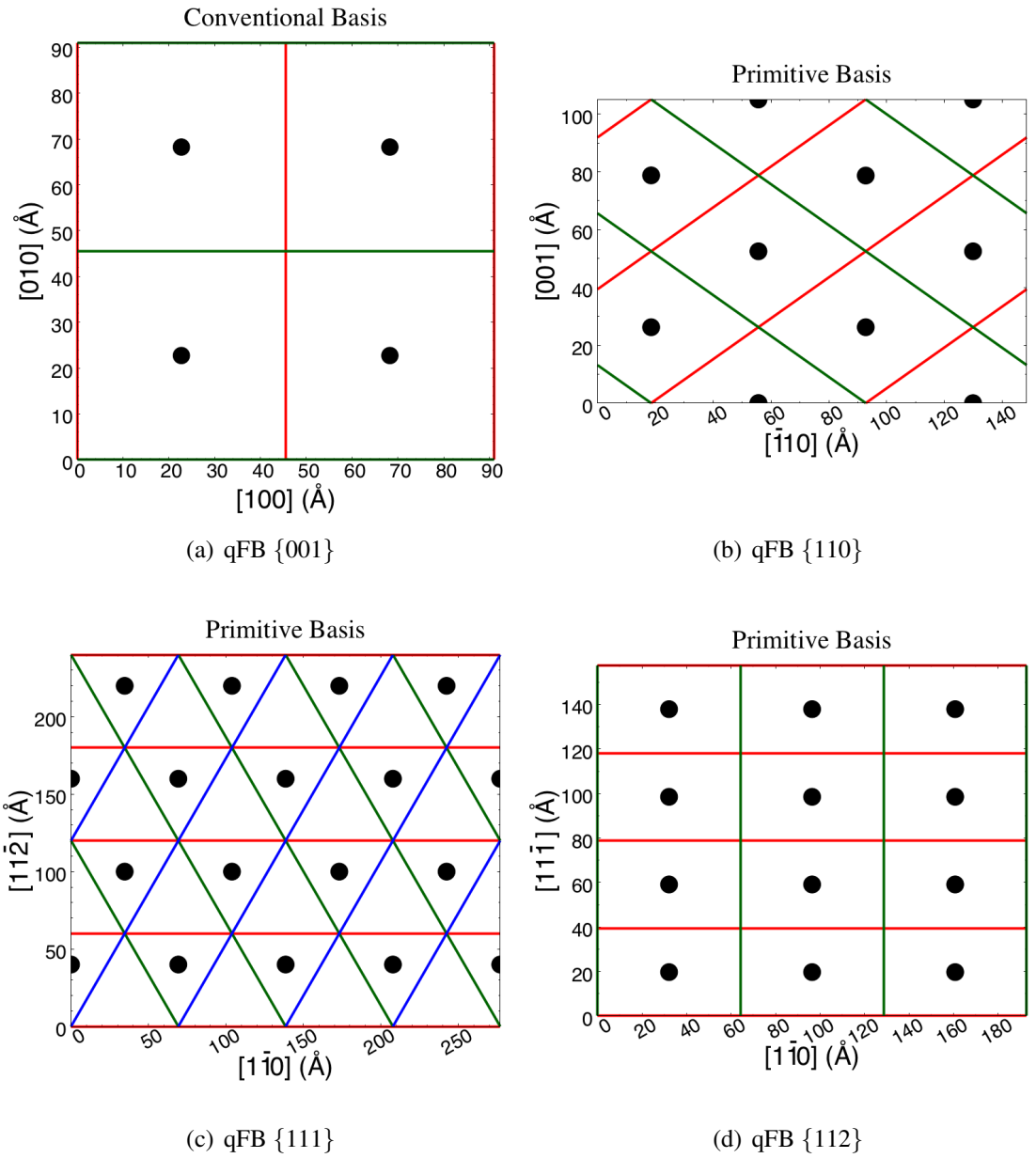

(a) qFB {001}

(b) qFB {110}

(c) qFB {111}

(d) qFB {112}

Figure 5.5: Misfit dislocation network. Closest matching quantized Frank-Bilby predictions for (a) {001}, (b) {100}, (c) {111} and (d) {112} U–Zr interfaces.

during elastic relaxation [146], since the amalgamation of the $[\bar{1}1\bar{1}]$ and $[\bar{1}11]$ dislocation lines can generate a new $[\bar{1}10]$ dislocation set. The merging of the two $\frac{1}{2}\langle 111\rangle$ dislocation sets would also explain why they are misaligned with the dislocation cores in the relaxed configuration. A similar shift of the dislocation network structure is also predicted by recent studies by Vattré [146] on the elastic strain relaxation of the FB patterns. Such theoretical

prediction showed how the dislocation network in an analogous closed-packed $\{111\}$ fcc plane can transform from the initial diamond pattern to a relaxed hexagonal pattern.

The classical qFB formalism also cannot predict the hextille dislocation network presented in the $\{111\}$ bcc stacking interfaces. This is not surprising as the qFB formulation was restricted to sets of infinitely straight dislocations, and is inherently incapable of generating the discontinuous hextille dislocation patterns. Instead, the classical qFB formulation predicts two similar sets of deltille networks as shown in Fig. 5.5(c). The transformation of the deltille network to the hextille network can conversely be explained by the merging of adjacent dislocation lines, resulting the pattern observed from the DXA results.

Overall the close agreement amongst the dislocation sets from the interfacial atomistic system, disregistry analysis of the misfit interface structures and qFB predictions confirm the precise characterization of the interfacial dislocation networks as tabulated in Table 5.2.

5.3.2 Interfacial excess energy

To quantitatively assess the impact of the presence of the interfacial dislocation network on the phase boundary behaviors, the interfacial excess energy is evaluated as function of misfit strain.

The interfacial excess energy for each stacking and misfit configuration is calculated using

$$\Gamma = \frac{1}{2A}\left[\sum_{i=1}^{N_U}(e_U^i - e_U^{bulk}) + \sum_{i=1}^{N_{Zr}}(e_{Zr}^i - e_{Zr}^{bulk})\right], \tag{5.3}$$

as defined by Dingreville and Qu [163]. Here, A denotes the surface area, N_U and N_{Zr} denote the total number of atoms in uranium and zirconium respectively, and e^i and e^{bulk} represent the per-atom potential energy and average potential energy within the bulk (i.e., far from the boundary) respectively. By calculating the excess energy of all the boundary variations generated with the Γ-surface technique, the most favorable interfacial structures are identified for each misfits strain and stacking orientation and correspond to those with the minimum interfacial excess energy. Minimum excess interfacial energies for each of

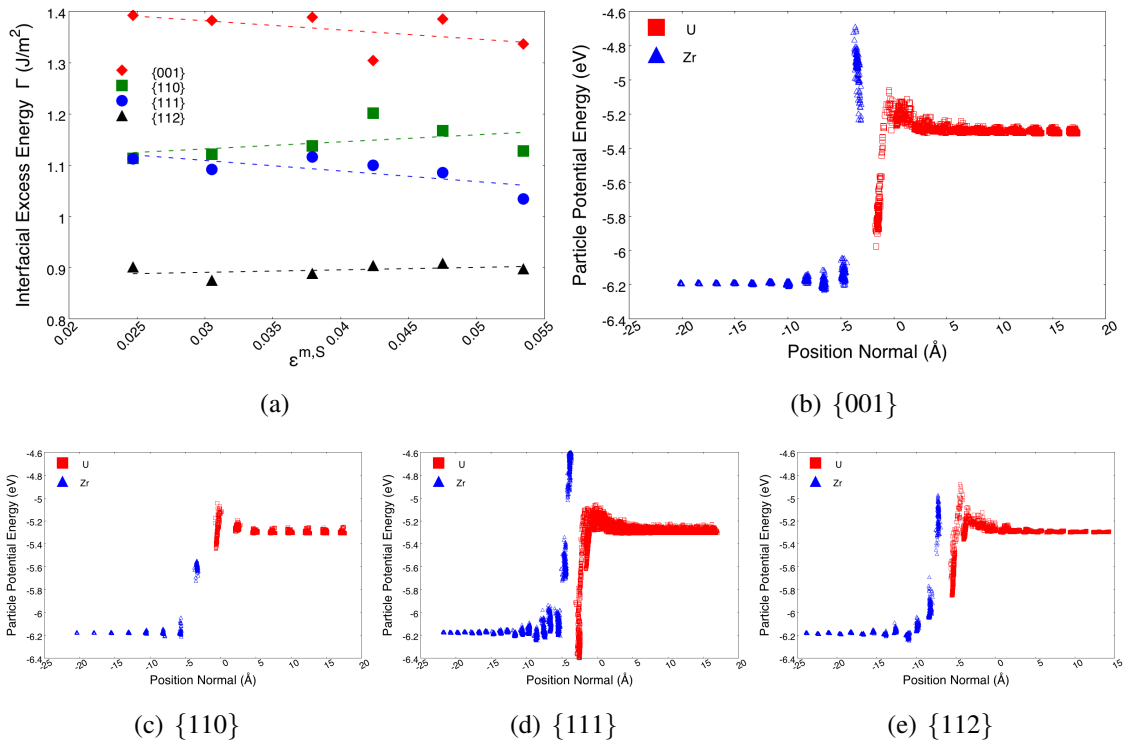

Figure 5.6: Phase boundary energetics (a) Interfacial excess energy vs misfit strain; Atomic potential energy density-of-state near the (b) $\{001\}$; (c) $\{110\}$; (d) $\{111\}$; (e) $\{112\}$ stacking interfaces. The interfacial excess energy Γ is linearly correlated with the misfit strain $\epsilon^{m,S}$. However, this dependence is weak due to the overwhelming cohesive energy well feature formed by the U and Zr atoms.

the 24 misfit strain and stacking orientation combination are shown in Fig. 5.6(a). As predicted from theoretical considerations [158], the observed interfacial excess energy Γ exhibits a linear dependence with respect to the misfit strain $\epsilon^{m,S}$. However, this dependence remains relatively small for all stacking orientations reflecting the fact that the structure of the interface remains unchanged while being stretched. Additionally, as illustrated in Fig. 5.6(b)–5.6(e), the examination of the atomic energy density-of-state near the interface reveals that the interfacial excess energies are largely dominated by the chemical bonding near the interface rather than the actual geometrical structure and associated elasticity features of the interface. Indeed, the presence of cohesive energy wells bridging the energy gap between the two bulk lattice structures are a differentiating characteristic of bi-material miscible phase boundaries as compared to grain or immiscible phase boundaries. In the

present study, in the case of U–Zr interface systems, these large cohesive energy wells reside in physical regions where the dislocation networks are prevalent. As such, any elastic energy features generated by the interfacial dislocation defects is overwhelmed by the significantly larger chemical potential binding energies.

Interface orientation	$\{001\}$	$\{110\}$	$\{111\}$	$\{112\}$
Thickness (Å)	10.90	13.01	14.94	13.39

Table 5.3: Approximate thickness of the $\{001\}$, $\{100\}$, $\{111\}$ and $\{112\}$ U–Zr interfaces, as calculated from interfacial energetics.

Since the chemical cohesive energy wells is the dominating energy feature at the miscible interfaces, the interfacial thicknesses, defined as the distance over which the atomic energies deviate from those in the respective bulk, can also be interpreted as the widths of the cohesive energy wells. Table 5.3 presents the energetically derived characteristic interfacial thickness for the different stacking orientations. These estimated interfacial thicknesses do not have any significant variations with misfit strain, again reinforcing the fact the cohesive energy wells are largely characteristic to the stacking orientations and the chemical bonding between interfacial atoms. The interfacial thicknesses are also comparable in value to the dislocation core widths provided in Table 5.1. If the dislocation core induced lattice distortion is assumed to be somewhat isotropic, then the strain energy features would also exist within the same range where cohesive energy well is dominant.

5.3.3 Residual elastic fields from network of misfit dislocations

To measure the residual elastic effect of the interfacial dislocation networks and identify the various stress concentration sites and preferred dislocation emission pathways, the planar principal stress fields are plotted in Fig. 5.7. The stress concentration sites are well aligned with the dislocation sets identified by the DXA algorithm and the disregistry analysis. These stress features are also very localized and quickly disappear within two to three lattice spacings away from the dislocation lines. The overall stresses are compressive in the

U lattice and tensile in the Zr lattice, as expected from the $m > n$ simulation constructs, where the extra atoms exist inside the U sublattice.

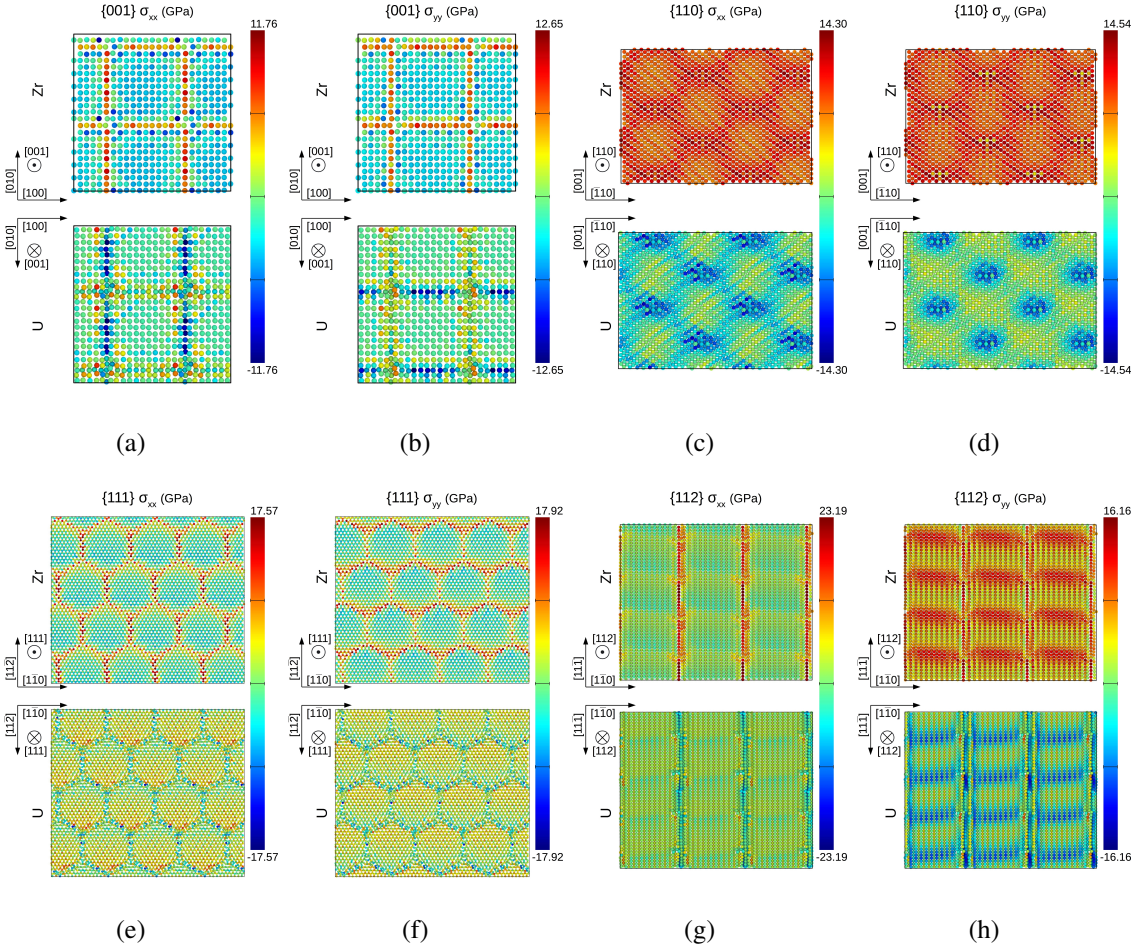

Figure 5.7: Interface adjacent planar stress fields σ_{xx} for: (a) $\{001\}$,(c) $\{110\}$,(e) $\{111\}$,(g) $\{112\}$ stacking interfaces. and σ_{yy} for: (b) $\{001\}$,(d) $\{110\}$,(f) $\{111\}$,(h) $\{112\}$ stacking interfaces.

In addition to interfacial planar stresses, the residual strain maps are used to identify long range dislocation emission pathways generated by the interfacial dislocation network. Figure 5.8 shows the Eulerian-Almansi interfacial normal strain ϵ_{zz} over the entire $\{001\}$, $\{110\}$, $\{111\}$, $\{112\}$ stacking super lattices. The per-atom Eulerian-Almansi strain tensor $\mathbf{e}$ is calculated using

$$\mathbf{e} = \frac{\mathbf{1}}{\mathbf{2}}\left[\mathbf{I} - (\mathbf{F^e})^{-\mathbf{T}}(\mathbf{F^e})^{-\mathbf{1}}\right], \tag{5.4}$$

where the per-atom deformation gradient tensor $\mathbf{F^e}$ is computed with respect to the relaxed

bulk U or Zr lattice configurations. Note that strain tensor calculations are omitted at the dislocation cores due to the drastic structural changes. Atoms are color coded by their interfacial normal strain ϵ_{zz} with the strain range set to $-5\% \sim +5\%$ in order to highlight certain strain features. Probability distributions of normal strains are also shown separately for U and Zr to show the full ranges of normal strain ϵ_{zz}.

Well defined strain features can be seen for all four stacking orientations, close to the interfacial boundary. In the $\{111\}$ and $\{112\}$ interfaces, these short range strain field features quickly terminate as one gets further away from the interfaces. However, this is not to say that long range strain features do not exist. In the $\{110\}$ interface, the close-range strain features transforms into discrete bands emitted away from the interface in the direction normal to the interface. Due to periodic constraint placed on the dislocation network, and therefore the simulation cell, a nominal interfacial planar compliance strain does exist as a consequence of the simulation setup. The planar compliance strain would limit the dissipation and redistribution of elastic fields away from the interface, which should be expected in a real material system. Second, the strain maps plotted in Figure. 5.8 correspond to fairly high misfit strain with densely spaced dislocation networks. It is fully within the range of possibility for the strain features to dissipate, should the spacing between periodic dislocations become sufficiently large.

5.4 Discussion and conclusions

This study examines the misfit dislocation networks in miscible semi-coherent phase boundaries in the case of U–Zr interfaces. These interfacial dislocation network are analyzed by utilizing a combination of atomistic simulations and theoretical predictions. Classical techniques such as DXA, disregistry analysis have been utilized on the atomistic system to characterize the dislocation network for various stacking orientation in terms of the nature and characteristics of the dislocations composing the misfit dislocation network (orientation, spacing, Burgers' vector). Characterizations from the atomistic model have been compared

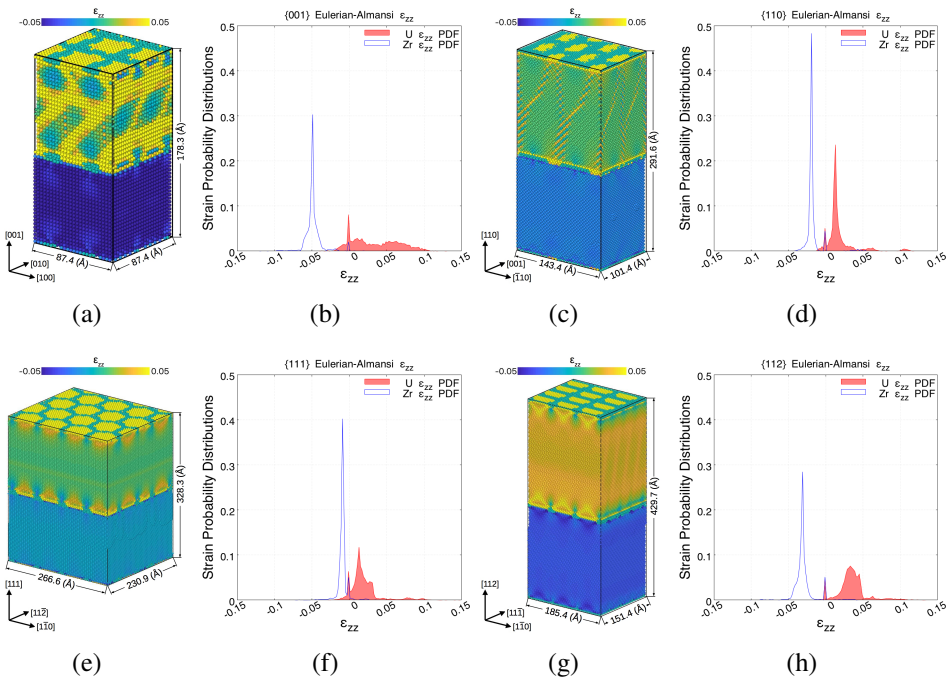

Figure 5.8: Atomic strain analysis for U–Zr interfaces. (a),(c),(e),(f): Normal strain field ε_{zz} for $\{001\}$, $\{110\}$, $\{111\}$, $\{112\}$ stacking interfaces. (b),(d),(f),(h): Probability distribution function of ε_{zz} for $\{001\}$, $\{110\}$, $\{111\}$, $\{112\}$ stacking interfaces.

with theoretical predictions from the classical qFB formalism. Discrepancies between the atomistic model and theoretical predictions point out to the predominant role of the chemical binding in the case miscible boundaries. Indeed, such effect is not accounted for in the classical qFB formalism or its extensions [146]. In the present example of miscible phase boundaries in U–Zr, the elastic dominance is not universal, especially for phase boundaries between two distinct, but miscible materials. The large gap in cohesive energy between U and Zr, combined with the miscibility of the material generated the orientation dependent cohesive energy wells. At every stacking orientation, the larger cohesive energy well has interwoven and overridden the elastic energy features, rendering the interfacial excess energies to near constants. The dominance of chemical over elastic interaction is consistently observed across all four interfaces. Such effects are in agreement with the theory of thermochemical equilibrium of solids which considers the competition between chemical and elastic interactions at an interface, as described by Larché and Cahn [164, 165, 166]. This

study highlights the fact that in the case of miscible interfaces, the utilization of theoretical predictions such as the qFB framework or its extensions needs to considered with care.

CHAPTER 6
IRRADIATION RESISTANCE OF NANOSTRUCTURED INTERFACES IN ZR-NB METALLIC MULTILAYERS [115]

Having obtained a baseline knowledge of radiation defect production from Chapter 3 and phase boundary characteristics from Chapter 5, Chapter 6 seeks to explore the accumulation and evolution of radiation defects in metallic multilayers. By adapting the state-of-the-art FPA technique introduced in Chapter 2, large dose electron irradiation is simulated for bulk Zr, bulk Nb and three different phase boundary combinations. In order to answer **Q1: How are radiation defects produced in bulk crystals, and what are the mechanisms of defect accumulation?**, we first examine defect accumulation in the bulk crystals. Despite the differences in lattice structures and defect formation behaviors, three similar stages of dislocation accumulation, saturation and coalescence emerged for both Zr and Nb. Using bulk behaviors as the basis for comparison, we then investigate **Q2: How do phase boundaries affect radiation defect accumulation, and how does the interfacial microstructure evolve?** using the three Zr–Nb multilayers. While analysis shows that phase boundaries do act as a defect sinks early on, radiation-induced intermixing eventually triggers phase transformations in the Zr–Nb mixture. This physical phenomenon resulted in the emission of a large quantity of small immobile dislocation loops from the phase boundaries. Surprisingly, the evolution of the boundary microstructures appears to be largely a function of inter-metallic composition mixing, with little or no dependence on interfacial geometry.

6.1 Introduction

Upon exposure to radiation environments, materials typically experience damage in the forms of defects such as: vacancies, interstitial, dislocation loops, point defect clusters,

voids, cavities, and etc., each associated with their distinct dimensionality. Over time, the accumulation of such defects can severely degrade a material's mechanical, physical and chemical performance. Regardless of its crystal structure (FCC, BCC or HCP), the engineering of radiation resistance materials focuses primarily mostly on the management rather than the prevention of radiation-induced defects. Grain and phase boundaries are key microstructural elements in the management of radiation-induced defects in crystalline materials. Indeed, these boundaries can be considered as preexisting microstructural defect sinks capable of trapping and potentially eliminating small-scale radiation-induced defects. Due to their abundance of grain and phase boundaries, nanostructured materials have been identified as one possible class of materials possessing radiation resistance superior to conventional materials [167]. Numerous examples of nanostructured materials take advantage of the defect sink capacities of boundaries to alleviate radiation damage including: nanocrystalline materials with a high density of small grains [168, 169], nanotwinned metals with a high density of twin boundaries [170, 171], multilayer nanocomposites with a high density of stacked heterophase boundaries [148, 172], or nanoporous materials containing a large number of free surfaces [173, 174].

Of particular interest to this study are metallic nanocomposites with heterophase layer interfaces [148, 175, 176, 172] acting as defect sinks to improve radiation tolerance. Layered nanocomposites are unique in terms of the multiplicity of length scales available to design and optimize their radiation resistance. Geometrically speaking, the layer thickness of each constituent provides an extrinsic length scale that can be controlled down to a few nanometers to devise the overall and effective sink strength and sink efficiency of the nanocomposite. Alternatively, the physical structure of the heterophase boundaries and the chemical nature of the chemical bonds formed across interface planes [131] provide intrinsic length scales that can be leveraged to manage radiation-induced defects. At the intersection of these length scales, there is also the inherent length scale associated with the interactions between the defects and the boundaries, the complexity of which cannot be

understated. In this study, we primarily explore intrinsic size effects of the defect-boundary interactions.

Due to the atomic nature of the radiation-induced damage production, researchers have used Molecular Dynamics (MD) and atomic kinetic Monte Carlo (akMC) models to study intrinsic size effect phenomena of defect-interface interactions. Many researchers have focused on the role of phase boundaries as a microstructural component to enhance sink efficiency and sink strength. They studied the effects of either misfit dislocation arrays [139, 140] or elastic interactions (coherency stresses) [177, 34] to draw conclusions on defect sink characteristics based on thermodynamic considerations of point defects energetics near these boundaries. Other researchers [148] have explicitly investigated defect-boundary interactions between pristine boundaries and isolated or few cascade(s). However, these studies only capture the extremely early stage of defect-boundary interactions. For instance, Fig. 6.1 shows the result of a 10 keV cascade interacting with a pristine Zr–Nb boundary. This example illustrates that not only the defects produced are few and far between, but also that the interfacial structure remains largely intact. While a few researchers [178, 179, 52, 172] have studied the morphological evolution of phase boundary structures as triggered by irradiation-induced intermixing, to our knowledge, none thus far have considered how the morphology changes the defect-boundary interactions.

In this study, we simultaneously examine the morphological evolution of both the phase boundary structures and the irradiation defects. Using Zr–Nb [180] as a case study, we investigate how defect-boundary interactions and their associated intrinsic length scales change over a large dose range. We consider three common interfacial stacking orientation relationships (ORs) for HCP (Zr) and BCC (Nb) multilayers. The first two ORs share similar stacking interfacial planes of (0001)——(011), with the $[2\bar{1}\bar{1}0]$——$[1\bar{1}1]$ and the $[11\bar{2}0]$——$[100]$ alignments known as the Burgers [181] and Pitsch-Schrader (P-S) [182] respectively. These two stacking orientations have been observed experimentally in similar HCP–BCC Mg–Nb multilayers by Chen et al. [140]. The third OR con-

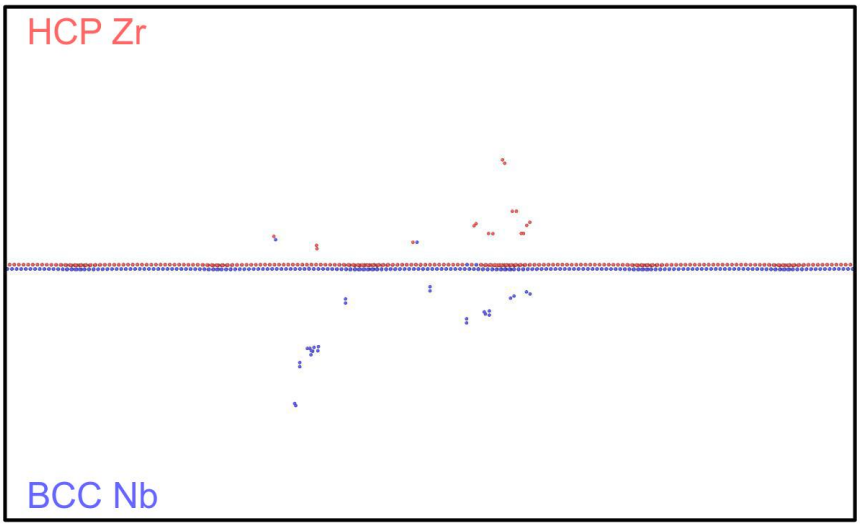

Figure 6.1: Remaining point defects after a 10 keV Primary Knock-on Atom (PKA) collision cascade in the vicinity of a Zr–Nb phase boundary. Atoms colored in blue correspond to point defect in BCC Nb. Atoms colored in red correspond to point defect in HCP Zr.

sists of an $(1\bar{2}10)$——$(\bar{1}00)$ and $[\bar{1}010]$——$[0\bar{1}1]$ orientations, and is taken directly from high-resolution transmission electron microscopy (TEM) studies of Nb nano-precipitates in Zr [183]. All three structured interfaces are illustrated in Fig. 6.2 in the Methods Section 6.2.

The paper is organized as follows. In the Methods Section, we describe the novel atomistic technique, known as the Frenkel Pair Accumulation (FPA) method. This technique consists of cumulatively introducing point defects in the atomistic system to accelerate the simulation of irradiation processes and defect evolution. In Section 6.3.1, we establish the mechanisms for defect accumulation in both bulk phases. In Section 6.3.2, we quantify the boundary effect on the defect evolution. Finally, in Section 6.4, we discuss the effect of irradiation intermixing on the morphology of the interfaces.

6.2 Methods

In this study, we used the atomistic simulation code LAMMPS (Large-scale Atomic/Molecular Massively Parallel Simulator [93]) to study the radiation resistance of Zr–Nb heterophase

boundaries. We selected and employed the Angular Dependent Potential (ADP) developed by Smirnova and Starikov [184] to model the interatomic interactions in Zr–Nb metallic multilayers. This potential, fitted to ab-initio results, is able to accurately replicate point defect formation and diffusion in multiple phases of Zr, BCC Nb as well as the mixed alloys. Since we are not using the Primary Knock on Atom (PKA) technique to generate radiation-induced damage, no modification (nuclear or electronic stopping) was added to this interatomic potential.[51] We performed the identification and quantification of the irradiation defects using the Dislocation Extraction Algorithm (DXA) [149] as implemented in the OVITO software package.[100] Our simulation technique is composed of two steps: (i) the construction of the three stacking orientations for Zr–Nb heterophase boundaries, and (ii) the accelerated introduction and evolution of irradiation defects in the vicinity of these boundaries.

6.2.1 Zr–Nb multilayer construction

The atomistic construction of a Zr–Nb heterophase (incoherent) boundaries consists of two stacking bulk crystals with periodic boundary conditions applied in all directions. Periodicity in the stacking normal direction transforms the two bulk crystals into alternating multilayers. To achieve the correct stacking orientation relationships, both bulk crystals are rotated with respective to one another. As lattice periodicities in the simulation frame shift upon rotation, atom numbers are slightly adjusted to eliminate any non-interfacial mis-stacking defects.

For the Burgers and P-S ORs considered in this study, we constructed our simulation cells to be approximately 250 Å$\times$ 500 Å$\times$ 500 Å, with each bulk layer taken as approximately 250 Åin thickness. In the case of the Burgers OR multilayer, our simulation contains 1,347,840 Zr atoms and 1,767,744 Nb atoms respectively; in the case of the P-S OR multilayer, our simulation contains 1,347,840 Zr atoms and 1,756,512 Nb atoms respectively; and in the case of the nano-precipitate OR multilayer, our simulation contains 1,347,840

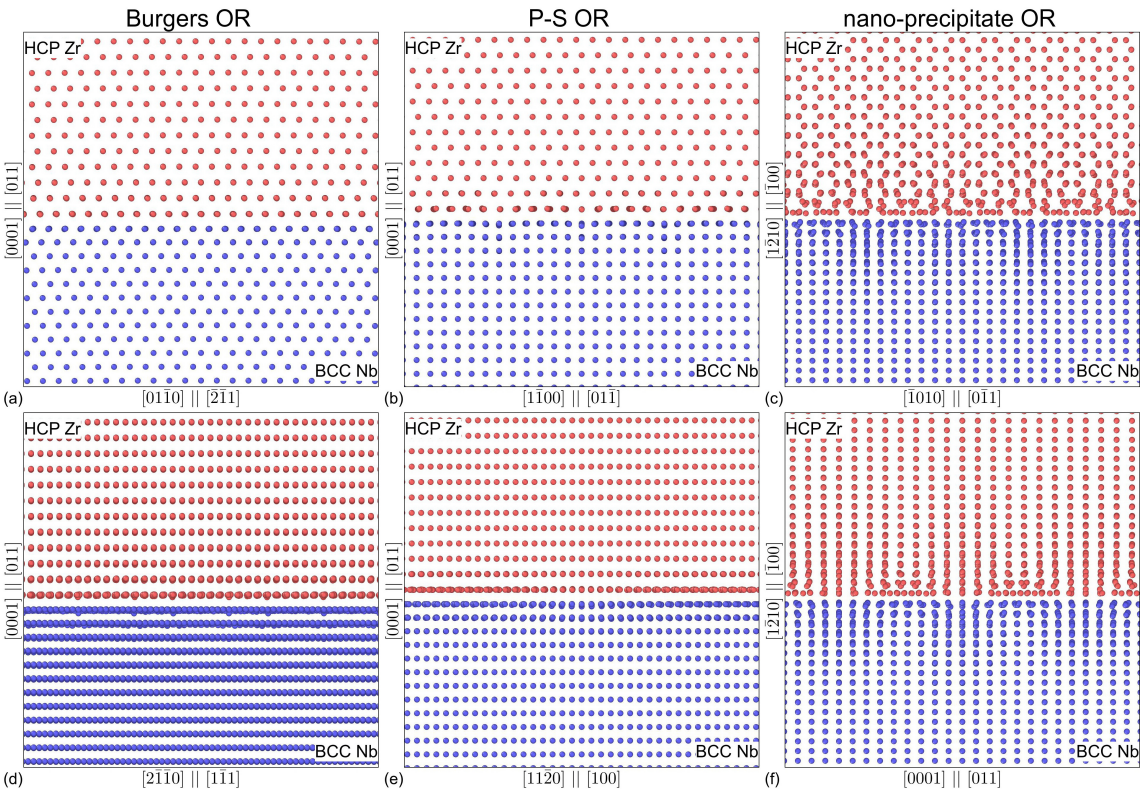

Figure 6.2: Structured multilayer interfaces for Burgers OR (a) and (d), P-S OR (b) and (e) and nano-precipitate OR (c) and (f).

Zr atoms and 1,772,928 Nb atoms respectively.

To allow for the relaxation of misfit stacking strains and the formation of interfacial microstructures, we performed an energy minimization step with isobaric ($P = 0$) constraint to the three individual constructed multilayers. Figure 6.2 illustrates the relaxed atomic structures near the three phase boundaries. Periodic clustering of atoms at the boundary layers clearly indicate the existence of various interfacial dislocation networks, as reported elsewhere [140, 131].

6.2.2 Frenkel pair accumulation (FPA)

In order to simulate the evolution of irradiation defects over a significant dose range, we adopted the Frenkel Pair Accumulation method [114, 58, 185]. The schematic for the FPA method is shown in Fig. 6.3. The FPA method introduces radiation damage directly

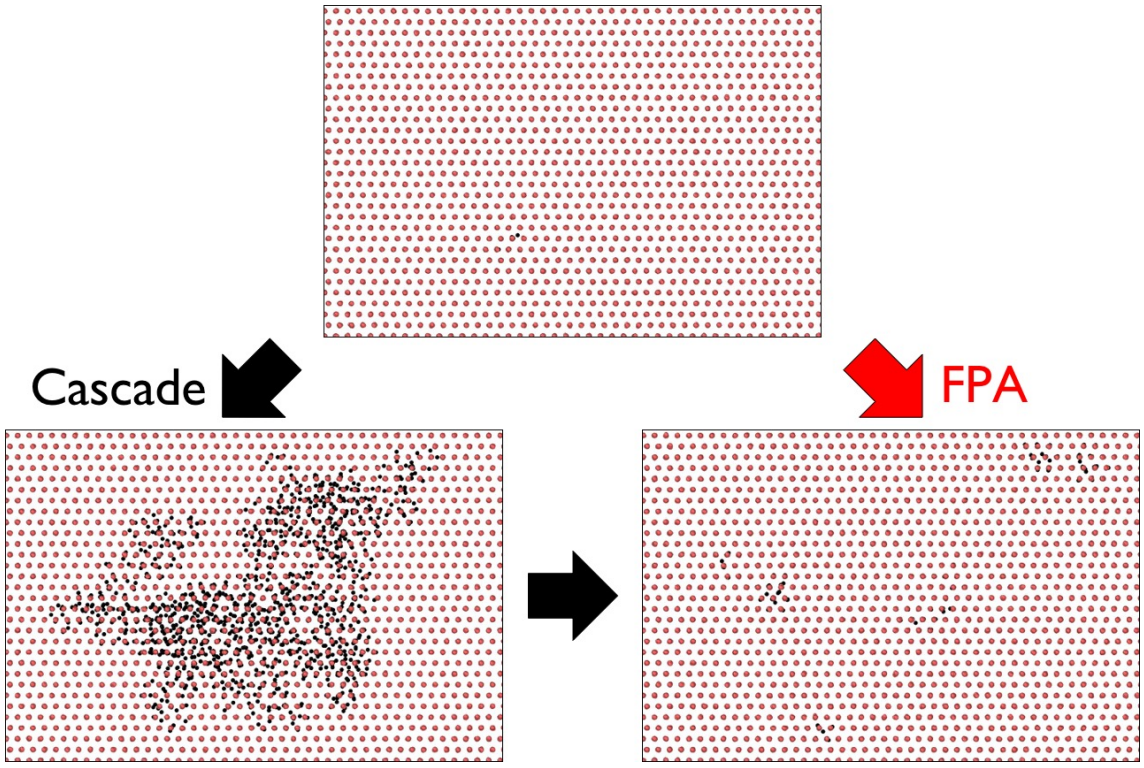

Figure 6.3: Schematics of Frenkel Pair Accumulation [58] (FPA) method.

as interstitial-vacancy point defect (Frenkel) pairs as observed at the end of the collision event, bypassing the various stages of cascade evolution. Each Frenkel pair is generated within the simulation cell by randomly selecting and displacing an atom from its initial lattice site. In turn, the initial atom site becomes a vacancy site; and the displaced atom becomes a interstitial site, thus creating a Frenkel pair. Since the original method presented by Chartier et al. [58] was developed for ceramic systems with large sparse lattices, we included an additional optimization step for the denser metallic systems that is Zr–Nb. In this additional step, at each interstitial defect site, the nearest neighbors of the displaced atom are nudged radially up to 2 Åaway from the center of the interstitial site. This nudging adjustment is intended to perform three primary functions: (i) preventing atom position overlap, (ii) reducing local heating from close-range repulsion and, (iii) allowing more defect pairs to be introduced simultaneously.

To better match the radiation-induced damage introduced using the FPA method to

that of a collision cascade, we have parameterized the maximum allowed displacement distance using the Stopping and Range of Ions in Matter (SRIM) software [186]. Using SRIM, we calculated the first collision range in both Zr and Nb target mediums for a maximum incident energy of 20 keV. We simulated same-specie collisions to approximate collision cascades initiated well within the respective bulk. In addition, we also simulated cross-species collisions to approximate collision cascades initiated in the vicinity of the heterophase boundaries. SRIM calculations yielded the first collision range of Zr→Zr, Nb→Nb, Zr→Nb, Nb→Zr to be 104 Å, 77 Å, 78 Å, 103 Årespectively. Taking the approximate average of the four test cases, the upper bound on atom displacement range is set to 90 Å. To reduce the possibility of spontaneous recombination and elimination of the new Frenkel pairs, the lower bound of the atom displacement is set to the value of 20 Å. The large separation of vacancy and interstitial defects is also a characteristic feature of high-energy irradiation, in which the interstitial defects cluster at the outer edge and the vacancy defects cluster at the inner core of the collision cascade [48].

At each time interval, we introduced $\mathrm{n_{fp}} = 5,000$ randomly generated Frenkel pairs. To offset the localized heating at the new interstitial sites and allow for defect evolutions, we subsequently relax our interfacial atomic system for 2 ps using an isobaric NPT ensemble. This process is repeated until the total dose/damage reaches the damage level of 1 dpa (displacement-per-atom), where $\mathrm{dpa} = \frac{\mathrm{n_{fp}}}{\mathrm{N_{atoms}}}$, with $\mathrm{N_{atoms}}$ being the total number of atoms in the entire atomic system considered. Effective dose/damage rates in bulk Zr, bulk Nb and larger multilayer systems are approximately 0.00371 dpa/ps, 0.00285 dpa/ps, and 0.00080 dpa/ps respectively.

6.3 Results

6.3.1 Mechanisms for defect accumulation in bulk phases

In order to understand the morphology evolution of both the phase boundary structure and the irradiation-induced defects, we must first examine the defect accumulation in isolated

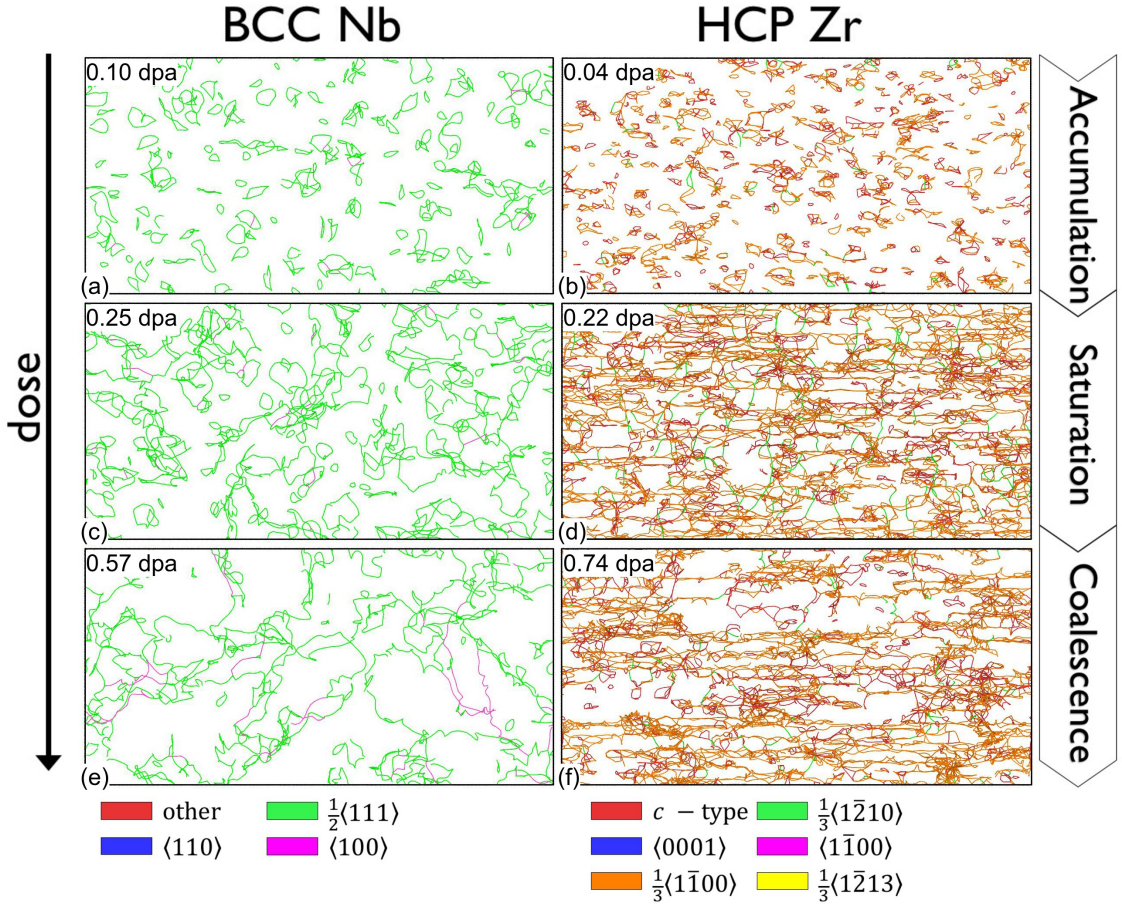

Figure 6.4: Process of the defect accumulation in Nb and Zr bulk phases: (a) and (b) correspond to the defect accumulation stage; (c) and (d) correspond to the defect saturation stage and; (e) and (f) correspond to the defect coalescence stage.

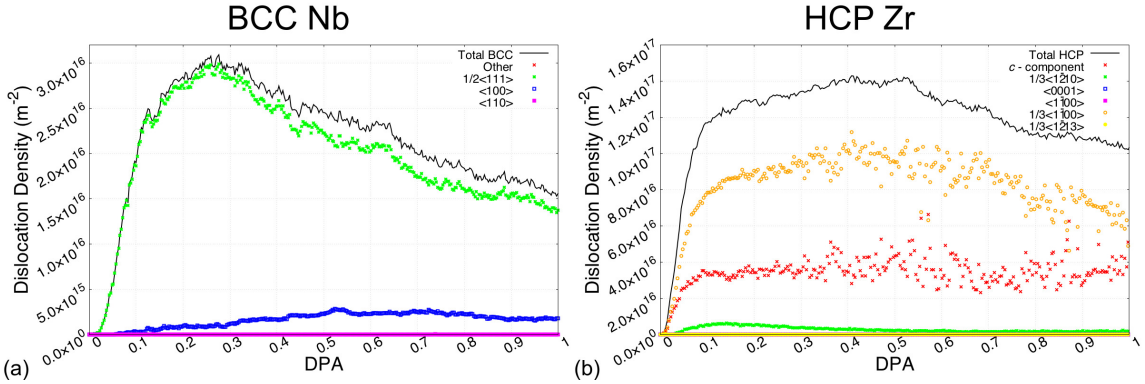

Figure 6.5: Dislocation density vs displacement-per-atom (dpa) in (a) BCC Nb bulk phase and, (b) HCP bulk phase Zr. The total dislocation density is partitioned as a function of the nature of the dislocation loops as indicated by the various symbols.

bulk metals.

To this end, we have simulated defect accumulation up to a damage level of 1 dpa in the two bulk systems of HCP Zr (1,347,840 atoms) and BCC Nb (1,756,512 atoms) respectively. Note that over the large dose/damage level examined, the primary defects generated are dislocations. While point defect accumulation and clustering processes are present, they are not explicitly shown. We illustrate in Fig. 6.4 the three primary stages of dislocation defect evolution in bulk Zr and bulk Nb: (i) accumulation, (ii) saturation, and (iii) coalescence. In complement, we also provide in Fig. 6.5 the quantification of dislocation density, by type, as a function of the dose. For ease of comparison with the multilayer systems, assuming each bulk metal act as a half volume of a reference multilayer. Dislocation densities in bulk metals are calculated as:

$$\rho_{\mathrm{Zr|Nb}} = \frac{N_{\mathrm{Zr|Nb}}}{V_{\mathrm{Zr}} + V_{\mathrm{Nb}}} \quad \text{and} \quad V_{\mathrm{Zr}} = V_{\mathrm{Nb}}, \tag{6.1}$$

where $N_{\mathrm{Zr|Nb}}$ is total length of dislocation segments in Zr and Nb respectively. V_{Zr} and V_{Nb} are the volumes of the bulk Zr and Nb phases respectively.

Throughout the process of dislocation generation and evolution, each stage can be associated with an intrinsic size scale related to the defect evolution:

1. The first stage consists of the production of exclusively of small dislocation loops, formed by the clustering of point defects. Due to the relative sparse distribution of dislocations, interactions between neighboring defects are infrequent. Consequently, small loops do not experience any growth and simply accumulate in quantity at a constant rate. In Fig. 6.5 (a) and (b), this first stage is identified by the initial sharp rise in dislocation density from 0.0 to 0.1 dpa.

2. The second stage begins when the dislocation density reaches a sufficient concentration, and interactions between neighboring small dislocations loops become more frequent. Initial interactions between small dislocation loops tend to form compound

dislocation structures, which over time (i.e., as the damage level increases) collapse into larger, more stable, dislocation loops. This process is what is referred to as coalescence. As a result, the second stage contains both small and medium dislocation loops. With the coalescence process, there is some loss of dislocation content due to the reorganization of compound dislocations. This counteracts the effect of dislocation accumulation, slowing the growth of the dislocation densities. At that moment, the balance remains in favor of accumulation, as dislocation densities slowly climb to peak saturations. For BCC Nb (Fig. 6.5(a)) and HCP Zr (Fig. 6.5(b)), the second stage occurs at 0.1→0.3 dpa and 0.1→0.5 dpa respectively.

3. By the time the defect evolution reaches the third and last stage, significant coalescence between dislocation loops has already occurred to form large sprawling dislocation forests, nanometers in size. While small dislocation accumulations are not apparent at this stage, they are still present. The only difference here is that the newly nucleated small dislocation loops quickly latch onto and merge with the existing large dislocations. Further coalescence of medium and large dislocation loops continues to lower the dislocation densities at this stage. At higher doses, the depletion of dislocations also becomes visually apparent, as seen in Fig. 6.4(e) and 6.4(f).

Overall, the accumulation of defects is not a simple matter of density, but rather a complex evolution of defect sizes with two competing processes of accumulation and coalescence. It should be noted that all three stages described above can also be found in other materials systems [58].

One unique feature of the HCP phase is the nature of the dislocations that generated based on the type of irradiation condition [187, 188]. Particularly, in the well-studied case of zirconium [189, 190, 191], the dislocation types and quantities can be directly compared against experimental results. As plotted in Fig. 6.5(b), the three main types of dislocations are c-component, $\frac{1}{3}\langle 1\bar{1}00\rangle$, and $\frac{1}{3}\langle 1\bar{2}10\rangle$, in decreasing order of concentrations. The c-component type dislocations can be further analyzed into sub-type classifications,

namely $\frac{1}{6}\langle 20\bar{2}\bar{3}\rangle$, $\frac{1}{9}\langle 1\bar{1}03\rangle$, $\frac{1}{18}\langle \bar{2}\bar{4}63\rangle$, $\frac{1}{18}\langle \bar{4}043\rangle$. The large presence of c-component type dislocations and the absence of $\langle a\rangle$-type ($\frac{1}{3}\langle \bar{1}\bar{1}20\rangle$) dislocations provide a fairly close match to the experimental case of high dose electron irradiation [192, 191]. This validation is not entirely surprisingly, as the FPA method used to introduced radiation-induced damage (see Methods Section) is tailored to rapidly generate dispersed point defects, much like electron irradiation.

6.3.2 Mechanisms of defect accumulation in multilayer heterophase boundaries

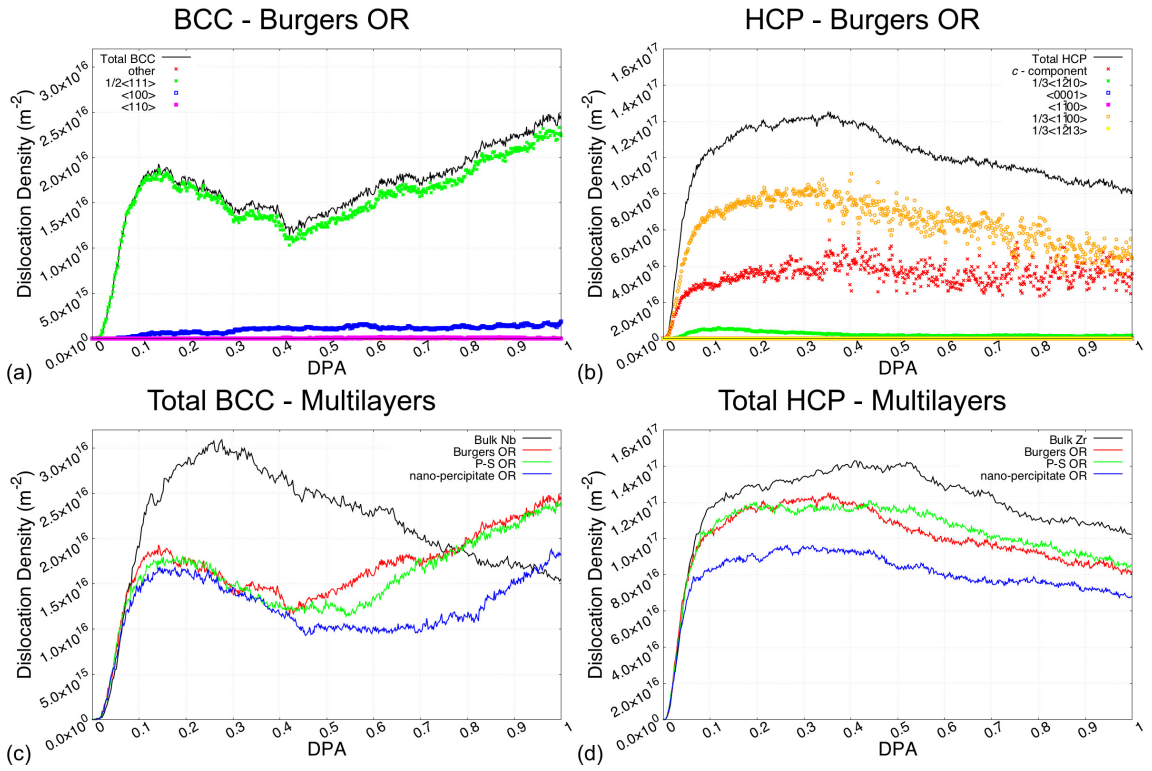

Figure 6.6: Dislocation density evolution in Zr–Nb phase multilayers. (a) Dislocation density in Burgers OR multilayer in the BCC phase. (b) Dislocation density in Burgers OR multilayer in the HCP phase. (c) Comparison of total BCC dislocation densities in bulk Nb with the Nb phase of the multilayered nanocomposite for all orientations studied. (d) Comparison of total HCP dislocation densities in bulk Zr with the Zr phase of the multilayered nanocomposite for all orientations studied for all orientations studied.

Having established the mechanisms for defect evolution in each respective bulk phases, we now examine the mechanisms of defect accumulation in the corresponding multilayer

heterophase boundaries. In Fig. 6.6, we present the evolution of the dislocation densities as a function of the damage level for the three multilayer ORs considered. For reference, we compare the total dislocation densities against those of the bulk phases. Using the Burgers OR multilayer as a representative example, we show in Fig. 6.7 and 6.8 the evolution of the dislocation contents as a function of the damage level, along with the set of dislocation Position vs Length (PvL) scatterplots. We focus the majority of the discussion in this subsection on the evolution of the BCC dislocation contents, as there are significant differences in defect accumulations compared to that of the bulk Nb.

At a first glance, the distribution of BCC dislocation types remains fairly similar to those observed in the bulk phase within the low dose range. However, we observe a secondary increase in the dislocation density when the damage level reaches approximately 0.428 dpa. As discussed later, this evolution is actually a feature of the complex interaction between defect accumulation and boundary morphology. For the quantitatively comparison of phase boundary effects, we plot the total BCC dislocation densities of the multilayers and bulk Nb in Fig. 6.6(c). In addition to confirming the ubiquitous appearance of the secondary increase in dislocation density, this plot also reveals a significant drop in initial dislocation density for the multilayered nanocomposite case. This, however, falls within the range of expectation, since the grain boundaries are known to act as sinks that absorb small sized defects.

Unlike those shown for BCC, the HCP dislocation densities in the Zr phase of the multilayered nanocomposite presented in Fig. 6.6(b) and Fig. 6.6(d) remain largely similar to that of the bulk Zr phase. The distributions of dislocation types in all three multilayers also do not deviate significantly from those in the bulk cases shown in Fig. 6.5(b). The only discernible effect of the phase boundaries is a slight decrease in the total dislocation densities. There is no counterpart to the secondary increase in dislocation density feature observed in the BCC phase.

It is important to note that there do exist a significant overlap in dislocation evolutions in

the Burgers and P-S OR multilayered nanocomposite configurations. This is perhaps a case against the effect of phase boundary microstructures, as the only difference between the two (0001)——(011) ORs is their stacking order. Conversely, the outlier nano-precipitate OR points to a significant dependence of defect accumulation on the bulk crystalline orientations.

Defect absorption by the phase boundary

To better illustrate the boundary absorption mechanism, we illustrate two early stages of defect accumulation in the Burgers OR multilayer in Fig. 6.7. Here, we primarily focus on the dislocation evolution in the BCC sub-lattice. We illustrate the initial stage of small dislocation loop accumulation corresponding to 0.0321 dpa in Fig. 6.7(a) and Fig. 6.7(b). At this dose level, the dislocation loops are all relatively small and evenly distributed throughout the bulk volumes, much like those observed in the bulk phase. Obvious deviations from the bulk behavior do not appear until the coalescence of larger dislocation loops, as shown in Fig. 6.7(c) and Fig. 6.7(d). At a damage level of 0.2247 dpa, we observe that large dislocation loops tend to form at the center of the bulk lattice, away from the interfaces. This is due to the cumulative effect of the boundary absorption mechanism. As dislocation loops continue to form with increasing dose, some of these dislocations migrate away from the phase boundaries coalesce and grow in size, while others migrate towards the phase boundaries and become trapped and absorbed. Over time, this process results not only in a decrease in the total defect content, but also in a position-dependent distribution of defect sizes.

Emergent defects near the phase boundary

While boundary absorption is very prevalent in the early stage of defect accumulation, it is quickly overshadowed by the emergence of a large quantity of dislocations near the phase boundary. It is important to note that these newly emerging BCC defects are not directly

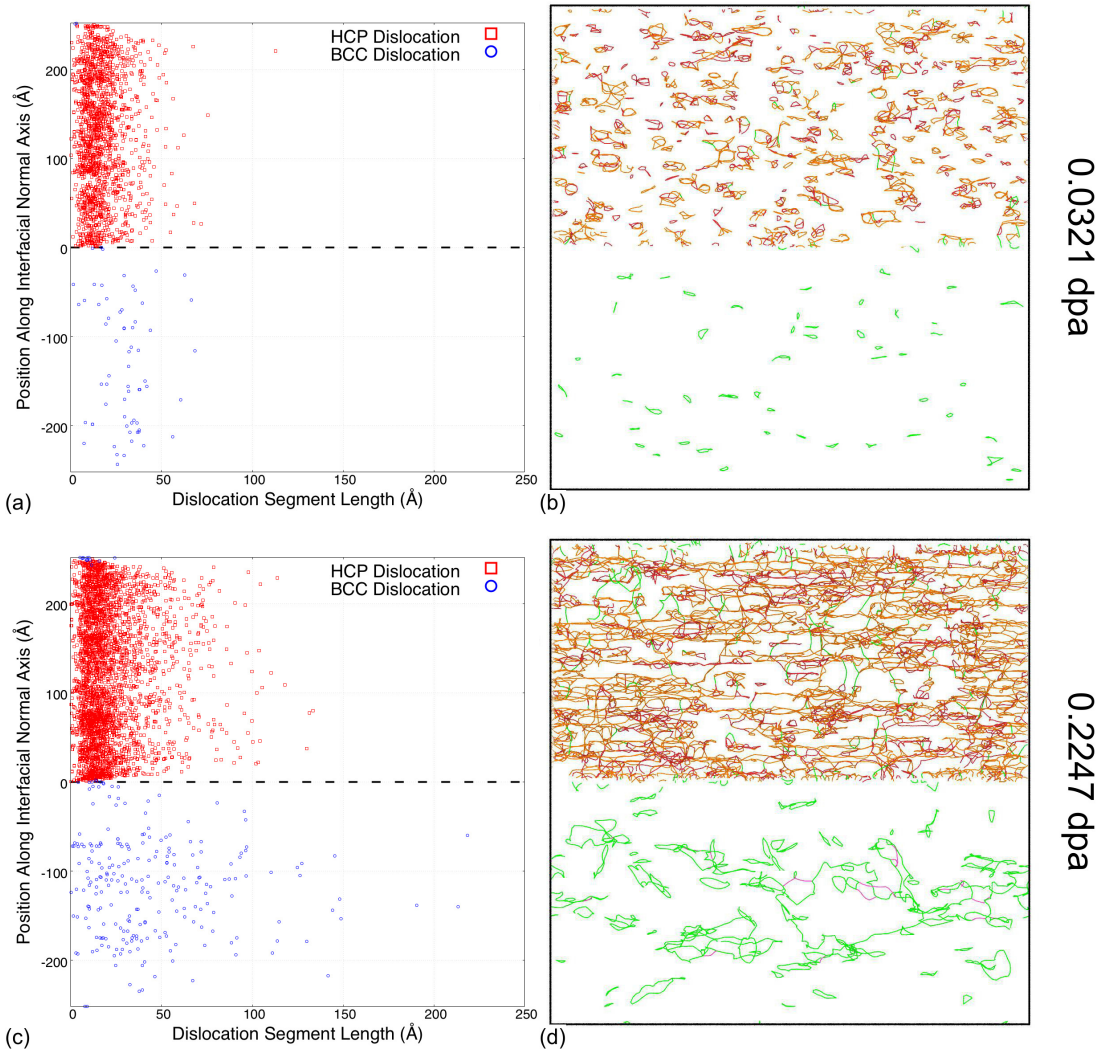

Figure 6.7: Early stages of dislocation evolution at the Burgers OR phase boundary. Scatterplots (a) and (c) correspond to the dislocation segment length location along the direction normal to the interface at a dose of 0.0321 dpa and 0.2247 dpa respectively. Figures (b) and (d) illustrate the distribution of dislocation loops in the vicinity of the Zr–Nb multilayer Burgers OR phase boundary at a dose of 0.0321 dpa and 0.2247 dpa respectively.

generated by the static boundaries. Rather, they are the byproduct of the change of the phase boundary morphology, in which the BCC lattice near the interface has shifted into HCP lattice [193]. This can be inferred from the PvL scatterplots at 0.3851 dpa (Fig. 6.8(a)) and 0.6419 dpa (Fig. 6.8(c)), in which the BCC dislocations (blue circle) not only grow in quantity, but also intrude into previously HCP positions. BCC dislocations emerging during this structural transformation are intrinsically small in size and form disjointed segments

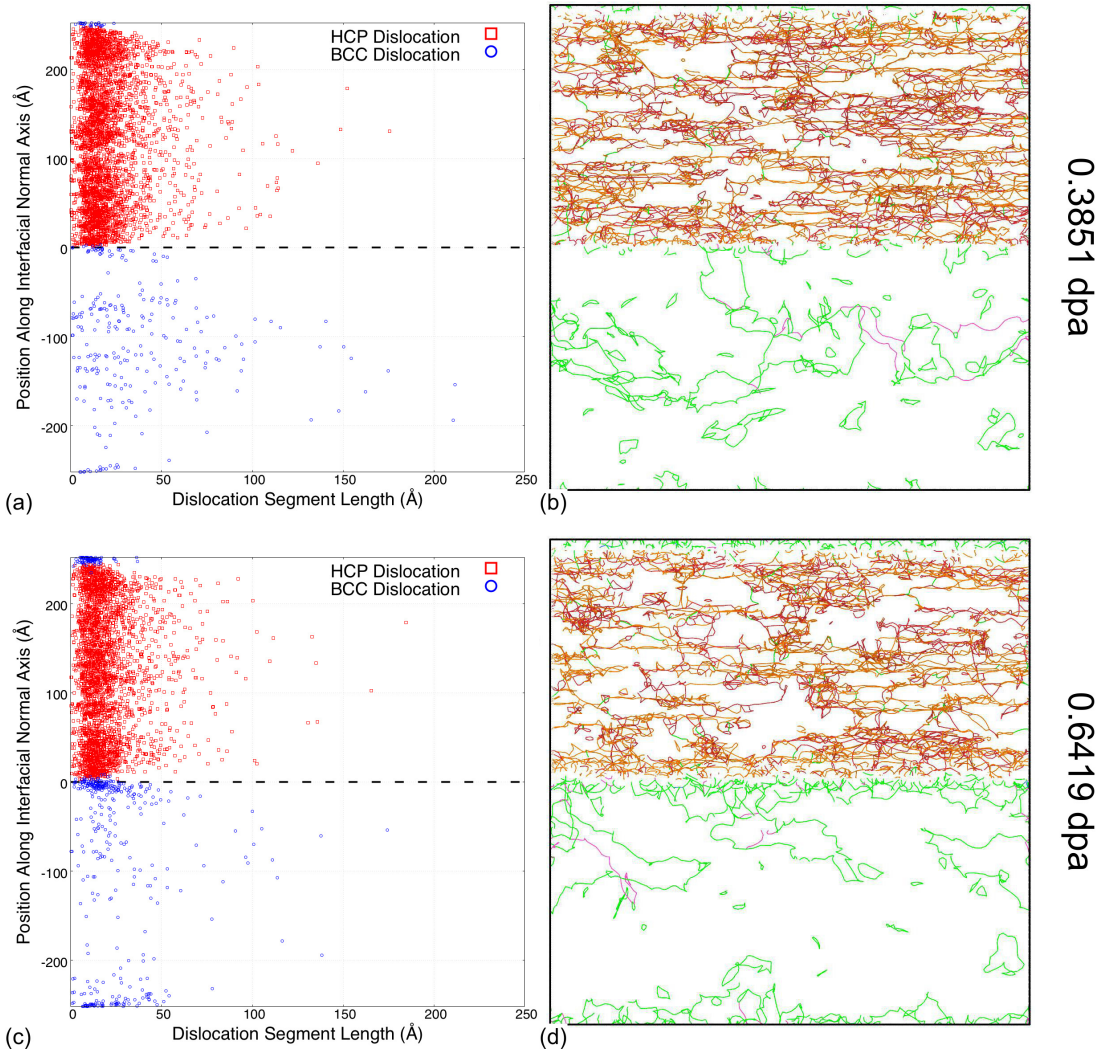

Figure 6.8: Intermediate and late stages of dislocation evolution at the Burgers OR phase boundary. (a) and (c) correspond to the dislocation segment length location along the direction normal to the interface at a dose of 0.3851 dpa and 0.6419 dpa respectively. (b) and (d) illustrate the distribution of dislocation loops in the vicinity of the Zr–Nb multilayer Burgers OR phase boundary at a dose of 0.3851 dpa and 0.6419 dpa respectively.

instead of complete loops. Due to both the attachment to the interfaces and the change in the Nb–Zr compositions, these new BCC dislocations are also less mobile than those of the Nb bulk phase. As a result, the nucleated boundary dislocation segments tend to form denser clusters instead of coalescing and reorganizing into larger dislocation loops. Indeed, these emergent dislocations are the cause of the secondary increase in BCC dislocation densities observed across all multilayers ORs. Finally, there are few early signs of larger

dislocations latching onto and becoming trapped at the boundaries, as shown in Fig. 6.8(c). The examination of such second order interaction between defect mechanisms, however, would need to be expanded upon in a separate study.

As expected, the inclusion of the effects of the morphological evolution of the phase boundary in the metallic multilayers has significantly changed the defect accumulation process. The interactions of multiple dislocation evolution mechanisms affect not only the quantity but also the intrinsic size-scale of resultant dislocations. The process of boundary emission does warrant more study at high doses, as there are some interesting engineering implications.

6.4 Discussions

6.4.1 Irradiation-induced Phase Transformation

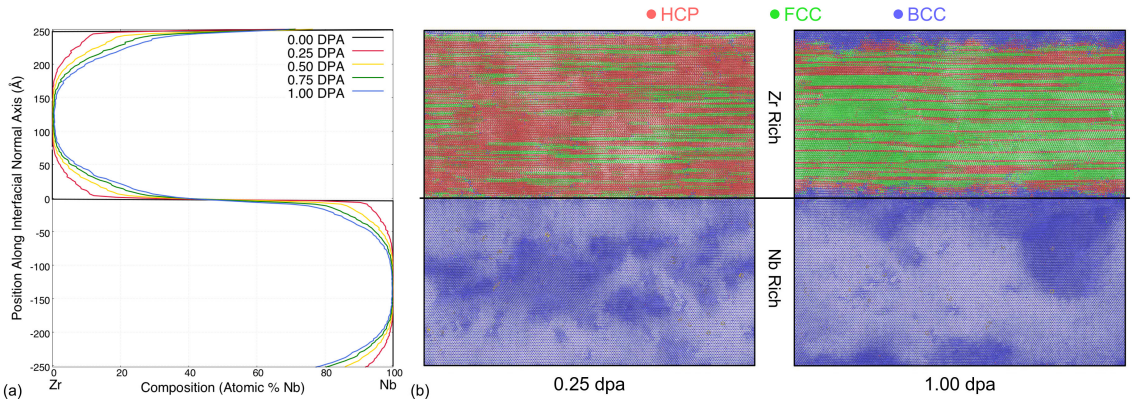

Figure 6.9: Intermixing and phase transformation at the Burgers OR phase boundary. (a) Atomic composition vs interfacial normal distance at various damage level. (b) Atomic structure types at 0.25 dpa and 1.0 dpa, as identified by Common Neighbor Analysis. *Note with the presence of defects in the system, distorted HCP structures are frequently identified as the similarly closed-packed FCC structure.

Given the established growth of a finite thickness BCC lattice structure into the HCP lattice and the role it plays in the management of defect concentration in the studied phase boundary systems, we turn our attention to understanding the mechanisms behind such a phase transformation. The two most common explanations are the defect induced instabil-

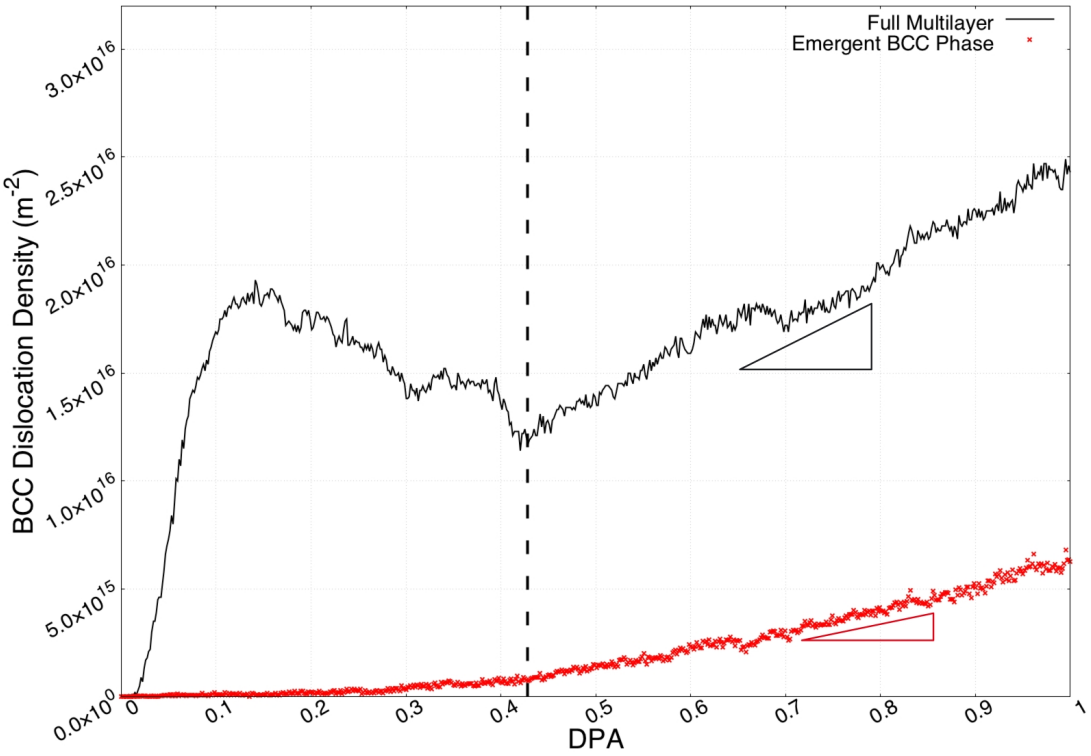

Figure 6.10: Dislocation density in the emergent BCC phase at the Burgers OR phase boundary. Emergent BCC phase is identified as volumes initially occupied by HCP structures at 0 dpa. Dislocation density growth rate in the full multilayer is greater than that in the emergent BCC phase.

ity and the boundary induced transformation [194]. Our simulations indicate that the cause of the HCP to BCC transformation is actually related to the irradiation-induced intermixing [195, 196, 52], a largely dose dependent process that occurs at phase boundaries. Using the Burgers OR phase boundary as an illustration, we illustrate in Fig. 6.9 the correlation between the intermixing and phase transformation phenomena.

In Fig. 6.9(a) we plot the atomic compositions of across the simulation cell at different stages of radiation damage. Starting from a pristine composition at 0 dpa, the original sharp interface becomes more and more diffused with increasing exposure to radiation damage. For the FPA modeling technique used in the present study, direct atom displacements most closely replicate the effects of ballistic mixing. As such, the evolution of the composi-

tion profile of Nb across the interface, $C_{\text{Nb}}(z,t)$, can be approximated by the functional form [12]:

$$C_{\text{Nb}}(z,t) = \frac{C'_{\text{Nb}}}{2}\left[1 - \text{erf}\left(\frac{z}{\sqrt{4Dt}}\right)\right], \tag{6.2}$$

where z is the distance normal to the interface plane, C'_{Nb} is the initial concentration of niobium in the Nb bulk (i.e., 100%), D is an effective diffusion coefficient, and t is the diffusion time. Additionally, when dealing with predominately ballistic mixing, the factor $4Dt$ becomes directly proportional to the dose ϕ (i.e., dpa), as shown by Nastasi et al. [197]. Therefore, the composition profile in Eq. 6.2 can also be expressed in terms of dose:

$$C_{\text{Nb}}(z,\phi) = \frac{C'_{\text{Nb}}}{2}\left[1 - \text{erf}\left(\frac{z}{\sqrt{\alpha \cdot \phi}}\right)\right], \tag{6.3}$$

where α is the proportionality constant. The functional form in Eq. 6.3 closely matches the intermixing evolution shown in Fig. 6.9(a).

As a result of the intermixing, composition changes can sometime trigger structural transformations in the crystalline lattices. This is especially prevalent near phase boundaries, where intermixing occurs most heavily. For phases with low miscibility, i.e., Cu–Nb [52], the intermixing has been shown to form growing layers of amorphous mixtures. Vice versa, for metals with high miscibility, the intermixing instead promotes alloying. In the case of Zr–Nb, the alloying process triggers the transformation from hexagon zirconium into a BCC Zr–Nb alloy phase [198]. This transformation process is also visible in Fig. 6.9(b), in which the BCC sub-lattice at 1.0 dpa grows far beyond the original location of the dividing interface when the interfacial intermixing has not occurred.

Since phase transformations occur exclusively in initially HCP sub-lattice, the newly formed (emergent) BCC phase can be easily identified by the position relative to the pristine phase boundaries, as illustrated in Fig. 6.9. Plotted in Fig. 6.10, is the dislocation density within this emergent BCC phase, representing the defects generated by the phase transformation process. The total BCC dislocations in the whole simulation volume is

shown alongside for reference. The dislocation density in the emergent BCC phase experiences very slow growth in the early stage, which is expected. Phase transformation requires both sufficient concentration and volume of mixing to be triggered. Comparing the two dislocation density evolutions, it is also clear that only a portion of the secondary increase in the total dislocation density is directly generated in the emergent BCC phase. The additional total dislocation density growth is attributed to the secondary interactions caused by the emergent defects, i.e. the increased boundary trapping of dislocations in the Nb-rich bulk.

Further examining the composition trigger of the phase transformations, we have tracked both the emergent point of the BCC dislocations and the fading point of the HCP dislocations to $\sim 20\%$ and $\sim 35\%$ Nb respectively. Within this composition range, the Zircaloy mixture has been observed to exist in both HCP and BCC phases. The variation in phase transformation rates between the various interface structures (Burgers, P-S and nano-precipitates) is attributed primarily to the differences in bulk lattice orientations rather than the interface structures themselves. This is evident in Fig. 6.6(c), in which the total BCC dislocation density for the nano-precipitate OR grows significantly slower than those at the Burgers and P-S ORs.

It is important to acknowledge that, while the morphology of Zr–Nb multilayers seems to favor phase transformation and emission of small dislocation loops, it cannot be accepted as a general rule. Boundary amorphization between immiscible metals can also be beneficial for defect management and reduce local stress. In either case, our results indicate that the defect-boundary interaction is not a steady-state process that can be examined in its isolated components. It is instead a larger dose dependent problem that needs to be investigated in its entirety.

6.4.2 Simulation Dose Rates

In order to replicate the defect accumulation and evolution process at atomistic timescale,

the simulated dose rates are accelerated far beyond what can be replicated experimentally. Consequently, this does result in the omission of some large timescale mechanisms, namely point defect diffusion. It is generally understood that defect diffusion is the mechanism by which defects interacts with grain boundaries. Due to the presence of long range elastic fields, mobile defects slowly diffuse towards to boundary defect sinks [35, 199] and eventually get absorbed [200]. The inability for the atomistic timescale to contain the diffusion process does restrict the defect boundary interaction at low dose/damage levels. Fortunately, small defects quickly cluster, grow in size and become immobile upon further irradiation, reducing the concern of diffusion over time. As a result, the dose and interfacial effects on defect evolution should remain largely unaffected by the dose rate, except the very early stages of point defect accumulation.

6.5 Conclusion

In this study, we have simulated the accumulation of irradiation defects in various orientation configurations of Zr–Nb multilayers. By using a novel technique based on the cumulative introduction of Frenkel pairs, we accelerated the simulations of irradiation processes faster than tradition collision cascade to study dose effects on defect evolutions near phase boundaries.

The process of the defect accumulation in bulk phases has been separated into three evolutionary stages: (i) accumulation, (ii) saturation, and (iii) coalescence. Each stage is associated with an intrinsic defect size and correlated with dislocation populations.

Expanding the study into multilayers heterophase boundaries, we also identified two additional defect accumulation mechanisms at these interfacial systems. Namely, we observed a boundary absorption mechanism early on, significantly restricting the accumulation of dislocations near the boundaries. As dose/damage buildup, the initial absorption is instead overtaken by the emission of large quantity immobile small size-scale dislocations. Our simulations enabled us to identify the emergent defects near the boundaries as

byproducts of the phase transformations caused by irradiation-induced intermixing. Interestingly, at any relevant damage level, the initial interfacial microstructures seem to have little influence on defect accumulation.

CHAPTER 7
IRRADIATION INDUCED EMBRITTLEMENT AT CU–NB PHASE BOUNDARIES

As the culmination of all previous works, this chapter finally examines the mechanical effects of radiation defect accumulation near phase boundaries. Utilizing the construction procedures outlined in Chapter 5, two pristine metallic multilayers are constructed by stacking layers of FCC Cu and BCC Nb. The bulk grains in the first multilayer are oriented to reproduce the Kurdjumov-Sachs (KS) orientation relationship at the interfaces, and the bulk grains in the second multilayer are oriented to reproduce the Nishiyama-Wassermann (NW) orientation relationship at the interfaces. Interfacial microstructures of the these orientation relationships have been previously studied by Wang et. al [201, 139], but they are shown to have little relevance after irradiation following Chapter 6. For simulation of large dose irradiation, we adapted the ROAC heavy ion bombardment example shown in Section 4.4.2. At regular dose intervals, the irradiated multilayer configurations are extracted and used to model phase boundry decoehsion. By comparing the crack growths and the crack tip dislocation emissions at multiple different doses, we are able to estimate the comparative mechanical effects of radiation defect accumulation.

To reduce the total number of illustrations, only results for the KS multiplayers are shown in the chapter below. Chapter 6 has already demonstrated the invariance of the defect accumulation behaviors with interfacial microstructures, This also holds true for the true for decohesion behaviors between two similarly oriented KS and NW multilayers.

7.1 Heavy-ion Irradiation of Multilayers

Similar to the example showcased in Section 4.4.2, heavy ion bombardment of bulk metals can be roughly approximated by utilizing a recoil spectrum for the PKA energies. For the

Cu–Nb multilayers considered, a second recoil energy spectrum for Nb is added (Fig. 7.1) to differentiate the radiation events in different bulk grains. Due concerns for cascade fragmentations at higher energies, both spectra also are only sampled up to the upper limit of 50 keV. At each 20 ps interval, 2,000 random radiation events of varying recoil energies are inserted into the multilayers. This process is repeated until the damage level, as estimated by the standard NRT-dpa model, reaches around 0.5 dpa. For each the irradiated multilayer configurations extract to model deochsion, radiation defect accumulation is shown in Fig. 7.2.

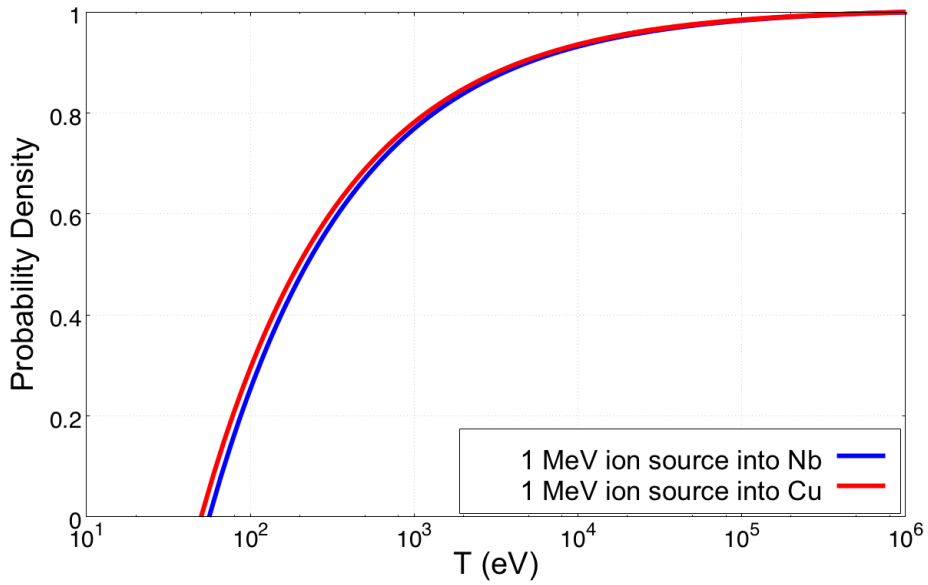

Figure 7.1: Integral primary recoil spectrum of 1 MeV ion sources irradiation Cu and Nb.

7.2 Intergranular Fracture at Irradiated Phase Boundaries

Using the approach proposed by Yamakov et al. [202, 203] for pure Aluminum, MD intergranular decohesion fracture models are constructed through a sequence of steps:

(1) Construction of a periodic grain boundary and optimization of the structure in isobaric-isothermal(NPT) ensemble, where $P = 0$.

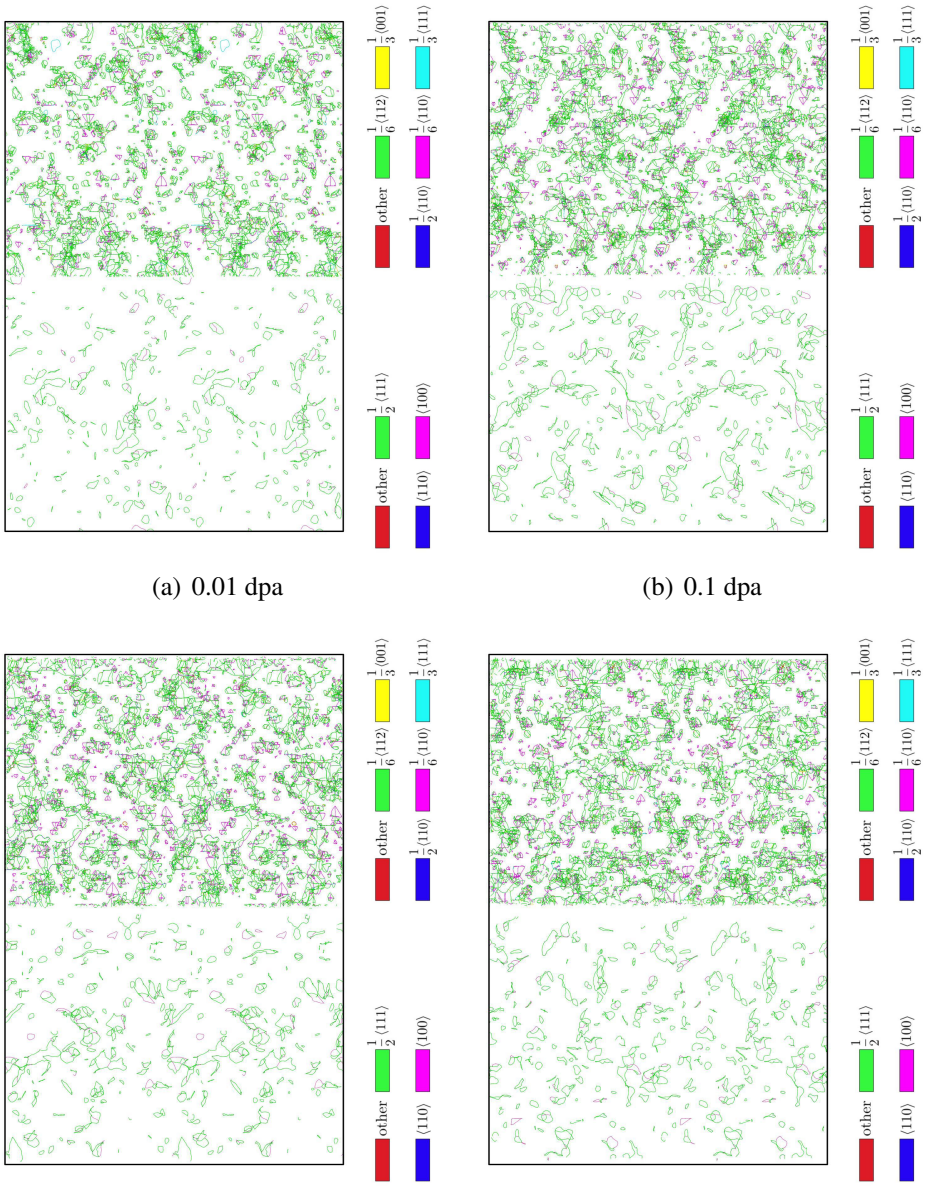

(a) 0.01 dpa

(b) 0.1 dpa

(c) 0.3 dpa

(d) 0.5 dpa

Figure 7.2: Dislocation evolution at the Cu–Nb phase boundary. (a) Dislocation content at 0.01 dpa. (b) Dislocation content at 0.1 dpa. (c) Dislocation content at 0.3 dpa. (d) Dislocation content at 0.5 dpa.

(2) Introduction of prestress in isobaric-isothermal(NPT) ensemble, where $P = \sigma_h$ is approximated by fracture stress σ_f in the Griffith fracture criterion [204] $\sigma_f\sqrt{a} = \sqrt{\frac{2E\gamma}{\pi}}$, where a is the half crack width, E is Young's moudulus, and γ is the free surface energy.

(3) Introduction of atomically sharp through crack of length $L_{crack} = 2a$, by screening particle interactions above and below the crack plane.

(4) Crack growth in isovolume-isothermal(NVT) ensemble, preserving the prestress.

This sequence effectively replicates a decreasing stress intensity loading condition at the atomic scale, allowing the study of steady state crack propagation.

In the present examination of radiation material aging, Step (1) is functionally replaced by the irradiated multilayer configurations for all cases except pristine fracture. To produce comparable decohesion behaviors, the loading condition in Step (2) and the initial crack designation in Step (3) are also kept constant across all doses of irradiation. Specifically, here we employed a hydrostatic tensile loading of $P = -7.5$ GPa, to induce deochsion with an initial crack size $2a = 200$ Å. This is in fact, slightly lower than then $P = -9.7$ GPa dictated by the Griffith fracture criterion, but it better accommodated the presence of radiation defects and preserved lattice stability during loading. For a demonstration of the pristine fracture characteristics, the final stable crack shape and crack tip dislocation emission are shown in Fig. 7.3.

While surprising, but not unexplained, Fig. 7.3(a) presents a heavily anisotropic behavior of crack growth. Instead of propagating along the Cu–Nb interface, crack tips quickly deflected away from the boundary, into the bulk Cu grain. This is attributed to the differences in elasticity between the two bulk grains/metals, which caused the softer Cu to take on the majority of the yielding. Similar behaviors were also observed in both simulations of Cu–SiC interfacial fracture [205], and experiments of Cu–Nb nano-laminates under shock loading [206]. In addition to deflect crack tips, the intergranular fracture also appears to be largely ductile in nature. The initially atomistically sharp crack tips are quickly blunted and expandeded into large plastics zones in the Cu bulk. Activation of slip systems ahead of the crack can be seen in Fig. 7.3(b), as dislocation emissions converge at the crack tips. Long range dislocation lines also emerged throughout the Cu grain, in order to better accommodate the large plastic deformations that have occurred during ductile fracture.

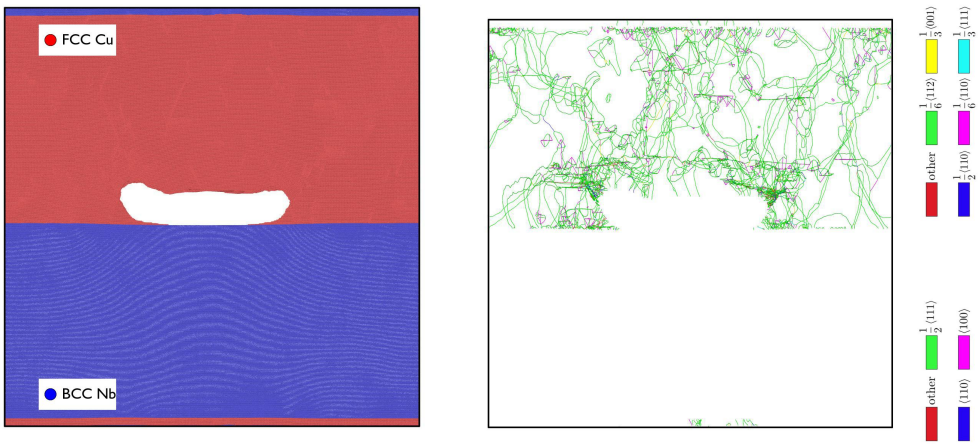

(a) (b)

Figure 7.3: Decohesion behavior at unirradiated Cu–Nb phase boundary. (a) Final stable crack shape. Crack tips are deflected towards to the FCC Cu bulk. (b) Dislocation emission due to crack propagation. No BCC dislocations are observed. *The unirradiated multilayer structure contains two additional alternating buffer layers to prevent dislocation transmission across the period boundary.

7.3 Integranular Fracture at Irradiated Phase Boundaries

Having established the baseline decohesion behaviors at the pristine phase boundary, we can now compare and extrapolate the effects of radiation defect accumulation by repeating the same analysis at dose. Shown in Fig. 7.4 are the individual decohesion behaviors at 0.01, 0.1, 0.3 and 0.5 dpa. For a more direct comparison crack growth characteristics, crack widths vs time and final stable crack shapes are also plotted in Fig. 7.5. It is important to note here, there are, indeed, a few small artificial differences between irradiated multilayers and pristine phase boundary used to model decohsion. They are taller in the crack normal direction, in order to eliminate any possible compositional mixing effects from the secondary phase boundary. They also do not contain alternating buffer layers, but the long range dislocations are mostly suppressed by existing defects, as we will later discuss in this section.

While not as obvious by examining individual decohesion behaviors, both comparative crack growth characteristics plotted n Fig. 7.5 clearly demonstrate a enlargement of crack

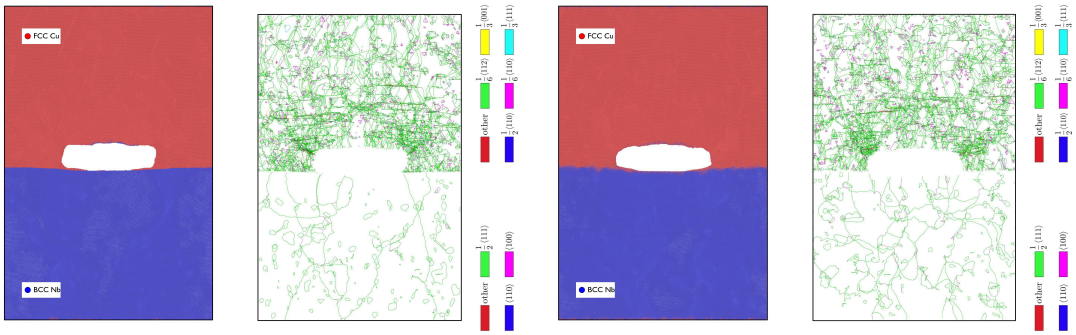

(a) 0.01 dpa (b) 0.01 dpa (c) 0.1 dpa (d) 0.01 dpa

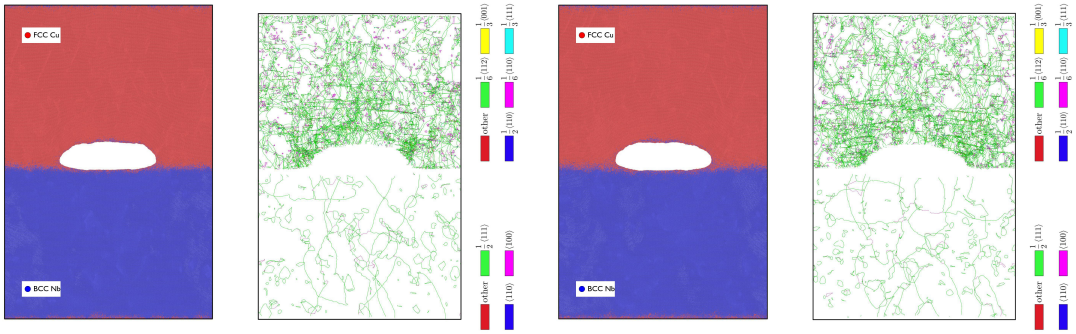

(e) 0.3 dpa (f) 0.3 dpa (g) 0.5 dpa (h) 0.5 dpa

Figure 7.4: Decohesion behavior at irradiated Cu–Nb phase boundary. (a), (b) Final stable crack shape and dislocation emission at 0.01 dpa. (c), (d) Final stable crack shape and dislocation emission at 0.1 dpa. (e), (f) Final stable crack shape and dislocation emission at 0.3 dpa. (g), (h) Final stable crack shape and dislocation emission at 0.5 dpa.

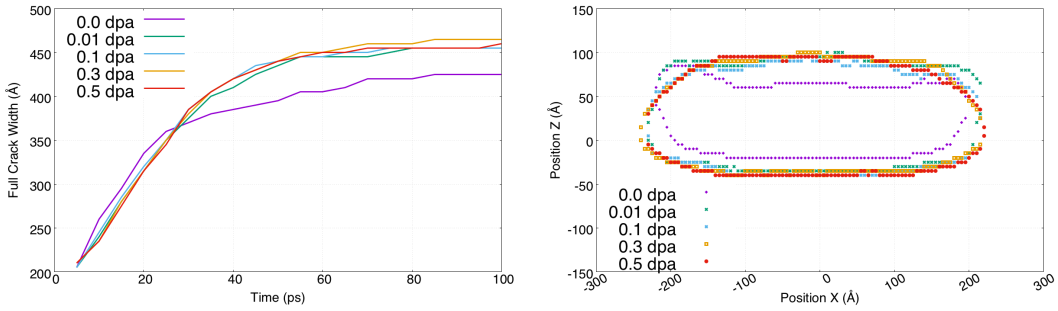

(a) (b)

Figure 7.5: Comparative decohesion behaviors at doses. (a) Crack widths as functions of time. (b) Final stable crack shapes after 100 ps.

sizes at dose. As loading condition remain constant throughout all models, this becomes equivalent to a reduction in plastic yielding in favor of crack extension. Of course, this loss

of ductility is, by definition, embrittlement, as induced by the accumulation of radiation defects. To a lesser extent, the effects of embrittlement can also be observed in the gradual evolution of final crack shapes from Fig 7.3(a), 7.4(a), 7.4(c), 7.4(e), and 7.4(g). As irradiation dose increases, both the crack tip deflection and the plastic deformation decrease, eventually leading to the flat planar crack shapes at 0.5 dpa.

In order to understand the mechanisms of radiation-induced embrittlement, we can examine the interactions between crack tip dislocation emissions and pre-existing radiation defects. While the long range dislocations can freely span across a pristine bulk crystal (Fig. 7.3(b)), interactions with existing defects can interrupt or redirect the path of transmission. As defect concentration increases, the likelihood of interaction increases, resulting in greater degrees of restriction to dislocations emitted from the crack tip. This localization of dislocation emissions only limits the plastic deformation across the larger grain but also elevates the comparative dislocation densities near emission sites. As such, the effects of embrittlement is often accompanied by an elevation of local dislocation density surrounding the crack opening, as illustrated by Fig.7.4(b), 7.4(d), 7.4(f), and 7.4(h).

CHAPTER 8
CONCLUSION

The central goal of this dissertation is to examine the mechanisms of the radiation aging of heterophase boundaries and the effects of aging on mechanical properties. In order to tackle this complex, multifaceted problem, multiple studies have been performed to examine the separate elements of radiation material aging.

In Chapter 3, we presented a study on the threshold displacement energies of metallic uranium [62] as an investigation into the initial stage of defect production. Utilizing standard collision cascade models, numerous simulations of atomic displacements have been simulated with varying recoil energies, recoil directions, lattice structures and ensemble temperatures. Subsequently, by analyzing the defect production of repeated cascades, statistical estimations for threshold displacement energy are then generated as functions of recoil direction and temperature. With respect to recoil directions, minima of threshold displacement energy are used to determine lattice channeling directions. With respect to temperature, variations of threshold displacement energy are used to determine the effects of thermally-enhanced recovery. Specifically for the orientation sampling of the anisotropic A20 α-U lattice, a new crystallographic symmetry-informed sample scheme was developed to eliminate potential bias. This new scheme is also generally applicable to other cubic, orthorhombic and tetragonal crystal lattice, which ultimately improves its viability for external applications.

Continuing with the investigation into the second stage of defect accumulation, Chapter 6 presented a study on the irradiation resistance of Zr–Nb metallic multilayers [115]. In place of standard collisions, the novel FPA method [58] is employed to simulate large-dose electron irradiation. The initial applications of FPA in bulk Zr and bulk Nb were used to establish a baseline characteristic for defect evolution at varying doses. Following the

bulk dislocation density evolution, the three stages of dislocation accumulation, saturation and coalescence were identified. Advancing through the stages, isolated dislocation loops gradually coalesce and grow in size, eventually forming large grain spanning dislocation forests. In a similar fashion, the FPA method is also applied to various Zr–Nb metallic multilayers to compare the effects of phase boundaries. While dislocation density evolution did indeed demonstrate a significant reduction in dislocation density at the early doses, as expected with boundary defect sinks, an unanticipated secondary rise in dislocation density also appeared well into the coalescence stage. The large emission of dislocations by the boundary is attributed to the cumulative composition mixing and the subsequent growth of a new composite Zr–Nb phase near the initial phase boundary. Ultimately, this study emphasized the importance of modeling defect accumulation and boundary morphology simultaneously, as both components can form a feedback loop that becomes less predictable overtime. As a supplement to this study, detailed analysis of many pristine U-Zr interfaces can be found in Chapter 5 [131]. However most of the work is effectively superfluous with respect to radiation damage, as there were no indications that initial grain boundary microstructures can withstand or influence defect accumulation at large doses.

Exploring the effects of radiation aging on mechanical properties, Chapter 7 presented a preliminary examination into Cu–Nb phase boundary decohesion behaviors at various doses of irradiation. The process of inducing boundary decohesion utilized an initial hydrostatic pressure loading, followed by the introduction of a nanocrack. This method was original proposed by Yamakov et. al [203] for the study of brittle grain boundary fracture, as it effectively constitutes a decreasing stress loading that would lead to steady-state crack growth. However, we found that crack extensions at the Cu–Nb phase boundaries are anything but brittle. Due to the large elastic anisotropy between Cu and Nb, cracks initiated at the phase boundaries quickly deflected toward the softer Cu bulk crystal. Growth of the cracks also do not follow any specific fracture plane, instead causing large plastic deformation ahead of the crack tip. This shift to ductile fracture behavior has unfortunately

rendered most quantitative analysis of decohesion behavior (i.e. Cohesive Zone Volume Element (CZVE) [202] and traction separate [**BW˙16**]) unusable. Qualitatively, we were able to demonstrate the early signs of embrittlement by comparing crack growth behaviors at various doses; however, there is still much to be done to develop a quantitative measure of the phase boundary embrittlement. As a continuation of the presented work, future efforts will be placed on quantitative analysis of ductile fracture behavior. While atomistic calculations of J-integral do exist [**JR˙10**], the applications are at best nontrivial, and are often restricted to the most idealized models. Quantitative assessment of crack tip plasticity would also more definitively confirm the existence of embrittlement as compared to basic analysis of crack open shapes.

Lastly, in order to supplement the study of large dose defect accumulation under realistic irradiation conditions, a new atomistic method of modeling damage accumulation was presented in Chapter 4. Utilizing an accelerated Monte Carlo framework, the new Reduced-Order Atomistic Cascade (ROAC) method generates radiation damage as reduced-order core-shells, with the core representing high energy thermal mixing, and the shell representing ballistic point defect production. Accuracy of the ROAC method is verified for both Cu and Nb by comparing the defects produced using this method against those produced using standard collision cascades for a wide range of recoil energies. Adaptations of ROAC have also been used to simulate large dose heavy ion bombardment in bulk Cu as well as irradiation of Cu–Nb multilayers. The scalability of this method means it will likely serve as a foundation for future investigations into radiation effects. One proposed future refinement of the method is the eventrual incorporation of high energy cascade fragmentation models, which would allow for the expansion of the applicable energy range to include the high energy neutron recoil spectrum. Such an improvement would greatly improve the flexibility of the method, and allow for true predictive modeling of reactor conditions.

REFERENCES

[1] A. Rascoe, "US approves first new nuclear plant in a generation," *Reuters technology*, vol. 9, 2012.

[2] B. Plumer, "Us nuclear comeback stalls as two reactors are abandoned," *The new york times*, Jul. 2017.

[3] P. Joskow and J. Parsons, "The future of nuclear power after fukushima," *Economics of energy & environmental policy*, vol. 1, no. 2, pp. 99–114, 2012.

[4] X. Guo and X. Guo, "Nuclear power development in china after the restart of new nuclear construction and approval: A system dynamics analysis," *Renewable and sustainable energy reviews*, vol. 57, pp. 999–1007, 2016.

[5] Z. Ming, L. Yingxin, O. Shaojie, S. Hui, and L. Chunxue, "Nuclear energy in the Post-Fukushima Era: Research on the developments of the Chinese and worldwide nuclear power industries," *Renewable and sustainable energy reviews*, vol. 58, pp. 147–156, 2016.

[6] C. Cawthorne and E. Fulton, "Voids in irradiated stainless steel," *Nature*, vol. 216, no. 5115, p. 575, 1967.

[7] E. Little and D. Stow, "Void-swelling in irons and ferritic steels: II. an experimental survey of materials irradiated in a fast reactor," *Journal of nuclear materials*, vol. 87, no. 1, pp. 25–39, 1979.

[8] L. Steele, "Neutron irradiation embrittlement of reactor pressure vessel steels," *International atomic energy agency (iaea)*, 1975.

[9] G. Odette and G. Lucas, "Embrittlement of nuclear reactor pressure vessels," *Jom*, vol. 53, no. 7, pp. 18–22, 2001.

[10] S. Bruemmer, E. Simonen, P. Scott, P. Andresen, G. Was, and J. Nelson, "Radiation-induced material changes and susceptibility to intergranular failure of light-water-reactor core internals," *Journal of nuclear materials*, vol. 274, no. 3, pp. 299–314, 1999.

[11] *Nuclear power reactors in the world*, ser. Reference Data Series 2. Vienna: INTERNATIONAL ATOMIC ENERGY AGENCY, 2019, ISBN: 978-92-0-102719-1.

[12] G. Was, *Fundamentals of radiation materials science: Metals and alloys*. Springer, 2016.

[13] M. Miller, M. Sokolov, R. Nanstad, and K. Russell, "APT characterization of high nickel RPV steels," *Journal of nuclear materials*, vol. 351, no. 1-3, pp. 187–196, 2006.

[14] C. Abromeit, "Aspects of simulation of neutron damage by ion irradiation," *Journal of nuclear materials*, vol. 216, pp. 78–96, 1994.

[15] P. Vladimirov and S. Bouffard, "Displacement damage and transmutations in metals under neutron and proton irradiation," *Comptes rendus physique*, vol. 9, no. 3-4, pp. 303–322, 2008.

[16] D. Maisonnier, I. Cook, S. Pierre, B. Lorenzo, L. Di Pace, G. Luciano, N. Prachai, P. Aldo, and P. Team, "DEMO and fusion power plant conceptual studies in Europe," *Fusion engineering and design*, vol. 81, no. 8-14, pp. 1123–1130, 2006.

[17] J. Knaster, F. Arbeiter, P. Cara, P. Favuzza, T. Furukawa, F. Groeschel, R. Heidinger, A. Ibarra, H. Matsumoto, A. Mosnier, H. Serizawa, M. Sugimoto, H. Suzuki, and E. Wakai, "IFMIF: Overview of the validation activities," *Nuclear fusion*, vol. 53, no. 11, p. 1 160 001, 2013.

[18] G. Kinchin and R. Pease, "The displacement of atoms in solids by radiation," *Reports on progress in physics*, vol. 18, no. 1, p. 1, 1955.

[19] M. Thompson, "Defects and radiation damage in metals," *Efects and radiation damage in metals, by mw thompson, cambridge, uk: Cambridge university press, 1974*, 1974.

[20] S. McRickard and J. Chow, "The effect of interstitial impurities on radiation hardening and embrittlement in iron," *Acta metallurgica*, vol. 14, no. 10, pp. 1195–1200, 1966.

[21] V. Tvergaard, "Material failure by void growth to coalescence," in *Advances in applied mechanics*, vol. 27, Elsevier, 1989, pp. 83–151.

[22] A. Dunn, L. Capolungo, E. Martinez, and M. Cherkaoui, "Spatially resolved stochastic cluster dynamics for radiation damage evolution in nanostructured metals," *Journal of nuclear materials*, vol. 443, no. 1-3, pp. 128–139, 2013.

[23] R. Barnes and D. Mazey, "The nature of radiation-induced point defect clusters," *Philosophical magazine*, vol. 5, no. 60, pp. 1247–1253, 1960.

[24] P. Derlet, D. Nguyen-Manh, and S. Dudarev, "Multiscale modeling of crowdion and vacancy defects in body-centered-cubic transition metals," *Physical review b*, vol. 76, no. 5, p. 054 107, 2007.

[25] B. Singh, H. Trinkaus, and C. Woo, "Production bias and cluster annihilation: Why necessary?" *Journal of nuclear materials*, vol. 212, pp. 168–174, 1994.

[26] U. Gösele and R. Mayer, "Nucleation and growth of voids by radiation: Iii. the role of sink strengths in the kinetics of swelling," *Journal of nuclear materials*, vol. 95, no. 1-2, pp. 64–74, 1980.

[27] K. Nogita and K. Une, "Radiation-induced microstructural change in high burnup UO2 fuel pellets," *Nuclear instruments and methods in physics research section b: Beam interactions with materials and atoms*, vol. 91, no. 1-4, pp. 301–306, 1994.

[28] K. Nordlund and F. Gao, "Formation of stacking-fault tetrahedra in collision cascades," *Applied physics letters*, vol. 74, no. 18, pp. 2720–2722, 1999.

[29] B. Wirth, V. Bulatov, and T. D. de la Rubia, "Atomistic simulation of stacking fault tetrahedra formation in Cu," *Journal of nuclear materials*, vol. 283, pp. 773–777, 2000.

[30] T. JŁssang and J. Hirth, "The energies of stacking-fault teirahedra in fcc metals," *Philosophical magazine*, vol. 13, no. 124, pp. 657–670, 1966.

[31] B. Uberuaga, L. Vernon, E. Martinez, and A. Voter, "The relationship between grain boundary structure, defect mobility, and grain boundary sink efficiency," *Scientific reports*, vol. 5, no. 9095, 2015.

[32] M. Samaras, P. Derlet, H. Van Swygenhoven, and M. Victoria, "Radiation damage near grain boundaries," *Philosophical magazine*, vol. 83, no. 31-34, pp. 3599–3607, 2003.

[33] F. Pérez and R. Smith, "Modelling radiation effects at grain boundaries in bcc iron," *Nuclear instruments and methods in physics research section b: Beam interactions with materials and atoms*, vol. 153, no. 1-4, pp. 136–141, 1999.

[34] P. Zarnas, R. Dingreville, and J. Qu, "Mechanics of point defect diffusion near dislocations and grain boundaries: A chemomechanical framework," *Computational materials science*, vol. 144, pp. 99–112, 2018.

[35] R. Balluffi, "High angle grain boundaries as sources or sinks for point defects," Massachusetts Inst. of Tech., Cambridge (USA). Dept. of Materials Science and Engineering, Tech. Rep., 1979.

[36] M. Shimada, H. Kokawa, Z. Wang, Y. Sato, and I. Karibe, "Optimization of grain boundary character distribution for intergranular corrosion resistant 304 stainless steel by twin-induced grain boundary engineering," *Acta materialia*, vol. 50, no. 9, pp. 2331–2341, 2002.

[37] T. Watanabe and S. Tsurekawa, "The control of brittleness and development of desirable mechanical properties in polycrystalline systems by grain boundary engineering," *Acta materialia*, vol. 47, no. 15-16, pp. 4171–4185, 1999.

[38] C. Basak, G. Prasad, H. Kamath, and N. Prabhu, "An evaluation of the properties of As-cast U-rich U–Zr alloys," *Journal of alloys and compounds*, vol. 480, no. 2, pp. 857–862, 2009.

[39] M. Yamaguchi, M. Shiga, and H. Kaburaki, "Grain boundary decohesion by impurity segregation in a nickel-sulfur system," *Science*, vol. 307, no. 5708, pp. 393–397, 2005.

[40] A. Cocks and M. Ashby, "On creep fracture by void growth," *Progress in materials science*, vol. 27, no. 3-4, pp. 189–244, 1982.

[41] A. Misra, M. Verdier, Y. Lu, H. Kung, T. Mitchell, M. Nastasi, and J. Embury, "Structure and mechanical properties of Cu-X (X= Nb, Cr, Ni) nanolayered composites," *Scripta materialia*, vol. 39, no. 4-5, pp. 555–560, 1998.

[42] H. Barshilia, A. Jain, and K. Rajam, "Structure, hardness and thermal stability of nanolayered tin/crn multilayer coatings," *Vacuum*, vol. 72, no. 3, pp. 241–248, 2003.

[43] M. Hu and A. Evans, "The cracking and decohesion of thin films on ductile substrates," *Acta metallurgica*, vol. 37, no. 3, pp. 917–925, 1989.

[44] W. Han, M. Demkowicz, N. Mara, E. Fu, S. Sinha, A. Rollett, Y. Wang, J. Carpenter, I. Beyerlein, and A. Misra, "Design of radiation tolerant materials via interface engineering," *Advanced materials*, vol. 25, no. 48, pp. 6975–6979, 2013.

[45] Y. Kim, J. Baek, S. Kim, S. Kim, S. Ryu, S. Jeon, and S. Han, "Radiation resistant vanadium-graphene nanolayered composite," *Scientific reports*, vol. 6, p. 24 785, 2016.

[46] J. Wang, Q. Zhou, S. Shao, and A. Misra, "Strength and plasticity of nanolaminated materials," *Materials research letters*, vol. 5, no. 1, pp. 1–19, 2017.

[47] R. Zhang, T. Germann, J. Wang, X.-Y. Liu, and I. Beyerlein, "Role of interface structure on the plastic response of cu/nb nanolaminates under shock compression:

Non-equilibrium molecular dynamics simulations," *Scripta materialia*, vol. 68, no. 2, pp. 114–117, 2013.

[48] K. Nordlund, S. Zinkle, A. Sand, F. Granberg, R. Averback, R. Stoller, T. Suzudo, L. Malerba, F. Banhart, W. Weber, F. Willaime, S. Dudarev, and D. Simeone, "Improving atomic displacement and replacement calculations with physically realistic damage models," *Nature communications*, vol. 9, no. 1, p. 1084, 2018.

[49] L. Zhang, E. Martinez, A. Caro, X.-Y. Liu, and M. Demkowicz, "Liquid-phase thermodynamics and structures in the Cu–Nb binary system," *Modelling and simulation in materials science and engineering*, vol. 21, no. 2, p. 025 005, 2013.

[50] J. Ziegler and J. Biersack, "The stopping and range of ions in matter," in *Treatise on heavy-ion science*, Springer, 1985, pp. 93–129.

[51] A. Sand, J. Dequeker, C. Becquart, C. Domain, and K. Nordlund, "Non-equilibrium properties of interatomic potentials in cascade simulations in tungsten," *Journal of nuclear materials*, vol. 470, pp. 119–127, 2016.

[52] L. Zhang and M. Demkowicz, "Radiation-induced mixing between metals of low solid solubility," *Acta materialia*, vol. 76, pp. 135–150, 2014.

[53] T. Lee, A. Caro, and M. Demkowicz, "Atomistic modeling of radiation-induced disordering and dissolution at a Ni/Ni3Al interface," *Journal of materials research*, vol. 30, no. 9, pp. 1456–1463, 2015.

[54] I. Jain and G. Agarwal, "Ion beam induced surface and interface engineering," *Surface science reports*, vol. 66, no. 3, pp. 77–172, 2011.

[55] G. Agarwal, P. Sharma, A. Jain, C. Lal, D. Kabiraj, and I. Jain, "Ion beam induced mixing at Co/Si interface," *Vacuum*, vol. 83, no. 2, pp. 397–400, 2008.

[56] G. Agarwal, V. Kulshrestha, P. Sharma, and I. Jain, "Change in the microstructure at W/Si interface and surface by swift heavy ions," *Journal of colloid and interface science*, vol. 351, no. 2, pp. 570–575, 2010.

[57] M. Kessels, J. Verhoeven, A. Yakshin, F. Tichelaar, and F. Bijkerk, "Ion beam induced intermixing of interface structures in W/Si multilayers," *Nuclear instruments and methods in physics research section b: Beam interactions with materials and atoms*, vol. 222, no. 3, pp. 484–490, 2004.

[58] A. Chartier, C. Onofri, L. Van Brutzel, C. Sabathier, O. Dorosh, and J. Jagielski, "Early stages of irradiation induced dislocations in urania," *Applied physics letters*, vol. 109, no. 18, p. 181 902, 2016.

[59] M. Norgett, M. Robinson, and I. Torrens, "A proposed method of calculating displacement dose rates," *Nuclear engineering and design*, vol. 33, no. 1, pp. 50–54, 1975.

[60] D. Chen, F. Gao, and B. Liu, "Grain boundary resistance to amorphization of nanocrystalline silicon carbide," *Scientific reports*, vol. 5, p. 16 602, 2015.

[61] A. Calder, D. Bacon, A. Barashev, and Y. Osetsky, "On the origin of large interstitial clusters in displacement cascades," *Philosophical magazine*, vol. 90, no. 7-8, pp. 863–884, 2010.

[62] E. Chen, C. Deo, and R. Dingreville, "Atomistic simulations of temperature and direction dependent threshold displacement energies in α-and γ-uranium," *Computational materials science*, vol. 157, pp. 75–86, 2019.

[63] M. Robinson and I. Torrens, "Computer simulation of atomic-displacement cascades in solids in the binary-collision approximation," *Physical review b*, vol. 9, no. 12, p. 5008, 1974.

[64] K. Nordlund, S. Zinkle, T. Suzudo, R. Averback, A. Meinander, F. Granberg, L. Malerba, R. Stoller, F. Banhart, W. Weber, F. Willaime, S. Dudarev, and D. Simeone, "Primary radiation damage in materials: Review of current understanding and proposed new standard displacement damage model to incorporate in-cascade mixing and defect production efficiency effects," Organisation for Economic Co-operation and Development, Nuclear Energy Agency, Report No. NEA-NSC-DOC-2015-9, 2015.

[65] J. Kittel, B. Frost, J. Mustelier, K. Bagley, G. Crittenden, and J. Van Dievoet, "History of fast reactor fuel development," *Journal of nuclear materials*, vol. 204, pp. 1–13, 1993.

[66] W. Carmack, D. Porter, Y. Chang, S. Hayes, M. Meyer, D. Burkes, C. Lee, T. Mizuno, F. Delage, and J. Somers, "Metallic fuels for advanced reactors," *Journal of nuclear materials*, vol. 392, no. 2, pp. 139–150, 2009.

[67] Y. Kim, G. Hofman, and A. Yacout, "Migration of minor actinides and lanthanides in fast reactor metallic fuel," *Journal of nuclear materials*, vol. 392, no. 2, pp. 164–170, 2009.

[68] M. Meyer, G. Hofman, S. Hayes, C. Clark, T. Wiencek, J. Snelgrove, R. Strain, and K. Kim, "Low-temperature irradiation behavior of uranium–molybdenum alloy dispersion fuel," *Journal of nuclear materials*, vol. 304, no. 2, pp. 221–236, 2002.

[69] G. Hofman, L. Walters, and T. Bauer, "Metallic fast reactor fuels," *Progress in nuclear energy*, vol. 31, no. 1-2, pp. 83–110, 1997.

[70] J. Smith and E. Kmetko, "Magnetism or bonding: A nearly periodic table of transition elements," *Journal of the less common metals*, vol. 90, no. 1, pp. 83–88, 1983.

[71] C. Barrett, M. Mueller, and R. Hitterman, "Crystal structure variations in alpha uranium at low temperatures," *Physical review*, vol. 129, no. 2, p. 625, 1963.

[72] G. Lander, E. Fisher, and S. Bader, "The solid-state properties of uranium. A historical perspective and review," *Advances in physics*, vol. 43, no. 1, pp. 1–111, 1994.

[73] A. Caro, M. Victoria, and R. Averback, "Threshold displacement and interstitial-atom formation energies in Ni_3Al," *Journal of materials research*, vol. 5, no. 7, pp. 1409–1413, 1990.

[74] B. Park, W. Weber, and L. Corrales, "Molecular-dynamics simulation study of threshold displacements and defect formation in zircon," *Physical review b*, vol. 64, no. 17, p. 174 108, 2001.

[75] L. Zepeda-Ruiz, S. Han, D. Srolovitz, R. Car, and B. Wirth, "Molecular dynamics study of the threshold displacement energy in vanadium," *Physical review b*, vol. 67, no. 13, p. 134 114, 2003.

[76] B. Thomas, N. Marks, L. Corrales, and R. Devanathan, "Threshold displacement energies in rutile TiO_2: A molecular dynamics simulation study," *Nuclear instruments and methods in physics research section b: Beam interactions with materials and atoms*, vol. 239, no. 3, pp. 191–201, 2005.

[77] K. Nordlund, J. Wallenius, and L. Malerba, "Molecular dynamics simulations of threshold displacement energies in Fe," *Nuclear instruments and methods in physics research section b: Beam interactions with materials and atoms*, vol. 246, no. 2, pp. 322–332, 2006.

[78] C. Taylor, "Evaluation of first-principles techniques for obtaining materials parameters of α-uranium and the (001) α-uranium surface," *Physical review b*, vol. 77, no. 9, p. 094 119, 2008.

[79] P. Moreira, R. Devanathan, J. Yu, and W. Weber, "Molecular-dynamics simulation of threshold displacement energies in zircon," *Nuclear instruments and methods in physics research section b: Beam interactions with materials and atoms*, vol. 267, no. 20, pp. 3431–3436, 2009.

[80] M. Jackson, P. Fossati, and R. Grimes, "Simulations of threshold displacement in beryllium," *Journal of applied physics*, vol. 120, no. 4, p. 045 903, 2016.

[81] M. Banisalman, S. Park, and T. Oda, "Evaluation of the threshold displacement energy in tungsten by molecular dynamics calculations," *Journal of nuclear materials*, vol. 495, no. Supplement C, pp. 277 –284, 2017.

[82] G. Kinchin and R. Pease, "The displacement of atoms in solids by radiation," *Reports on progress in physics*, vol. 18, no. 1, p. 1, 1955.

[83] R. Stoller, M. Toloczko, G. Was, A. Certain, S. Dwaraknath, and F. Garner, "On the use of SRIM for computing radiation damage exposure," *Nuclear instruments and methods in physics research section b: Beam interactions with materials and atoms*, vol. 310, pp. 75–80, 2013.

[84] F. Gao, D. Bacon, P. Flewitt, and T. Lewis, "A molecular dynamics study of temperature effects on defect production by displacement cascades in α-iron," *Journal of nuclear materials*, vol. 249, no. 1, pp. 77–86, 1997.

[85] B. Beeler, M. Asta, P. Hosemann, and N. Grønbech-Jensen, "Effect of strain and temperature on the threshold displacement energy in body-centered cubic iron," *Journal of nuclear materials*, vol. 474, pp. 113–119, 2016.

[86] D. Wang, N. Gao, Z. Wang, X. Gao, W. He, M. Cui, L. Pang, and Y. Zhu, "Effect of strain field on displacement cascade in tungsten studied by molecular dynamics simulation," *Nuclear instruments and methods in physics research section b: Beam interactions with materials and atoms*, vol. 384, pp. 68–75, 2016.

[87] F. Gao, D. Bacon, and G. Ackland, "Point-defect and threshold displacement energies in Ni_3Al I. Point-defect properties," *Philosophical magazine a*, vol. 67, no. 2, pp. 275–288, 1993.

[88] F. Gao and D. Bacon, "Point-defect and threshold displacement energies in Ni_3Al II. Events at the displacement threshold," *Philosophical magazine a*, vol. 67, no. 2, pp. 289–306, 1993.

[89] B. Beeler, Y. Zhang, M. Okuniewski, and C. Deo, "Calculation of the displacement energy of α and γ uranium," *Journal of nuclear materials*, vol. 508, pp. 181–194, 2018.

[90] B. Beeler, C. Deo, M. Baskes, and M. Okuniewski, "Atomistic properties of γ uranium," *Journal of physics: Condensed matter*, vol. 24, no. 7, p. 075 401, 2012.

[91] A. Moore, B. Beeler, C. Deo, M. Baskes, and M. Okuniewski, "Atomistic modeling of high temperature uranium-zirconium alloy structure and thermodynamics," *Journal of nuclear materials*, vol. 467, no. 2, pp. 802–819, 2015.

[92] D. Smirnova, A. Y. Kuksin, S. Starikov, and V. Stegailov, "Atomistic modeling of the self-diffusion in γ-u and γ-u-mo," *The physics of metals and metallography*, vol. 116, no. 5, pp. 445–455, 2015.

[93] S. Plimpton, "Fast parallel algorithms for short-range molecular dynamics," *Journal of computational physics*, vol. 117, no. 1, pp. 1–19, 1995.

[94] D. Smirnova, S. Starikov, and V. Stegailov, "Interatomic potential for uranium in a wide range of pressures and temperatures," *Journal of physics: Condensed matter*, vol. 24, no. 1, p. 015 702, 2011.

[95] ——, "New interatomic potential for computation of mechanical and thermodynamic properties of uranium in a wide range of pressures and temperatures," *The physics of metals and metallography*, vol. 113, no. 2, pp. 107–116, 2012.

[96] T. Schneider and E. Stoll, "Molecular-dynamics study of a three-dimensional one-component model for distortive phase transitions," *Physical review b*, vol. 17, no. 3, p. 1302, 1978.

[97] O. Engler and V. Randle, *Introduction to texture analysis: Macrotexture, microtexture, and orientation mapping*. CRC press, 2009.

[98] E. Weisstein, "Sphere point picking–from wolfram math world," *Wolfram research, inc*, 2013.

[99] K. Nordlund, M. Ghaly, R. Averback, M. Caturla, T. D. de La Rubia, and J. Tarus, "Defect production in collision cascades in elemental semiconductors and fcc metals," *Physical review b*, vol. 57, no. 13, p. 7556, 1998.

[100] A. Stukowski, "Visualization and analysis of atomistic simulation data with OVITO the Open Visualization Tool," *Modelling and simulation in materials science and engineering*, vol. 18, no. 1, p. 015 012, 2010.

[101] Y. Li, T. Shan, T. Liang, S. Sinnott, and S. Phillpot, "Classical interatomic potential for orthorhombic uranium," *Journal of physics: Condensed matter*, vol. 24, no. 23, p. 235 403, 2012.

[102] B. Beeler, B. Good, S. Rashkeev, C. Deo, M. Baskes, and M. Okuniewski, "First-principles calculations of the stability and incorporation of helium, xenon and krypton in uranium," *Journal of nuclear materials*, vol. 425, no. 1-3, pp. 2–7, 2012.

[103] G. Huang and B. Wirth, "First-principles study of bubble nucleation and growth behaviors in α U–Zr," *Journal of physics: Condensed matter*, vol. 24, no. 41, p. 415 404, 2012.

[104] B. Beeler, B. Good, S. Rashkeev, C. Deo, M. Baskes, and M. Okuniewski, "First principles calculations for defects in U," *Journal of physics: Condensed matter*, vol. 22, no. 50, p. 505 703, 2010.

[105] D. Simeone, L. Luneville, and Y. Serruys, "Cascade fragmentation under ion beam irradiation: A fractal approach," *Physical review e*, vol. 82, no. 1, p. 011 122, 2010.

[106] L. Bukonte, F. Djurabekova, J. Samela, K. Nordlund, S. Norris, and M. Aziz, "Comparison of molecular dynamics and binary collision approximation simulations for atom displacement analysis," *Nuclear instruments and methods in physics research b*, vol. 297, pp. 23–28, 2013.

[107] A. Sand, D. Mason, A. De Backer, X. Yi, S. Dudarev, and K. Nordlund, "Cascade fragmentation: Deviation from power law in primary radiation damage," *Materials research letters*, vol. 5, no. 5, pp. 357–363, 2017.

[108] J. Stewart, A. Kohnert, L. Capolungo, and R. Dingreville, "Design and analysis of forward and reverse models for predicting defect accumulation, defect energetics, and irradiation conditions," *Computational materials science*, vol. 148, pp. 272–285, 2018.

[109] Q. Peng, F. Meng, Y. Yang, C. Lu, H. Deng, L. Wang, S. De, and F. Gao, "Shockwave generates ¡100¿ dislocation loops in bcc iron," *Nature communications*, vol. 9, no. 1, p. 4880, 2018.

[110] J.-P. Crocombette, "Cell Molecular Dynamics for Cascade (CMDC): Molecular dynamics simulation of cascades for realistic ion energies," *Computational materials science*, vol. 147, pp. 168–175, 2018.

[111] M. Baskes, "Modified embedded-atom potentials for cubic materials and impurities," *Physical review b*, vol. 46, no. 5, p. 2727, 1992.

[112] T.-R. Shan, B. Devine, T. Kemper, S. Sinnott, and S. Phillpot, "Charge-optimized many-body potential for the hafnium/hafnium oxide system," *Physical review b*, vol. 81, no. 12, p. 125 328, 2010.

[113] K. Chenoweth, A. van Duin, and W. Goddard, "ReaxFF reactive force field for molecular dynamics simulations of hydrocarbon oxidation," *The journal of physical chemistry a*, vol. 112, no. 5, pp. 1040–1053, 2008.

[114] J.-P. Crocombette, A. Chartier, and W. Weber, "Atomistic simulation of amorphization thermokinetics in lanthanum pyrozirconate," *Applied physics letters*, vol. 88, no. 5, p. 051 912, 2006.

[115] E. Chen, C. Deo, and R. Dingreville, "Irradiation resistance of nanostructured interfaces in Zr–Nb metallic multilayers," *Journal of materials research*, pp. 1–13, 2019.

[116] A. Sand, J. Byggmästar, A. Zitting, and K. Nordlund, "Defect structures and statistics in overlapping cascade damage in fusion-relevant bcc metals," *Journal of nuclear materials*, vol. 511, pp. 64–74, 2018.

[117] D. Bacon, F. Gao, and Y. Osetsky, "The primary damage state in fcc, bcc and hcp metals as seen in molecular dynamics simulations," *Journal of nuclear materials*, vol. 276, no. 1-3, pp. 1–12, 2000.

[118] C. Björkas and K. Nordlund, "Comparative study of cascade damage in Fe simulated with recent potentials," *Nuclear instruments and methods in physics research b*, vol. 259, no. 2, pp. 853–860, 2007.

[119] A. Sand and K. Nordlund, "On the lower energy limit of electronic stopping in simulated collision cascades in Ni, Pd and Pt," *Journal of nuclear materials*, vol. 456, pp. 99–105, 2015.

[120] A. Meldrum, S. Zinkle, L. Boatner, and R. C. Ewing, "A transient liquid-like phase in the displacement cascades of zircon, hafnon and thorite," *Nature*, vol. 395, no. 6697, p. 56, 1998.

[121] N. Li, K. Hattar, and A. Misra, "In situ probing of the evolution of irradiation-induced defects in copper," *Journal of nuclear materials*, vol. 439, no. 1-3, pp. 185–191, 2013.

[122] A. De Backer, C. Domain, C. Becquart, L. Luneville, D. Simeone, A. E. Sand, and K. Nordlund, "A model of defect cluster creation in fragmented cascades in metals based on morphological analysis," *Journal of physics: Condensed matter*, vol. 30, no. 40, p. 405 701, 2018.

[123] H. Heinisch and B. Singh, "On the structure of irradiation-induced collision cascades in metals as a function of recoil energy and crystal structure," *Philosophical magazine a*, vol. 67, no. 2, pp. 407–424, 1993.

[124] S. Jumel and J. Van-Duysen, "INCAS: An analytical model to describe displacement cascades," *Journal of nuclear materials*, vol. 328, no. 2-3, pp. 151–164, 2004.

[125] A. Ryazanov, E. Metelkin, and E. Semenov, "Modeling of cascade and sub-cascade formation at high PKA energies in irradiated fusion structural materials," *Journal of nuclear materials*, vol. 386, pp. 132–134, 2009.

[126] A. Sand, S. Dudarev, and K. Nordlund, "High-energy collision cascades in tungsten: Dislocation loops structure and clustering scaling laws," *Epl (europhysics letters)*, vol. 103, no. 4, p. 46 003, 2013.

[127] R. Averback, "Atomic displacement processes in irradiated metals," *Journal of nuclear materials*, vol. 216, pp. 49–62, 1994.

[128] M. Makin, A. Whapham, and F. Minter, "The formation of dislocation loops in copper during neutron irradiation," *Philosophical magazine*, vol. 7, no. 74, pp. 285–299, 1962.

[129] M. Victoria, N. Baluc, C. Bailat, Y. Dai, M. Luppo, R. Schaublin, and B. Singh, "The microstructure and associated tensile properties of irradiated fcc and bcc metals," *Journal of nuclear materials*, vol. 276, no. 1-3, pp. 114–122, 2000.

[130] A. Dunn, R. Dingreville, and R. Capolungo, "Multi-scale simulation of radiation damage accumulation and subsequent hardening in neutron-irradiated α-Fe," *Modelling and simulation in materials science and engineering*, vol. 24, p. 015 005, 2016.

[131] E. Chen, R. Dingreville, and C. Deo, "Misfit dislocation networks in semi-coherent miscible phase boundaries: An example for u–zr interfaces," *Computational materials science*, vol. 154, pp. 194–203, 2018.

[132] P. Gumbsch, M. Daw, S. Foiles, and H. Fischmeister, "Accommodation of the lattice mismatch in a Ag/Ni heterophase boundary," *Physical review b*, vol. 43, no. 17, p. 13 833, 1991.

[133] R. Maurer and H. Fischmeister, "Low energy heterophase boundaries in the system silver/nickel and in other weakly bonded systems," *Acta metallurgica*, vol. 37, no. 4, pp. 1177–1189, 1989.

[134] A. Romanov, T. Wagner, and M. Rühle, "Coherent to incoherent transition in mismatched interfaces," *Scripta materialia*, vol. 38, no. 6, pp. 869–875, 1998.

[135] A. Romanov and T. Wagner, "On the universal misfit parameter at mismatched interfaces," *Scripta materialia*, vol. 45, no. 3, pp. 325–331, 2001.

[136] R. Hyland, M. Asta, S. Foiles, and C. Rohrer, "Al(fcc):$Al_3Sc(L1_2)$ interphase boundary energy calculations," *Acta materialia*, vol. 46, no. 10, pp. 3667–3678, 1998.

[137] M. Asta and J. Hoyt, "Thermodynamic properties of coherent interfaces in fcc-based Ag–Al alloys: A first-principles study," *Acta materialia*, vol. 48, no. 5, pp. 1089–1096, 2000.

[138] J. Wang and A. Misra, "An overview of interface-dominated deformation mechanisms in metallic multilayers," *Current opinion in solid state and materials science*, vol. 15, no. 1, pp. 20–28, 2011.

[139] J. Wang, R. Zhang, C. Zhou, I. Beyerlein, and A. Misra, "Interface dislocation patterns and dislocation nucleation in face-centered-cubic and body-centered-cubic bicrystal interfaces," *International journal of plasticity*, vol. 53, pp. 40–55, 2014.

[140] Y. Chen, S. Shao, X. Liu, S. Yadav, N. Li, N. Mara, and J. Wang, "Misfit dislocation patterns of mg-nb interfaces," *Acta materialia*, vol. 126, pp. 552–563, 2017.

[141] M. Demkowicz and L. Thilly, "Structure, shear resistance and interaction with point defects of interfaces in Cu–Nb nanocomposites synthesized by severe plastic deformation," *Acta materialia*, vol. 59, no. 20, pp. 7744–7756, 2011.

[142] B. Bilby, "On the interactions of dislocations and solute atoms," *Proceedings of the physical society. section a*, vol. 63, no. 3, p. 191, 1950.

[143] F. Frank, "LXXXIII. Crystal dislocations – Elementary concepts and definitions," *The london, edinburgh, and dublin philosophical magazine and journal of science*, vol. 42, no. 331, pp. 809–819, 1951.

[144] J. Hirth, R. Pond, R. Hoagland, X. Liu, and J. Wang, "Interface defects, reference spaces and the Frank–Bilby equation," *Progress in materials science*, vol. 58, no. 5, pp. 749–823, 2013.

[145] A. Vattré and M. Demkowicz, "Partitioning of elastic distortions at a semicoherent heterophase interface between anisotropic crystals," *Acta materialia*, vol. 82, pp. 234–243, 2015.

[146] A. Vattré, "Elastic strain relaxation in interfacial dislocation patterns: I. A parametric energy-based framework," *Journal of the mechanics and physics of solids*, vol. 105, pp. 254–282, 2017.

[147] G. Pilania, B. Thijsse, R. Hoagland, I. Lazia, S. Valone, and X. Liu, "Revisiting the Al/Al_2O_3 interface: Coherent interfaces and misfit accommodation," *Scientific reports*, vol. 4, 2014.

[148] M. Demkowicz, R. Hoagland, and J. Hirth, "Interface structure and radiation damage resistance in Cu-Nb multilayer nanocomposites," *Physical review letters*, vol. 100, no. 13, p. 136 102, 2008.

[149] A. Stukowski, V. Bulatov, and A. Arsenlis, "Automated identification and indexing of dislocations in crystal interfaces," *Modelling and simulation in materials science and engineering*, vol. 20, no. 8, p. 085 007, 2012.

[150] L. Smith and D. Farkas, "Non-planar grain boundary structures in fcc metals and their role in nano-scale deformation mechanisms," *Philosophical magazine*, vol. 94, no. 2, pp. 152–173, 2014.

[151] J. Jeon and G. Dehm, "Formation of dislocation networks in a coherent cu $\Sigma 3$ (1 1 1) twin boundary," *Scripta materialia*, vol. 102, pp. 71–74, 2015.

[152] Y. Gao, P. Shewmon, and S. Dregia, "Investigation of low energy interphase boundaries in AgNi by computer simulation and crystallite rotation," *Acta metallurgica*, vol. 37, no. 12, pp. 3165–3175, 1989.

[153] S. Kaity, J. Banerjee, M. Nair, K. Ravi, S. Dash, T. Kutty, A. Kumar, and R. Singh, "Microstructural and thermophysical properties of U–6 wt.% Zr alloy for fast reactor application," *Journal of nuclear materials*, vol. 427, no. 1-3, pp. 1–11, 2012.

[154] J. Kim, H. Song, H. Kim, K. Kim, C. Lee, and R. Fielding, "Development of a new casting method to fabricate U–Zr alloy containing minor actinides," *Journal of radioanalytical and nuclear chemistry*, vol. 299, no. 1, pp. 103–109, 2014.

[155] A. Moore, C. Deo, M. Baskes, and M. Okuniewski, "Atomistic mechanisms of morphological evolution and segregation in U-Zr alloys," *Acta materialia*, vol. 115, pp. 178–188, 2016.

[156] C. Yoo, H. Cynn, and P. Söderlind, "Phase diagram of uranium at high pressures and temperatures," *Physical review b*, vol. 57, no. 17, p. 10 359, 1998.

[157] A. Heiming, W. Petry, J. Trampenau, M. Alba, C. Herzig, H. Schober, and G. Vogl, "Phonon dispersion of the bcc phase of group-IV metals. II. bcc zirconium, a model case of dynamical precursors of martensitic transitions," *Physical review b*, vol. 43, no. 13, p. 10 948, 1991.

[158] R. Dingreville, A. Hallil, and S. Berbenni, "From coherent to incoherent mismatched interfaces: A generalized continuum formulation of surface stresses," *Journal of the mechanics and physics of solids*, vol. 72, pp. 40–60, 2014.

[159] M. Duesbery and V. Vitek, "Plastic anisotropy in b.c.c. transition metals," *Acta materialia*, vol. 46, no. 5, pp. 1481–1492, 1998.

[160] J. Yang, Y. Nagai, Z. Yang, and M. Hasegawa, "Quantization of the Frank-Bilby equation for misfit dislocation arrays in interfaces," *Acta materialia*, vol. 57, no. 16, pp. 4874–4881, 2009.

[161] A. Sangghaleh and M. Demkowicz, "AIDA: A tool for exhaustive enumeration of solutions to the quantized Frank-Bilby equation," *Computational materials science*, vol. 145, pp. 35–47, 2018.

[162] W. Bollmann, *Crystal defects and crystalline interfaces*. Springer-Verlag Berlin Heidelberg, 1970.

[163] R. Dingreville and J. Qu, "Interfacial excess energy, excess stress and excess strain in elastic solids: Planar interfaces," *Journal of the mechanics and physics of solids*, vol. 56, no. 5, pp. 1944–1954, 2008.

[164] F. Larché and J. W. Cahn, "A linear theory of thermochemical equilibrium of solids under stress," *Acta metallurgica*, vol. 21, no. 8, pp. 1051–1063, 1973.

[165] F. Larché and J. Cahn, "Thermochemical equilibrium of multiphase solids under stress," *Acta metallurgica*, vol. 26, no. 10, pp. 1579–1589, 1978.

[166] J. Cahn and F. Larché, "A simple model for coherent equilibrium," *Acta metallurgica*, vol. 32, no. 11, pp. 1915–1923, 1984.

[167] X. Zhang, K. Hattar, Y. Chen, L. Shao, J. Li, C. Sun, K. Yu, N. Li, M. Taheri, H. Wang, J. Wang, and M. Nastasi, "Radiation damage in nanostructured materials," *Progress in materials science*, 2018.

[168] M. Rose, A. Balogh, and H. Hahn, "Instability of irradiation induced defects in nanostructured materials," *Nuclear instruments and methods in physics research section b: Beam interactions with materials and atoms*, vol. 127, pp. 119–122, 1997.

[169] B. Radiguet, A. Etienne, P. Pareige, X. Sauvage, and R. Valiev, "Irradiation behavior of nanostructured 316 austenitic stainless steel," *Journal of materials science*, vol. 43, pp. 7338–7343, 2008.

[170] M. Demkowicz, O. Anderoglu, X. Zhang, and A. Misra, "The influence of $\Sigma 3$ twin boundaries on the formation of radiation-induced defect clusters in nanotwinned Cu," *Journal of materials research*, vol. 26, pp. 1666–1675, 2011.

[171] J. Li, K. Yu, Y. Chen, M. Song, H. Wang, M. Kirk, M. Li, and X. Zhang, "In situ study of defect migration kinetics and self-healing of twin boundaries in heavy ion irradiated nanotwinned metals," *Nanoletters*, vol. 15, pp. 2922–2927, 2015.

[172] F. Chen, X. Tang, Y. Yang, H. Huang, J. Liu, H. Li, and D. Chen, "Atomic simulations of Fe/Ni multilayer nanocomposites on the radiation damage resistance," *Journal of nuclear materials*, vol. 468, pp. 164–170, 2016.

[173] C. Sun, D. Bufford, Y. Chen, M. Kirk, Y. Wang, M. Li, H. Wang, S. Maloy, and X. Zhang, "In situ study of defect migration kinetics in nanoporous Ag with enhanced radiation tolerance," *Scientific reports*, vol. 4, no. 1, p. 3737, 2014.

[174] J. Li, C. Fan, J. Ding, S. Xue, Y. Chen, Q. Li, H. Wang, and X. Zhang, "In situ heavy ion irradiation studies of nanopore shrinkage and enhanced radiation tolerance of nanoporous Au," *Scientific reports*, vol. 7, p. 39 484, 2017.

[175] I. Beyerlein, J. Mayeur, S. Zheng, N. Mara, J. Wang, and A. Misra, "Emergence of stable interfaces under extreme plastic deformation," *Proceedings of the national academy of sciences*, p. 201 319 436, 2014.

[176] I. Beyerlein, M. Demkowicz, A. Misra, and B. Uberuaga, "Defect-interface interactions," *Progress in materials science*, vol. 74, pp. 125–210, 2015.

[177] A. Vattré, T. Jourdan, H. Ding, M. Marinica, and M. Demkowicz, "Non-random walk diffusion enhances the sink strength of semicoherent interfaces," *International journal of plasticity*, vol. 7, 2016.

[178] H. Heinisch, F. Gao, and R. Kurtz, "The effects of interfaces on radiation damage production in layered metal composites," *Journal of nuclear materials*, vol. 329, pp. 924–928, 2004.

[179] L. Zhang and M. Demkowicz, "Morphological stability of Cu-Nb nanocomposites under high-energy collision cascades," *Applied physics letters*, vol. 103, no. 6, p. 061 604, 2013.

[180] A. Nikulina, "Zirconium-niobium alloys for core elements of pressurized water reactors," *Metal science and heat treatment*, vol. 45, no. 7-8, pp. 287–292, 2003.

[181] W. Burgers, "On the process of transition of the cubic-body-centered modification into the hexagonal-close-packed modification of zirconium," *Physica*, vol. 1, no. 7-12, pp. 561–586, 1934.

[182] W. Pitsch and A. Schrader, "Die Ausscheidungsform des ϵ-Karbids im Ferrit und im Martensit beim Anlassen," *Archiv für das eisenhüttenwesen*, vol. 29, no. 11, pp. 715–721, 1958.

[183] J. Ribis, S. Doriot, and F. Onimus, "Shape, orientation relationships and interface structure of beta-Nb nano-particles in neutron irradiated zirconium alloy," *Journal of nuclear materials*, vol. 511, pp. 18–29, 2018.

[184] D. Smirnova and S. Starikov, "An interatomic potential for simulation of Zr-Nb system," *Computational materials science*, vol. 129, pp. 259–272, 2017.

[185] H. Balboa, L. Van Brutzel, A. Chartier, and Y. Le Bouar, "Damage characterization of (U, Pu) O under irradiation by molecular dynamics simulations," *Journal of nuclear materials*, 2018.

[186] J. Ziegler, M. Ziegler, and J. Biersack, "SRIM–The stopping and range of ions in matter (2010)," *Nuclear instruments and methods in physics research section b: Beam interactions with materials and atoms*, vol. 268, no. 11-12, pp. 1818–1823, 2010.

[187] A. Jostsons and K. Farrell, "Structural damage and its annealing response in neutron irradiated magnesium," *Radiation effects*, vol. 15, no. 3-4, pp. 217–225, 1972.

[188] M. Griffiths, "Evolution of microstructure in hcp metals during irradiation," *Journal of nuclear materials*, vol. 205, pp. 225–241, 1993.

[189] D. Northwood, R. Gilbert, L. Bahen, P. Kelly, R. Blake, A. Jostsons, P. Madden, D. Faulkner, W. Bell, and R. Adamson, "Characterization of neutron irradiation damage in zirconium alloys–an international "round-robin" experiment," *Journal of nuclear materials*, vol. 79, no. 2, pp. 379–394, 1979.

[190] M. Griffiths, M. Loretto, and R. Smallman, "Anisotropic distribution of dislocation loops in HVEM-irradiated Zr," *Philosophical magazine a*, vol. 49, no. 5, pp. 613–624, 1984.

[191] M. Griffiths, "Microstructure evolution in Zr alloys during irradiation: Dose, dose rate, and impurity dependence," *Journal of astm international*, vol. 5, no. 1, pp. 1–8, 2007.

[192] ——, "A review of microstructure evolution in zirconium alloys during irradiation," *Journal of nuclear materials*, vol. 159, pp. 190–218, 1988.

[193] J. Abriata and J. Bolcich, "The Nb-Zr (Niobium-Zirconium) system," *Journal of phase equilibria*, vol. 3, no. 1, pp. 34–44, 1982.

[194] A. Khachaturyan, S. Shapiro, and S. Semenovskaya, "Adaptive phase formation in martensitic transformation," *Physical review b*, vol. 43, no. 13, p. 10 832, 1991.

[195] B. Paine and R. Averback, "Ion beam mixing: Basic experiments," *Nuclear instruments and methods in physics research section b: Beam interactions with materials and atoms*, vol. 7, pp. 666–675, 1985.

[196] R. Averback, "Fundamental aspects of ion beam mixing," *Nuclear instruments and methods in physics research section b: Beam interactions with materials and atoms*, vol. 15, no. 1-6, pp. 675–687, 1986.

[197] M. Nastasi, N. Michael, J. Mayer, J. K. Hirvonen, and M. James, *Ion-solid interactions: Fundamentals and applications*. Cambridge University Press, 1996.

[198] G. Fernandez, "Thermodynamic analysis of the stable phases in the Zr-Nb system and calculation of the phase diagram," *Zeitschrift für metallkunde*, vol. 82, no. 6, pp. 478–487, 1991.

[199] W. Han, M. Demkowicz, E. Fu, Y. Wang, and A. Misra, "Effect of grain boundary character on sink efficiency," *Acta materialia*, vol. 60, no. 18, pp. 6341–6351, 2012.

[200] A. Misra, M. Demkowicz, X. Zhang, and R. Hoagland, "The radiation damage tolerance of ultra-high strength nanolayered composites," *Jom*, vol. 59, no. 9, pp. 62–65, 2007.

[201] J. Wang, R. Zhang, C. Zhou, I. Beyerlein, and A. Misra, "Characterizing interface dislocations by atomically informed frank-bilby theory," *Journal of materials research*, vol. 28, no. 13, pp. 1646–1657, 2013.

[202] V. Yamakov, E. Saether, D. Phillips, and E. Glaessgen, "Molecular-dynamics simulation-based cohesive zone representation of intergranular fracture processes in aluminum," *Journal of the mechanics and physics of solids*, vol. 54, no. 9, pp. 1899–1928, 2006.

[203] V. Yamakov, E. Saether, and E. Glaessgen, "Multiscale modeling of intergranular fracture in aluminum: Constitutive relation for interface debonding," *Journal of materials science*, vol. 43, no. 23-24, p. 7488, 2008.

[204] A. Griffith, "The phenomena of rupture and flow in solids," *Philosophical transactions of the royal society of london. series a, containing papers of a mathematical or physical character*, vol. 221, pp. 163–198, 1921.

[205] Z. Yang, Y. Zhou, T. Wang, Q. Liu, and Z. Lu, "Crack propagation behaviors at Cu/SiC interface by molecular dynamics simulation," *Computational materials science*, vol. 82, pp. 17–25, 2014.

[206] W. Han, E. Cerreta, N. Mara, I. Beyerlein, J. Carpenter, S. Zheng, C. Trujillo, P. Dickerson, and A. Misra, "Deformation and failure of shocked bulk Cu–Nb nanolaminates," *Acta materialia*, vol. 63, pp. 150–161, 2014.